UNCLASSIFIED

CENTRAL RESEARCH LIBRARY
DOCUMENT COLLECTION

MARTIN MARIETTA ENERGY SYSTEMS LIBRARIES
3 4456 0360730 9

ORNL 1798
Progress
Cy. 5

PHYSICS DIVISION
SEMIANNUAL PROGRESS REPORT
FOR PERIOD ENDING SEPTEMBER 10, 1954

CENTRAL RESEARCH LIBRARY
DOCUMENT COLLECTION
LIBRARY LOAN COPY
DO NOT TRANSFER TO ANOTHER PERSON
If you wish someone else to see this document, send in name with document and the library will arrange a loan.

OAK RIDGE NATIONAL LABORATORY
OPERATED BY
CARBIDE AND CARBON CHEMICALS COMPANY
A DIVISION OF UNION CARBIDE AND CARBON CORPORATION
UCC
POST OFFICE BOX P
OAK RIDGE, TENNESSEE

UNCLASSIFIED

ORNL-1798

Copy No. 5

Contract No. W-7405-eng-26

PHYSICS DIVISION

SEMIANNUAL PROGRESS REPORT

for Period Ending September 10, 1954

A. H. Snell, Director

Edited by

J. L. Fowler and E. O. Wollan

Associate Directors

DATE ISSUED

NOV 26 1954

OAK RIDGE NATIONAL LABORATORY

Operated by

CARBIDE AND CARBON CHEMICALS COMPANY

A Division of Union Carbide and Carbon Corporation

Post Office Box P

Oak Ridge, Tennessee

MARTIN MARIETTA ENERGY SYSTEMS LIBRARIES

3 4456 0360730 9

INTERNAL DISTRIBUTION

1. C. E. Center
2. Biology Library
3. Health Physics Library
4-6. Central Research Library
7. Reactor Experimental Engineering Library
8-12. Laboratory Records Department
13. Laboratory Records, ORNL R.C.
14. C. E. Larson
15. L. B. Emlet (K-25)
16. J. P. Murray (Y-12)
17. A. M. Weinberg
18. E. H. Taylor
19. E. D. Shipley
20. E. J. Murphy
21. F. C. VonderLage
22. A. H. Snell
23. A. Hollaender
24. J. A. Swartout
25. K. Z. Morgan
26. F. L. Culler
27. M. T. Kelley
28. E. M. King
29. E. O. Wollan
30. D. W. Cardwell
31. A. S. Householder
32. L. D. Roberts
33. R. B. Briggs
34. R. N. Lyon
35. W. C. Koehler
36. E. P. Blizard
37. M. E. Rose
38. G. E. Boyd
39. Lewis Nelson
40. R. W. Stoughton
41. C. E. Winters
42. W. H. Jordan
43. E. C. Campbell
44. D. S. Billington
45. M. A. Bredig
46. R. S. Livingston
47. C. P. Keim
48. J. L. Meem
49. C. E. Clifford
50. G. H. Clewett
51. C. D. Susano
52. C. J. Borkowski
53. M. J. Skinner
54. M. K. Wilkinson
55. S. Bernstein
56. P. M. Reyling
57. D. D. Cowen
58. W. M. Good
59. G. C. Williams
60. J. L. Fowler
61. R. W. Johnson
62. J. R. McNally, Jr.
63. J. L. Gabbard
64. C. L. Storrs
65. P. M. Steir
66. R. A. Charpie
67. E. P. Wigner (consultant)
68. H. A. Bethe (consultant)
69. K. Lark-Horovitz (consultant)
70. Eugene Guth (consultant)
71. J. G. Daunt (consultant)
72. W. M. Breazeale (consultant)
73. E. C. Smith
74. C. G. Hull
75. P. R. Bell
76. G. G. Kelley
77. C. C. Harris
78. H. G. MacPherson (consultant)
79. P. H. Stelson
80. J. E. Sherwood
81. U. H. Bents
82-83. ORNL Document Reference Library, Y-12 Branch
84. W. Zobel

EXTERNAL DISTRIBUTION

85. W. G. Pollard, ORINS
86. W. K. H. Panofsky, Stanford University
87. L. C. Biedenharn, Sloans Physics Laboratory
88. R. F. Bacher, California Institute of Technology
89. John Dunning, Columbia University
90. Phillips Petroleum Co., Attn: Librarian
91. R. L. Health, American Cyanamid Co.
92. S. DeBenedetti, Carnegie Institute of Technology
93. Massachusetts Institute of Technology, Department of Electrical Engineering
94. A. von Hippel, Laboratory for Insulation Research, MIT
95. M. Goodrich, Louisiana State University
96. Truman S. Grey, Massachusetts Institute of Technology
97. V. C. Wilson, General Electric Co., Schenectady
98. D. S. Hughes, University of Texas
99. E. A. Rollor, ANP Project Office, Fort Worth
100. S. Frankel, Physics Dept., University of Pennsylvania
101. G. Griffith, Westinghouse Research Laboratory, E. Pittsburgh, Pennsylvania
102. F. Allison, Emory and Henry University, Emory, Virginia
103. J. A. Sauer, Physics Dept., Pennsylvania State University

104-356. Given distribution as shown in TID 4500 under Physics Category

Physics Division progress reports previously issued in this series are as follows:

ORNL-325 Supplement	December, January, and February, 1948-1949
ORNL-366	Period Ending June 15, 1949
ORNL-481	Period Ending September 25, 1949
ORNL-577	Period Ending December 15, 1949
ORNL-694	Period Ending March 15, 1950
ORNL-782	Period Ending June 15, 1950
ORNL-865	Period Ending September 20, 1950
ORNL-940	Period Ending December 20, 1950
ORNL-1005	Period Ending March 20, 1951
ORNL-1092	Period Ending June 20, 1951
ORNL-1164	Period Ending September 20, 1951
ORNL-1278	Period Ending December 20, 1951
ORNL-1289	Period Ending March 20, 1952
ORNL-1365	Period Ending June 20, 1952
ORNL-1415	Period Ending September 20, 1952
ORNL-1496	Period Ending December 20, 1952
ORNL-1620	Period Ending September 10, 1953
ORNL-1705	Period Ending March 10, 1954

CONTENTS

PUBLICATIONS vii

PAPERS PRESENTED AT SCIENTIFIC MEETINGS BY MEMBERS OF THE PHYSICS DIVISION vii

ANNOUNCEMENTS viii

SUMMARY 1

1. HIGH-VOLTAGE PHYSICS 3

Total Neutron Cross Section of Li^6 3
Differential Neutron-Scattering Cross Section for Nitrogen 3
Elastic Scattering of Neutrons on Normal Boron and Be^9 6
A Note on the Polarization of $Li^7(p,n)Be^7$ Neutrons 7
Mass Differences from (p,n) Threshold Measurements 8
Neutron Spectrum and Angular Distribution of $Li^7(d,n)Be^8$ Reaction 8
Coulomb Excitation 11
Gamma Rays from Boron and Carbon-13 Bombarded by Protons 18

2. RADIOACTIVITY AND NUCLEAR ISOMERISM 23

Improved Total-Absorption Spectrometer 23
Decay of Bi^{207} 26
Decay of Sb^{124} 31
Response of Lithium Iodide (Europium) Phosphor 32
A Comparison of Large-Single-Crystal and Multiple-Crystal Gamma-Ray Spectrometers 34
Nuclear Isomers of Short Half Life 35
Search for Isomer Daughter of Nb^{90} 39
Search for O^{20} 40
Separation of Ge^{73m} from As^{73} and of Ir^{191m} from Os^{191} 40
Angular Correlation of Gamma Rays 40

3. NEUTRON DIFFRACTION 41

Neutron-Diffraction Studies of Perovskite-Type Compounds $LaRO_3$ 41
Continuation of Magnetic Study of the Series of Compounds $[xLa, (1-x)Ca]MnO_3$ 42
Neutron-Diffraction Spectrometer with Cryostat and Magnetic Field 45
Magnetic Structure of Nickel-Iron Alloys 46
Magnetic Structure of Mn_2Sb 49
Study of $CuCl_2 \cdot 2H_2O$ 51
On the Structures of Some Compounds of the Perovskite Type 51

4. LOW-TEMPERATURE PHYSICS – NUCLEAR ALIGNMENT 57

Brute-Force Polarization of In^{115} Nuclei 57
Magnetic Transition in Uranium Tri-iodide at Liquid-Helium Temperatures 57
Magnetic Transition in Anhydrous Manganous Chloride at Liquid-Helium Temperatures 60

5. HEAVY-ION PHYSICS 64

Investigation of Electron Capture and Loss for Heavy Ions Passing Through Gases 64

6. NEUTRINO RECOIL 66

Recoil Spectrometry 66

7. THEORETICAL PHYSICS 69
Nuclear Structure from High-Energy Electron Scattering 69
Quantum Electrodynamics 71

PUBLICATIONS

R. A. Erickson and L. D. Roberts, "The Measurement and the Calculation of the Liquid Helium Vapor Pressure–Temperature Scale from 1° to 4.2°K," *Phys. Rev.* **93**, 957–962 (1954).

W. M. Good, W. E. Kunz, and C. D. Moak, "The He^3 + He^3 Reactions," *Phys. Rev.* **94**, 87–91 (1954).

M. E. Rose and R. K. Osborn, "The Pseudoscalar Interaction and the Beta Spectrum of RaE," *Phys. Rev.* **93**, 1315–1325 (1954).

M. E. Rose and R. K. Osborn, "Nuclear Matrix Elements in Beta Decay," *Phys. Rev.* **93**, 1326–1336 (1954).

C. P. Stanford, T. E. Stephenson, L. W. Cochran, and S. Bernstein, "Neutron Polarization," *Phys. Rev.* **94**, 374–381 (1954).

F. Maienschein and T. Love, "Gamma-Ray Spectrum of the Bulk Shielding Reactor," *Nucleonics* **12**, No. 5 (1954).

M. K. Wilkinson, "Techniques and Applications of Neutron Diffraction," *Am. J. Phys.* **22**, 263–276 (1954).

H. W. Newson and R. H. Rohrer, "Shell Effects in Highly Excited Nuclei," *Phys. Rev.* **94**, 654–658 (1954).

A. Simon and T. A. Welton, "Polarization from Isolated Resonances," *Phys. Rev.* **94**, 943–944 (1954).

S. Bernstein, L. D. Roberts, C. P. Stanford, J. W. T. Dabbs, and T. E. Stephenson, "Interaction of Polarized Neutrons with Polarized Mn^{55} Nuclei," *Phys. Rev.* **94**, 1243–1251 (1954).

L. D. Roberts and D. E. LaValle, "The Anomalous Magnetic Behavior of UI_3 from 1–4.2°K," *J. Chem. Phys.* **22**, 1145–1146 (1954).

R. K. Sheline, N. R. Johnson, P. R. Bell, R. C. Davis, and F. K. McGowan, "Study of the Isobaric Triplet Mg^{28}–Al^{28}–Si^{28}," *Phys. Rev.* **94**, 1642–1651 (1954).

N. H. Lazar, "Decay of Sb^{124}," *Phys. Rev.* **95**, 292–293 (1954).

W. C. Koehler and E. O. Wollan, "Search for Antiferromagnetism in the Silicides V_3Si, Cr_3Si, and Mo_3Si," *Phys. Rev.* **95**, 280–281 (1954).

A. H. Snell, "Atoms and Energy" (Review of book by H. S. W. Massey, Elek Books, London), *Sci. Monthly* **78**, No. 5 (1954).

A. H. Snell, "Reactors or Other Nuclear Machines?" *Physics Today* **7**, 7–9 (1954).

L. D. Roberts, S. Bernstein, J. W. T. Dabbs, and C. P. Stanford, "The Capture of Polarized Neutrons by Polarized Sm^{149} Nuclei," *Phys. Rev.* **95**, 105 (1954).

J. W. T. Dabbs and L. D. Roberts, "The Polarization of Mn^{55} Nuclei: Cryogenic Aspects," *Phys. Rev.* **95**, 970 (1954).

L. D. Roberts, S. Bernstein, J. W. T. Dabbs, and C. P. Stanford, "Interaction of Polarized Neutrons with Polarized Sm^{149} Nuclei," *Phys. Rev.* **94**, 1243 (1954).

A. H. Snell, "Nuclear Theory" (Review of book by R. G. Sachs, Addison-Wesley, Cambridge, Mass., 1953), *Science* **120**, 301 (1954).

PAPERS PRESENTED AT SCIENTIFIC MEETINGS BY MEMBERS OF THE PHYSICS DIVISION

American Physical Society Meeting, Detroit–Ann Arbor, March 18–20, 1954

M. K. Wilkinson and C. G. Shull, "Neutron Diffraction Observations on Iron at High Temperatures."

C. G. Shull and M. K. Wilkinson, "Small Angle Neutron Scattering by Iron at High Temperatures."

American Physical Society Meeting, Knoxville, April 1–3, 1954

H. B. Willard, "Elastic Scattering Angular Distributions and Polarization of Fast Neutrons," (invited speech).

T. A. Welton, "On the Theory of Nuclear Reactions with a Radioactive Product."

J. E. Sherwood, T. E. Stephenson, C. P. Stanford, and S. Bernstein, "Stern-Gerlach Experiment on Polarized Neutrons."

A. H. Snell and F. Pleasonton, "Magnetic Spectrometer for Recoil Spectrometry."

R. B. Murray, "The Specific Heat of $MnCl_2$ at the Temperatures of Liquid Helium."

L. D. Roberts and J. W. T. Dabbs, "An Approximate Partition Function for Certain Iron Group Salts at Low Temperatures."

J. W. T. Dabbs and L. D. Roberts, "A Method for Brute Force Polarization of Hydrogen Nuclei."

American Physical Society Meeting, Washington, D. C., April 29–May 1, 1954

C. H. Johnson and J. L. Fowler, "Differential Cross Section for Elastic Scattering of Neutrons from Nitrogen."

C. C. Trail and C. H. Johnson, "A Proton Recoil Telescope for Observing Neutron Spectra."

N. H. Lazar and P. R. Bell, "Gamma Radiation from K^{42}."

C. D. Moak, W. M. Good, and W. E. Kunz, "The Be^9 + He^3 Reactions."

W. E. Kunz, C. D. Moak, and W. M. Good, "The $Li^7(He^3,p)He^9$ Reaction."

W. C. Koehler and E. O. Wollan, "Neutron-Magnetic Diffraction Studies of Lanthanum, Calcium Manganites."

J. H. Neiler, F. Muckenthaler, and J. Schenck, "Fast Neutron Scintillation Spectra of $Li^6(n,\alpha)H^3$ in LiI(Eu)."

A. Simon, "High Speed Computation of Angular Momentum Functions."

G. T. Trammell, "Electron Scattering from Nuclei."

T. A. Welton, "On the Formulation of Quantum Electrodynamics in Minkowski Space."

Glasgow 1954 Physics Conference, Glasgow, Scotland, July 13, 1954

S. Bernstein, L. D. Roberts, C. P. Stanford, J. W. T. Dabbs, and T. E. Stephenson, "Observation of the Interaction of Polarized Neutrons with Polarized Mn^{55} and Sm^{149} Nuclei."

Solvay Conference, Brussels, Belgium, September 13–18, 1954

C. G. Shull, "Neutron Diffraction Studies of Transition Elements and Their Alloys."

ANNOUNCEMENTS

The following persons have been added to the staff of the Physics Division during this period: H. O. Cohn, J. E. Wills, Jr. (ORINS fellow), and A. I. Galonsky (High Voltage); A. E. Glassgold (Theoretical); and F. G. Prohammer, transferred from ANP Division, and C. D. Zerby, transferred from Reactor Experimental Engineering Division (Shielding).

R. G. Cochran (Shielding) is on leave and is attending Pennsylvania State College, completing work toward the Ph.D. degree.

Terminations: C. P. Stanford and T. E. Stephenson (Nuclear Alignment Group); C. C. Trail (ORINS fellow) and C. W. Snyder (High Voltage); G. S. Pawlicki (Neutron Velocity Selector); and J. E. Faulkner (Shielding).

Summer personnel included the following Research Participants and university students: R. K. Sheline (Associate Professor, Florida State University) and M. Goodrich (Professor, Louisiana State University), Instrumentation Group; H. Brysk (visiting Assistant Professor, Vanderbilt University), Theoretical Physics; T. J. Turner (Assistant Professor, University of Virginia), Neutron Diffraction; R. A. Howard (Associate Professor, University of Oklahoma),

Heavy Ion Physics; H. P. Hotz (Assistant Professor, Alabama Polytechnic Institute), High Voltage; and A. W. Hanson (Associate Professor, The Citadel), Neutron Velocity Selector; J. M. Jauch (summer visitor, State University of Iowa) and L. C. Biedenharn (summer visitor, Yale University) Theoretical Physics, W. M. Bugg (student, University of Tennessee), Heavy Ion Physics; J. P. Evans (student, Marquette University), Recoil Spectrometry; D. S. Faulk (student, Cornell University), Theoretical Physics; R. W. Kedzie (student, Marquette University), Neutron Diffraction; W. A. Moser (student, Vanderbilt University), Instrumentation; H. Postma (student, Duke University) and E. A. Soltysik (student, Indiana University), Low Temperature Group; and W. A. Steyert, Jr. (student, Massachusetts Institute of Technology), Shielding.

PHYSICS DIVISION
SEMIANNUAL PROGRESS REPORT

SUMMARY

HIGH-VOLTAGE PHYSICS

The total neutron cross section of Li^6 has been remeasured, and the results have been found to agree substantially with the older measurements, which had yielded for the 0.255-Mev resonance the characterization $J = 5/2$, odd parity.

The differential cross section for the elastic scattering of neutrons on nitrogen has been obtained in the energy range from 0.5 to 2.5 Mev. In addition to the nonresonant phase shifts, the following angular momentum and parity assignments have been established for the states in N^{15} of corresponding neutron energy: 1.12 Mev, $J = 3/2$ minus; 1.401 Mev, $J = 3/2$ minus; 1.595 Mev, $J = 5/2$ minus; 1.779 Mev, $J = 5/2$ plus.

The elastic scattering of neutrons on normal boron and on Be^9 has been studied. It is shown that the 0.43- and 1.28-Mev neutron resonant levels in normal boron have, respectively, the assignments $J = 2$ plus and $J = 3$ minus. In Be^9 the levels at neutron resonant energies of 0.62 and 0.81 Mev have, respectively, the assignments $J = 3$ and $J = 2$, with the parities uncertain.

In continued work with polarized neutrons from $Li^7(p,n)Be^7$, some finer details of the product polarization with O^{16} used as polarization analyzer have been observed which are consistent with 50% as the degree of polarization from the $Li^7(p,n)Be^7$ reaction at 42 deg to the beam. Measurements in which He^4 serves as analyzer give this polarization as 54 ± 18%.

The (p,n) thresholds for N^{15}, Mg^{25}, Mg^{26}, Cu^{63}, and Cu^{65} have been found to be, respectively, 3.783 ± 0.008, 5.294 ± 0.015, 5.074 ± 0.010, 4.226 ± 0.008, and 2.172 ± 0.005 Mev. The first three values agree well with calculated values based on coulomb energy.

A neutron spectrometer has been used to study the $Li^7(d,n)Be^8$ reaction. The neutron spectrum shows only the ground and 3-Mev states in Be^8, contradicting the old photoplate studies. The angular distributions of both neutron groups are predominantly forward, probably indicating at least some stripping.

"Coulomb-excited" gamma radiation produced by protons and alpha particles has been the object of further study, especially as regards cross section and angular distribution of the radiation. The data obtained have been interpreted in terms of the following nuclear parameters: level position, angular momentum, parity and gamma-ray transition matrix element. In three cases where the matrix elements have been alternatively determined from direct half-life measurements, the agreement is good.

Gamma rays have been studied from proton capture and proton inelastic scattering on normal boron. In addition, the angular distribution of the $C^{13}(p,\gamma)N^{14}$ ground-state gamma ray has been studied at the 3.11-Mev proton resonance. The angular distribution is consistent with the 10.43-Mev level in N^{14}, being characterized as $J = 2$ minus.

RADIOACTIVITY AND NUCLEAR ISOMERISM

An improved total-absorption gamma-ray scintillation counter has been constructed in which a large sodium iodide crystal is surrounded by a large solution counter tank operating in anticoincidence with the crystal. A reduction of about a factor of 10 in the Compton distribution or pair peaks is obtained.

The decay scheme of Bi^{207} has been investigated to determine the presence or absence of two reported gamma-ray lines, both of which are now found to be absent.

Two new gamma rays have been found in Sb^{124}, and the decay scheme has been worked out.

A critical study has been made of the fast-neutron response characteristics of lithium iodide crystals activated with europium.

Various single-crystal spectrometer arrangements have been compared in energy resolution with multiple-crystal arrangements.

Four nuclear isomers of short half life not previously reported have been found in germanium, cadmium, and iridium. New measurements are given for isomers produced by neutron irradiation

of zirconium, germanium, ytterbium, and lead.

It has been shown that the isomer produced by fast neutrons on Zr^{90} is not a daughter of Nb^{90}. An attempt to detect O^{20} by the $O^{18}(t,p)$ reaction was not successful.

The angular correlations of gamma rays in cascade have been measured for certain excited states in Te^{124}, Pb^{207}, and Cr^{52}.

NEUTRON DIFFRACTION

The perovskite compounds $LaRO_3$ have been studied for R = V, Cr, Mn, Fe, and Co, the middle three being found to be antiferromagnetic, with chromium and iron of one structure type and manganese of another. X-ray studies of these compounds are also included. Further discussion is given of the (La, Ca) manganite series for which a newly installed spectrometer with cryostat and magnetic field has been used to determine the nature of the ferro- and antiferromagnetic reflections. A study of $CuCl_2 \cdot 2H_2O$ has been started.

The atomic magnetic moments have been determined for the individual atoms in a series of Ni-Fe alloys. From these investigations it appears that ordering of the lattice has little or no effect on the component magnetic moments and that these values are dependent on the over-all lattice composition.

The magnetic structure of Mn_2Sb has been determined from an investigation of single-crystal reflectivities with magnetized and unmagnetized samples.

LOW-TEMPERATURE PHYSICS – NUCLEAR ALIGNMENT

Preliminary nuclear polarization experiments appear to have demonstrated brute-force nuclear alignment in In^{116}.

A series of measurements of the susceptibility and specific heat of UI_3 in the liquid-helium region suggest that the material becomes antiferromagnetic at 2.61°K and that a domain structure composed of antiferromagnetic regions separated by ferromagnetic domain walls exists.

Further work on anhydrous $MnCl_2$ has established the validity of the unusual, double specific-heat peak previously reported, and it is tentatively suggested that this material undergoes two antiferromagnetic transitions.

HEAVY-ION PHYSICS

Electron-loss cross sections for fast hydrogen atoms passing through various gases are reported. The energy range studied was 20 to 200 kev, and the stopping gases were hydrogen, helium, nitrogen, oxygen, neon, and argon. Curves are presented of the electron-capture cross sections for protons calculable from these data and the previously reported ratio of electron loss-to-capture cross sections.

NEUTRINO RECOIL

Recoils from neutrino emission in A^{37} have been analyzed both magnetically and electrically, and peaks corresponding to Cl^{37} ions of charges 2+, 3+, and 4+ have been observed. At present the values of the recoil energy as determined from the two methods bracket within a volt the value of 9.6 ev predicted from the disintegration energy that is available. Further work is being done to improve the precision of this measurement as well as to obtain the relative intensities of the several peaks.

THEORETICAL PHYSICS

The problem of calculating the mass correction for the electron has been rephrased in a form amenable to exact calculation. Calculation of a simple case makes plausible the hypothesis that the diverging mass correction represents nothing but a failure of the perturbation theory.

The ORACLE has been used in obtaining electron-scattering phase shifts for various nuclear models, and the results are compared with available experimental data.

1. HIGH-VOLTAGE PHYSICS

TOTAL NEUTRON CROSS SECTION OF Li^6

C. H. Johnson H. B. Willard
J. K. Bair

The total neutron cross section of Li^6 has been remeasured with samples of high purity. In 1952 the cross section was measured[1] for neutron energies from 0.035 to 4.2 Mev; the results were not published, however, because the purity of the lithium samples was questionable. For the present measurements the Stable Isotopes Division provided two scattering samples which had a chemical purity of 99.97% and were enriched to 93.8% in Li^6. The total cross section was determined in the neighborhood of the resonance by means of a standard transmission experiment. Neutrons were produced by the $Li^7(p,n)Be^7$ reaction and detected with a propane-filled recoil counter. In Fig. 1.1 the upper curve is the total cross section in the region of the resonance. The solid circles and triangles are the results of the present measurements with two different samples. Four other symbols are used to refer to our previous measurements. The two sets are in good agreement and indicate a resonance at 0.255 ± 0.010 Mev with a width of 100 kev. The X's refer to the (n,α) cross section of Blair and Holland.[2] The two solid curves are calculated from the Breit-Wigner formula with the assumption that the resonance results from p-wave neutrons forming a state of $J = 5/2$.

[1] C. H. Johnson, H. B. Willard, and J. K. Bair, *Phys. Quar. Prog. Rep. June 20, 1952*, ORNL-1374, p 10.

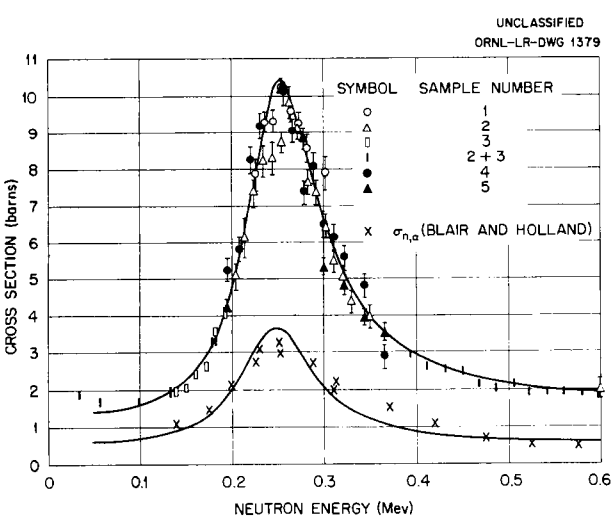

Fig. 1.1. Neutron Cross Section of Li^6 Near the 255-kev Resonance.

DIFFERENTIAL NEUTRON-SCATTERING CROSS SECTION FOR NITROGEN

C. H. Johnson J. L. Fowler

The differential cross section for elastic scattering of neutrons from nitrogen has been measured by two independent techniques. In one series of experiments a proton-recoil neutron detector has been used to measure the scattered neutrons as a function of angle.[3] In another set of experiments the angular distribution of neutrons was deduced from the energy distribution of recoil nitrogen nuclei.[4] The neutron-detection experiment, which had very low counting rates and therefore was done only with relatively thick targets (~40 kev), gave reliable results over most of the angular region. This experiment was used to measure the differential cross section between resonances. The nitrogen-recoil experiment could be done with thin targets and was used to investigate the angular distributions at the resonances.

Comparison of the two types of measurements normalized in the region $\cos\phi = 0$ to $\cos\phi = -0.9$ shows that the nitrogen-recoil data are unreliable for angles with $\cos\phi > 0.5$ and that at low energies (<1.8) these data deviate from the neutron data in the region $\cos\phi = 0.1$ to $\cos\phi > 0.5$ by as much as 28%. From such comparisons, correction curves were plotted for the recoil data from $\cos\phi = 0.1$ to $\cos\phi = 0.5$. The corrected recoil data are plotted as solid circles in Figs. 1.2, 1.3, and 1.4. The straggling at the upper edge ($\cos\phi = -1.0$) of the recoil data is due to the pulse-height energy resolution of the recoil counter. The

[2] J. M. Blair and R. E. Holland, *Neutron Cross Sections*, AECU-2040 (May 15, 1952).

[3] C. H. Johnson and J. L. Fowler, *Phys. Rev.* 95, 637 (1954).

[4] J. L. Fowler, C. H. Johnson, and J. R. Risser, *Phys. Rev.* 91, 441 (1953).

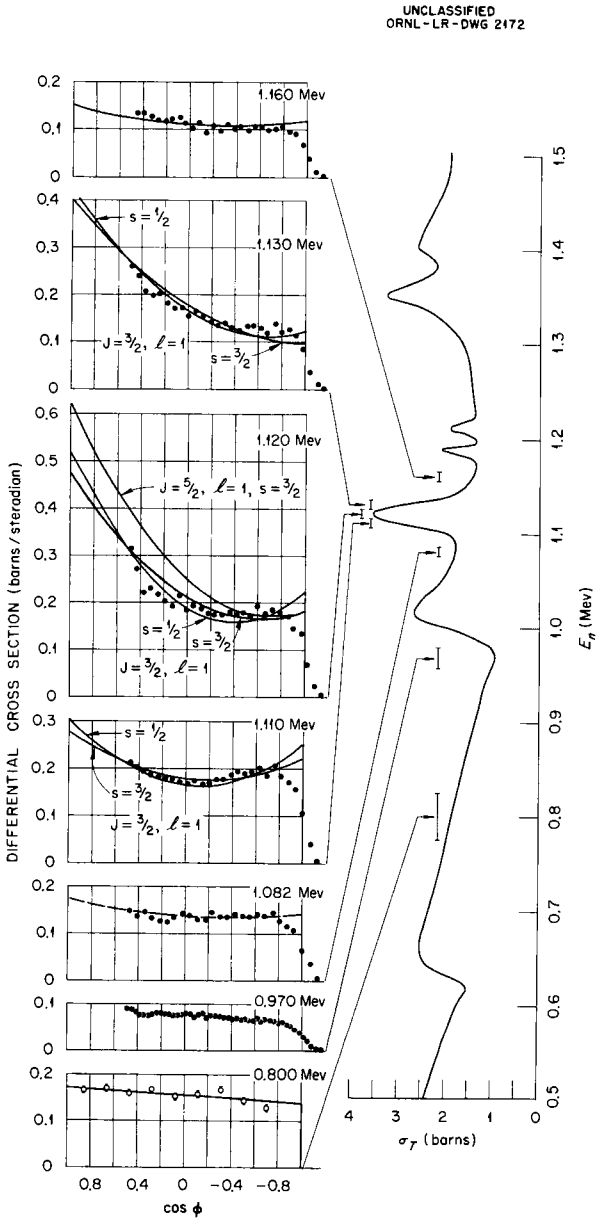

Fig. 1.2. Differential Elastic Cross Sections for N^{14} for Neutron Energies from 0.80 to 1.16 Mev.

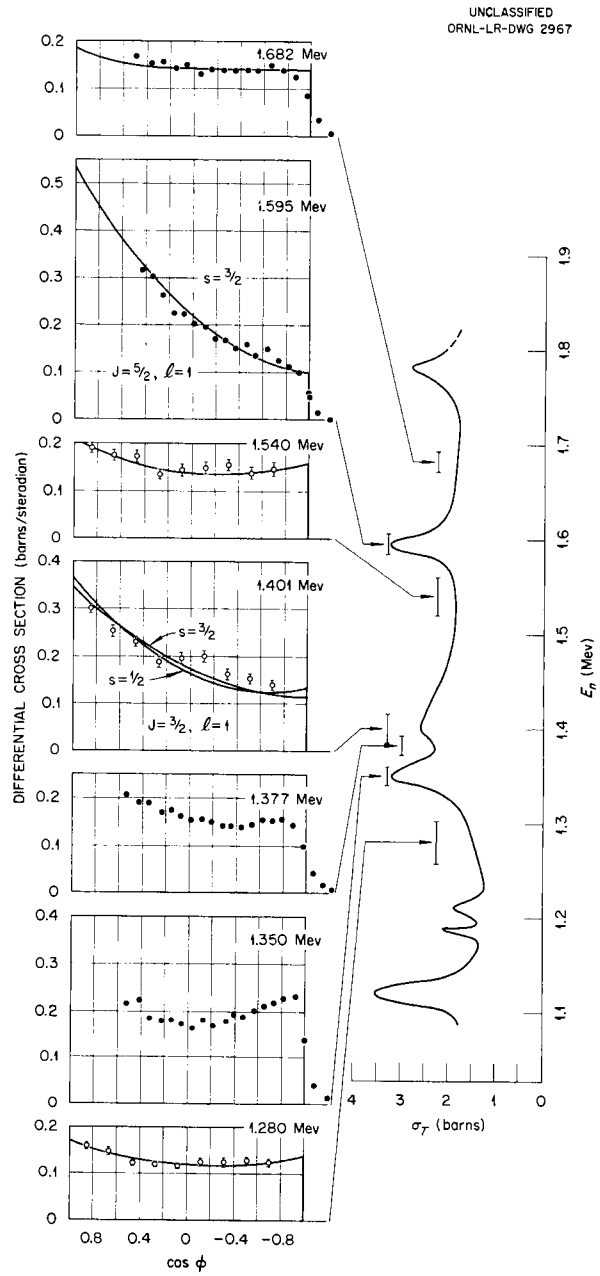

Fig. 1.3. Differential Elastic Cross Sections for N^{14} for Neutron Energies from 1.28 to 1.682 Mev.

arrows on the right-hand side[5,6,7] in Figs. 1.2, 1.3, and 1.4 indicate on the total-cross-section curve the energy at which the measurements were made. The bars at the end of the arrows give the full energy at one-half maximum of the neutron source.

[5] C. H. Johnson, B. Petree, and R. K. Adair, *Phys. Rev.* 84, 775 (1951).

[6] J. J. Hinchey, P. H. Stelson, and W. M. Preston, *Phys. Rev.* 86, 483 (1952).

[7] C. H. Johnson, H. B. Willard, J. K. Bair, and J. D. Kington, *Phys. Quar. Prog. Rep. June 20, 1952*, ORNL-1365, p 1.

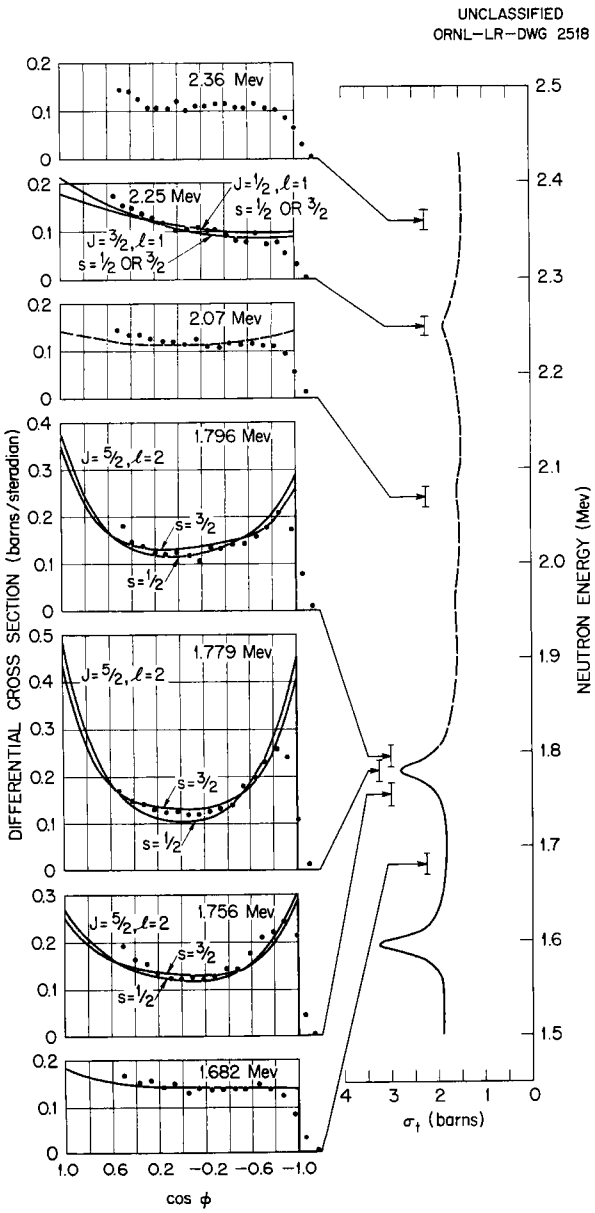

Fig. 1.4. Differential Elastic Cross Sections for N^{14} for Neutron Energies from 1.682 to 2.34 Mev.

The nonresonance neutron data, plotted as open circles in Figs. 1.2 and 1.3, were used to calculate the potential scattering phase shifts shown in Fig. 1.5. Below 0.8 Mev the differential cross section is practically isotropic, so that the phase shift is obtained from the total neutron cross section.[5,6] By use of the method of Blatt and Biedenharn[8] one can calculate the theoretical

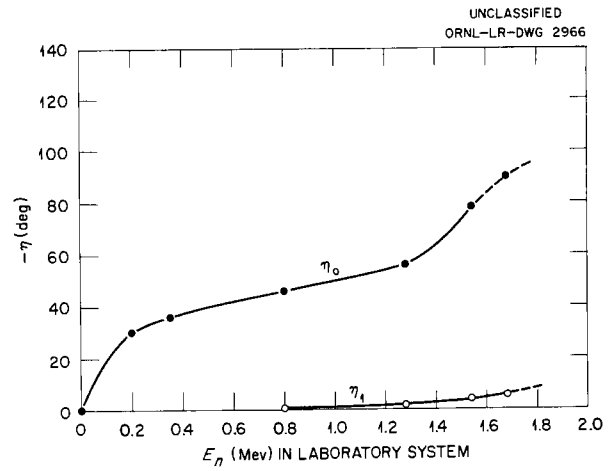

Fig. 1.5. Potential Scattering *s*- and *p*-Wave Phase Shifts for N^{14} as a Function of Neutron Energy.

differential cross section to be expected for various types of resonances interfering with potential scattering given by Fig. 1.5. The angular momentum (J values) were deduced by Preston and Stelson[6] from the height and width of the resonances in the total cross section and from the measurements of the (n,p) and (n,α) cross sections in nitrogen.[9]

The solid curves shown in Figs. 1.2, 1.3, and 1.4 are theoretical curves of the differential cross section averaged over the energy spread of the source neutron. These curves uniquely determine the parity of the levels (l = 1 corresponds to odd parity, l = 2 to even) and in the case of the 1.12-Mev resonance show that J = 3/2 rather than 5/2, which is given as a possibility in the literature.[6] Since insufficient data were available for analysis of the 2.25-Mev resonance, no curve has been drawn. The increased forward scattering for this resonance, however, indicates that it is an odd-parity level. Since the 1.40-Mev level interferes strongly with the 1.35-Mev level, the analysis of Blatt and Biedenharn does not apply to the 1.35-Mev level.

[8] J. M. Blatt and L. C. Biedenharn, *Revs. Mod. Phys.* 24, 256 (1952).

[9] C. H. Johnson and H. H. Barschall, *Phys. Rev.* 80, 818 (1950).

ELASTIC SCATTERING OF NEUTRONS ON NORMAL BORON AND Be^9

H. B. Willard J. D. Kington
J. K. Bair H. O. Cohn

Resonances have been observed previously[10,11] in the total cross section of Be^9 at 0.62 and 0.81 Mev, with maxima of 7.2 and 4.8 barns and level widths of $\Gamma = 30$ and $\Gamma \leq 11$ kev, respectively. The total cross section was redetermined in this energy region with the $Li^7(p,n)Be^7$ reaction as a neutron source and with the use of good resolution (4 kev) and good geometry. A propane recoil counter, 1 in. in diameter, was located a mean distance of 18 in. from the target, and the transmission of a ¼-in.-thick, 1-in.-dia beryllium sample located at the mid-point was measured. The 0.62-Mev resonance had a peak cross section of 7.75 ± 0.20 barns and a level width of 25 kev. After subtraction of the 3.40 barns of potential scattering, the remaining contribution of 4.35 barns of resonance scattering is in good agreement with the theoretical value of 4.52 barns predicted by $J = 3$ for the level in the compound nucleus. At 0.81 Mev the maximum cross section was 5.25 ± 0.20 barns and the level width was 8 kev, which is consistent with $J = 2$. No other resonances appear below 2-Mev neutron energy.

Differential cross sections for elastic neutron scattering from Be^9 have been remeasured at 0.62 Mev by using techniques previously described[12] but with better (8-kev) energy resolution. From the new data the angular distribution is given by

$$\sigma(\phi) = 0.60P_0(\cos\phi) + 0.17P_2(\cos\phi)$$

in the center-of-mass system. This is in agreement with the earlier work when proper allowance is made for the resolution. In order to detect the presence of possible interference terms, the ratio of the differential cross section at $\cos\phi_{cm} = 0.58$ to that at $\cos\phi_{cm} = -0.58$ was measured as a function of neutron energy, and the results are shown in Fig. 1.6. Since the potential scattering is all s-wave in this region, it was first assumed that the resonance was described as $J = 3$, $l = 2$; and the best fit was obtained by assuming that the level is all due to channel spin 2. This does not

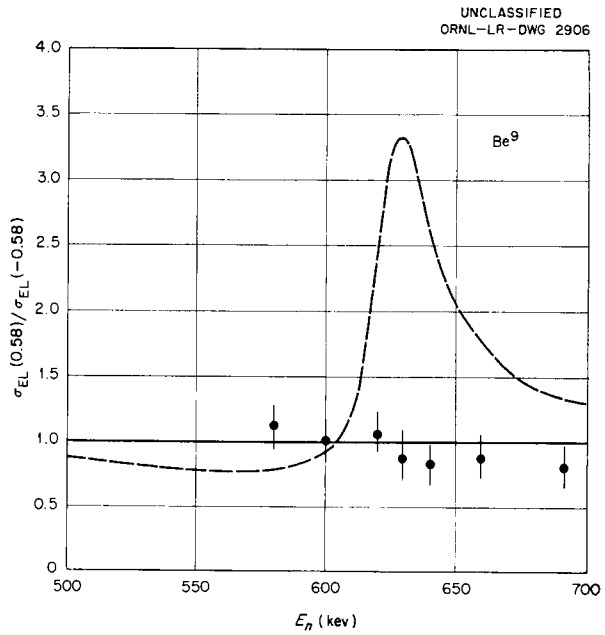

Fig. 1.6. Ratio of Cross Sections for cos ϕ = +0.58 to −0.58 for Be^9, as a Function of Neutron Energy.

agree too well with the data. Alternatively, it is assumed that $J = 3$, $l = 1$, $s = 2$. In this case, the theory of Blatt and Biedenharn[13] predicts a strong interference term, which would manifest itself as the dashed curve in Fig. 1.6. However, if the potential scattering is spin-dependent and all channel spin 1, the interference term becomes zero, and the angular distribution at resonance agrees well with the data. This assignment is somewhat questionable because the scattering is spin-independent at thermal energies.[14]

The total cross section of normal boron below 1.5 Mev shows resonances at 0.43 and 1.28 Mev and widths of 40 and 150 kev, respectively.[10,11] As a check on the assignment of $J = 2$, $l = 1$ to the 0.43-Mev level, and $J = 3$, $l = 2$ to the 1.28-Mev level indicated by the angular distributions,[12] the presence of interference terms was investigated as described above. Figure 1.7 shows a strong $P_1(\cos\phi)$ term in good agreement with the solid theoretical curve $J = 2$, $l = 1$ for the 0.43-Mev resonance. Figure 1.8 indicates symmetry about

[10] C. K. Bockelman, *Phys. Rev.* 80, 1011 (1951).

[11] C. K. Bockelman, D. W. Miller, R. K. Adair, and H. H. Barschall, *Phys. Rev.* 84, 69 (1951).

[12] H. B. Willard, J. K. Bair, and J. D. Kington, *Phys. Semiann. Prog. Rep. Sept. 10, 1953*, ORNL-1620, p 5.

[13] J. M. Blatt and L. C. Biedenharn, *Revs. Mod. Phys.* 24, 258 (1952).

[14] H. Palevsky and R. R. Smith, *Phys. Rev.* 86, 604 (1952).

90 deg in the center-of-mass system in agreement with $J = 3$, $l = 2$ for the 1.28-Mev resonance. The variation for $J = 3$, $l = 1$ is shown as a dashed curve.

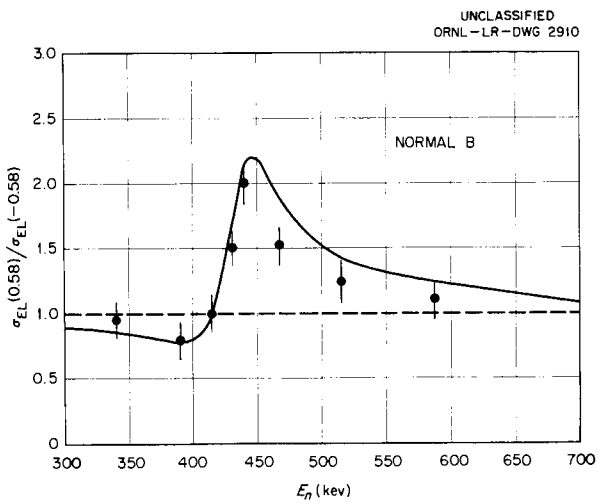

Fig. 1.7. Ratio of Cross Sections for cos ϕ = +0.58 to −0.58 for B^{11}, as a Function of Neutron Energy.

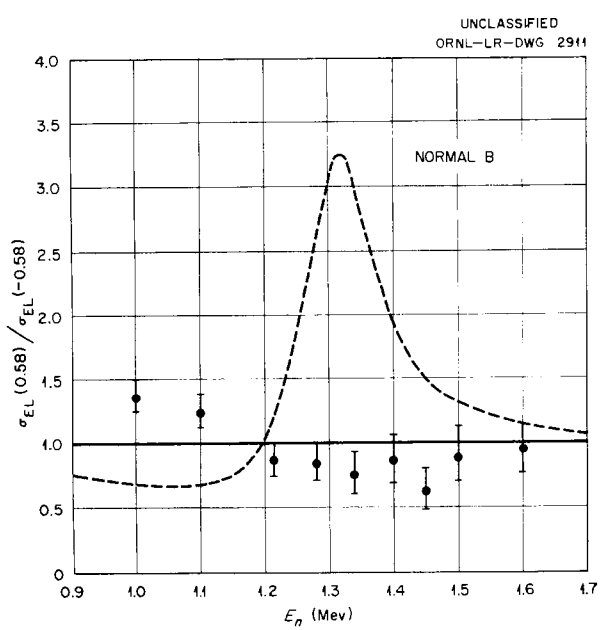

Fig. 1.8. Ratio of Cross Sections for cos ϕ = +0.58 to −0.58 for B^{11}, as a Function of Neutron Energy.

A NOTE ON THE POLARIZATION OF $Li^7(p,n)Be^7$ NEUTRONS

H. B. Willard J. D. Kington
J. K. Bair H. O. Cohn

Neutrons emitted from the $Li^7(p,n)Be^7$ reaction at 42 deg in the laboratory system are polarized nearly 50% from 300 to 500 kev.[15] Previous measurements were repeated in which O^{16} served as an analyzer of these neutrons. The product polarization for 50% polarized neutrons, as shown in Fig. 1.9, follows very closely the theoretical curve for a $P_{3/2}$ level in O^{17} interfering with $S_{1/2}$ potential scattering. Especially to be noted is the manner in which the product polarization reverses sign across the resonance (Fig. 1.9).

[15] H. B. Willard, J. K. Bair, and J. D. Kington, *Phys. Semiann. Prog. Rep. March 10, 1954*, ORNL-1705 p 3; also *Phys. Rev.* (in press).

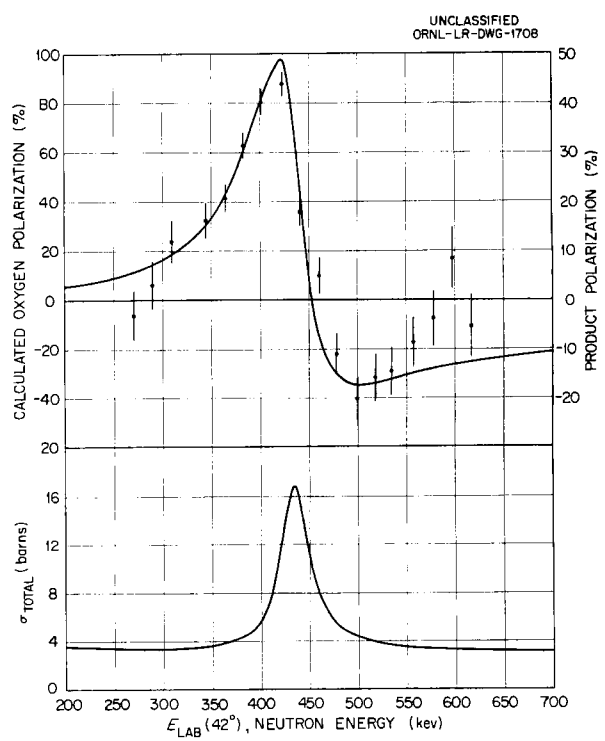

Fig. 1.9. Total Cross Section of O^{16} (lower curve); Theoretical Polarization for Neutrons Scattered Through 90 deg by O^{16} (upper curve, with the use of the left ordinate); Measured Values of the Product Polarization P_1(42 deg)P_2(90 deg) for the $Li^7(p,n)Be^7$ Neutrons Scattered by O^{16} (plotted with the use of the right ordinate).

As a check on the above results, He^4 was employed as the analyzer. The recoiling helium nuclei were detected with a cloud chamber, and the resultant asymmetry, which serves to measure the product polarization, leads independently to a value of 0.54 ± 0.18 for the polarization of 400-kev neutrons. The sign of the polarization is negative.

MASS DIFFERENCES FROM (p,n) THRESHOLD MEASUREMENTS

J. D. Kington J. K. Bair
H. B. Willard

Neutron thresholds for the proton bombardment of N^{15}, Mg^{25}, Mg^{26}, Cu^{63}, and Cu^{65} have been measured to be 3.783 ± 0.008, 5.294 ± 0.015, 5.074 ± 0.010, 4.226 ± 0.008, and 2.172 ± 0.005 Mev, respectively. The absolute energy of the proton beam is believed to be accurate[16] to better than ±0.2% relative to the $Li^7(p,n)Be^7$ threshold value of 1.882 Mev. A Bonner and Butler[17] type of counter was used at 0 deg with respect to the target to measure the relative neutron yield. Nitrogen-15, enriched to 64.5 at. %, was supplied by Eastman Kodak Company. Separated isotopes of Cu^{63}, enriched to 99.11 at. %, and Mg^{25}, enriched to 92.33 at. %, were supplied by the Stable Isotopes Division. Table 1.1 summarizes the thresholds, Q values, coulomb energies calculated using the method of Peaslee,[18] mass differences, and energy available for beta decay of the residual nucleus.

[16] R. G. Herb, S. C. Snowdon, and O. Sala, *Phys. Rev.* 75, 246 (1949).

[17] T. W. Bonner and J. W. Butler, *Phys. Rev.* 83, 1091 (1951).

NEUTRON SPECTRUM AND ANGULAR DISTRIBUTION OF $Li^7(d,n)Be^8$ REACTION

C. C. Trail C. H. Johnson

A proton-recoil telescope has been developed which is an absolute neutron counter and neutron spectrometer. It has been used to study the $Li^7(d,n)Be^8$ reaction. Figure 1.10 is a cross-sectional diagram of the counter. Briefly, it contains a polyethylene radiator, two proportional counters, and an NaI scintillation counter. Neutrons impinge upon the polyethylene (CH_2) and knock out protons. Protons recoiling in the forward direction give rise to pulses in the proportional counters and terminate in the sodium iodide crystal. Triple coincidences arising from a proton passing through the two counters and into the crystal gate a 20-channel pulse sorter, which analyzes the proton spectrum in the crystal. The use of a multichannel analyzer partially compensates for the low neutron counting efficiency, which is about 10^{-5}. Radiators of five thicknesses are mounted on a wheel within the counter; for each neutron-energy region a radiator may be chosen with maximum thickness consistent with the required energy resolution.

The proportional counters are somewhat unconventional. The center wires of the counters are parallel to the direction of the recoil protons. Surrounding the center wire is a field tube held at

[18] D. C. Peaslee, *Phys. Rev.* 95, 717 (1954).

TABLE 1.1. MEASURED THRESHOLDS, CALCULATED Q VALUES, COULOMB ENERGIES, MASS DIFFERENCES, AND ENERGY AVAILABLE FOR BETA DECAY

Reaction	E_{th} (Mev)	Q (Mev)	E_c (Mev)	Mass Difference		Energy, Beta Decay (Mev)
				Mev	Amu	
$N^{15}(p,n)O^{15}$	3.783 ± 0.008	−3.547	3.44	2.77	0.00297	1.74
$Mg^{25}(p,n)Al^{25}$	5.294 ± 0.015	−5.090	5.05	4.31	0.00463	3.29
$Mg^{26}(p,n)Al^{26}$	5.074 ± 0.010	−4.886	5.06	4.10	0.00441	3.08
$Cu^{63}(p,n)Zn^{63}$	4.226 ± 0.008	−4.160		3.38	0.00363	2.36
$Cu^{65}(p,n)Zn^{65}$	2.172 ± 0.004	−2.139		1.36	0.00146	3.34

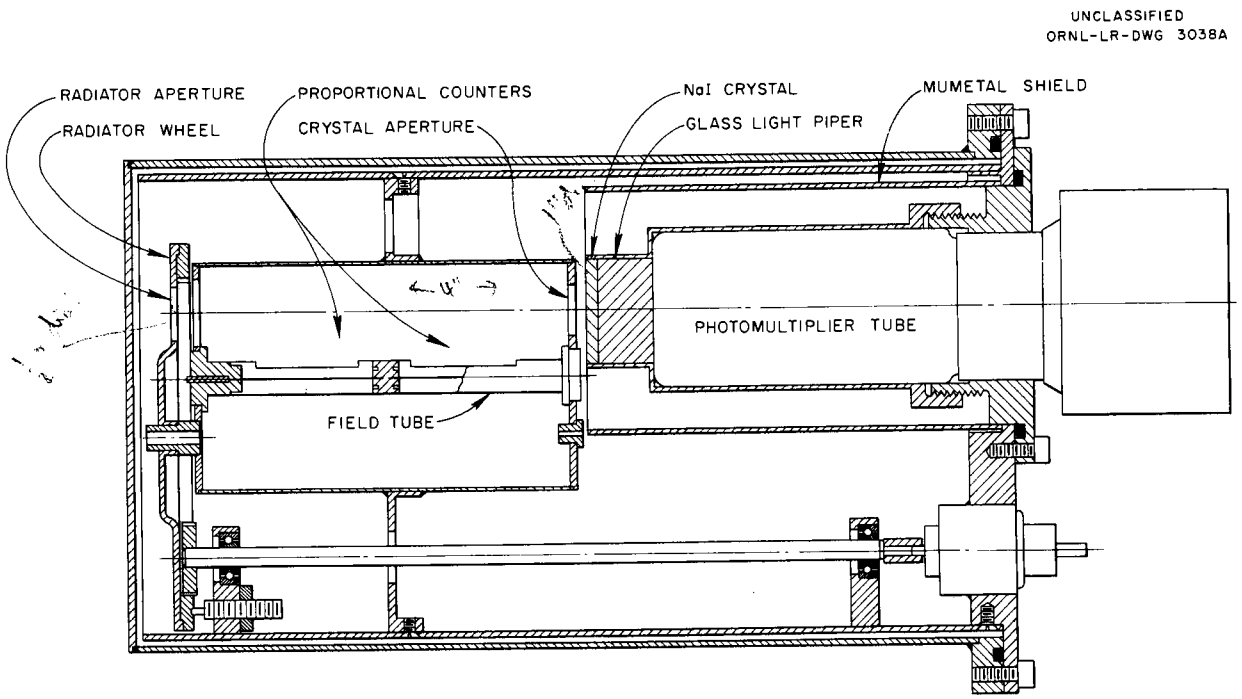

Fig. 1.10. Cross-Sectional Diagram of the Proton-Recoil Telescope.

the proper intermediate potential. The field tube is cut away so that the center wire can collect ionization primarily from that region through which the recoil protons pass; this feature reduces the relative counting rate from the argon recoils in the counter filling. The design also allows the crystal to be relatively close to the radiator and requires no intermediate apertures other than those at the radiator and at the crystal. The last consideration is of importance in an absolute counter because the multiple scattering of protons in the counter gas filling is not negligible.

Figure 1.11 is the spectrum produced in this counter when it is irradiated with 13.5-Mev neutrons. Neutrons were produced in the $T(d,n)He^4$ reaction by bombarding a thick Zr-T target with deuterons from the 2.5-Mev Van de Graaff. The counter was placed with its axis 118 deg to the deuteron beam and with the radiator 6 cm from the source. The resolution is about 5% and is determined primarily by the angular resolution of the counting geometry, the radiator thickness, and the window width of the analyzer.

The above spectrum served to check the counter before proceeding to a study of the $Li^7(d,n)Be^8$ reaction. Several low-lying states in Be^8 have

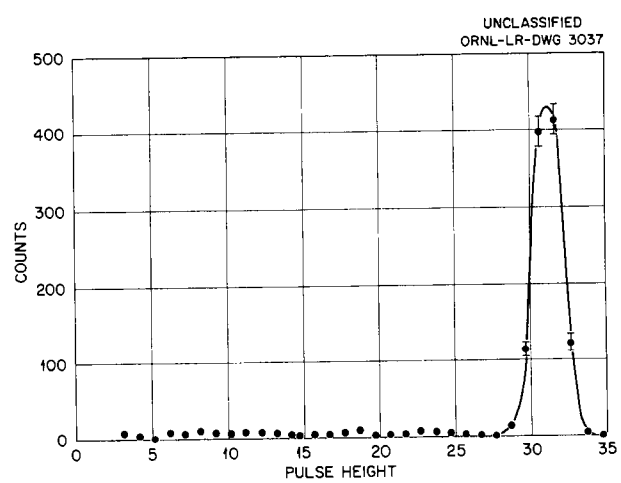

Fig. 1.11. Pulse-Height Distribution Produced in the Spectrometer by Neutrons from the $T(d,n)He^4$ Reaction.

been reported[19] in addition to a well-established broad level at 3 Mev. In particular, Titterton[20]

[19] F. Ajzenberg and T. Lauritsen, *Revs. Mod. Phys.* 24, 321 (1952).

[20] E. W. Titterton, *Phys. Rev.* 94, 206 (1954): this paper contains additional references to previous work.

has discussed the evidence for levels in Be^8 at 4, 5.3, and 7.5 Mev. Existence of the 4-, 5.3-, and 7.5-Mev levels is suggested[21–27] from $B^{11}(\gamma,t)Be^8$, $B^{10}(\gamma,d)Be^8$, $Li^7(d,n)Be^8$, and $Li^7(p,\gamma\alpha)He^4$. Additional evidence for the 7.5-Mev level is given by the alpha-alpha scattering experiment of Steigert and Sampson.[28]

In a recent article Kunz, Moak, and Good[29] reported the proton spectrum from $Li^6(He^3,p)Be^8$. The spectrum indicates only the 3.0-Mev excited state in Be^8 up to an excitation of 10 Mev. Malm and Inglis[30] observed the alpha-particle spectrum from $B^{11}(p,\alpha)Be^8$ and found only the 3-Mev excited state up to an excitation of 7 Mev. The $B^{10}(d,\alpha)Be^8$ reaction[31] was found to leave Be^8 in only the ground and 3.0-Mev state. The neutron spectrum from $Li^7(d,n)Be^8$ has been obtained previously with poor statistics with photographic plates.[23–26] The primary purpose of the present investigation was to measure this neutron spectrum with good statistics.

Separated Li^7 was evaporated in place on the 2.5-Mev Van de Graaff to make a target with 240-kev stopping power for 2-Mev deuterons. The target was bombarded with 5 μa of deuterons with an average energy over the target of 2 Mev. A propane recoil counter with sufficient length and pressure to stop high-energy neutrons from the reaction was used as a monitor. It was necessary to insert a 1-cm-thick disk of iron between the source and the counter to reduce the counting rate from beta particles arising from the competing $Li^7(d,p)Li^8$ reaction.

At two angles, 0 and 120 deg, the amplifier gain for the NaI crystal was adjusted to require five multichannel settings to cover the spectrum, a total of 100 channels. Each setting of the pulse sorter required a different radiator and an adjustment of the coincidence-circuit time constants. Figures 1.12 and 1.13 show the spectra obtained at these two angles. The pulse height is presented in terms of neutron energy, which was chosen from the known energy of the ground-state group. A scale is also given for the excitation energy in Be^8. A background observed in the

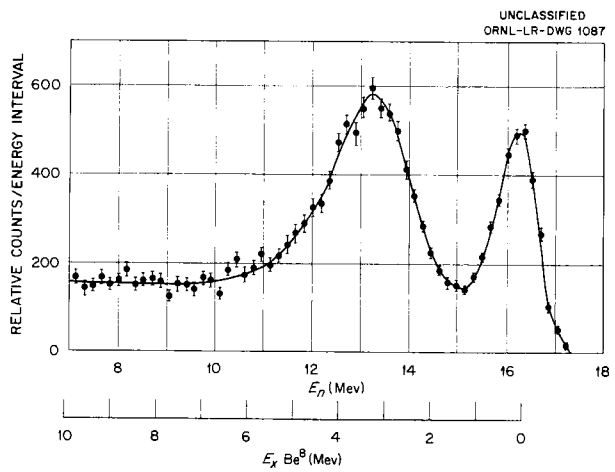

Fig. 1.12. Neutron Spectrum at 0 deg from the $Li^7(d,n)Be^8$ Reaction.

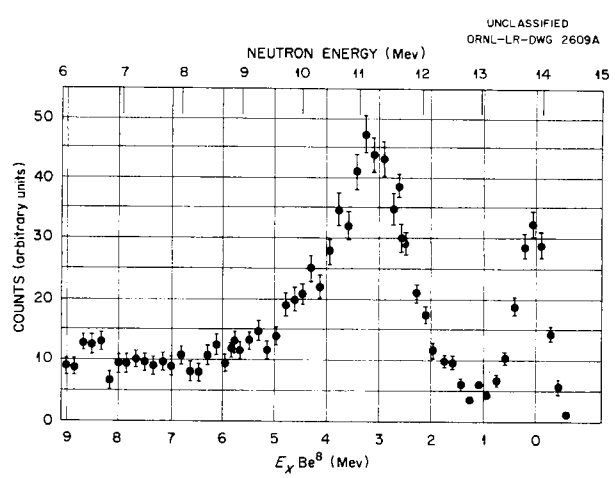

Fig. 1.13. Neutron Spectrum at 120 deg from the $Li^7(d,n)Be^8$ Reaction.

[21] M. E. Calcraft and E. W. Titterton, *Phil. Mag.* **42**, 666 (1951).

[22] M. J. Brinkworth and E. W. Titterton, *Phil. Mag.* **42**, 952 (1951).

[23] H. T. Richards, *Phys. Rev.* 59, 796 (1941).

[24] L. L. Green and W. M. Gibson, *Proc. Phys. Soc. (London)* **62**, 407 (1949).

[25] B. Trumpy, T. Grotdal, and A. Graue, *Nature* **170**, 1118 (1952).

[26] J. Catalá, J. Aguilor, and F. Busquets, *Anales real soc. span. fís. y quím. (Madrid)* **49A**, 131 (1953).

[27] E. K. Inall and A. J. F. Boyle, *Phil. Mag.* **44**, 1081 (1953).

[28] F. E. Steigert and M. B. Sampson, *Phys. Rev.* **92**, 660 (1953).

[29] W. E. Kunz, C. D. Moak, and W. M. Good, *Phys. Rev.* **91**, 676 (1953).

[30] R. Malm and P. R. Inglis, *Phys. Rev.* **92**, 1326 (1953).

[31] P. B. Treacy, *Phil. Mag.* **44**, 325 (1953).

counter without a radiator in place has been subtracted; no data were obtained for lower neutron energies because of an excessive background. These spectra have been corrected for the variation in n-p scattering cross section with energy. In addition, Fig. 1.13 has been corrected for the energy loss in the radiator and in the counter gas and for the attenuation of the neutrons in the iron shield for beta particles.

These spectra show a high-energy neutron group leaving Be^8 in the ground state, another group leaving it in the 3-Mev state, and a continuum arising from the formation of two alpha particles and a neutron. No evidence was found for the existence of levels previously reported in the region of 4-, 5-, and 7.5-Mev excitation.

In order to study the angular distribution of this reaction, the entire spectrum was compressed into one setting of the analyzer and was thereby observed with poor resolution at 10-deg intervals from 0 to 120 deg and at 135 deg. Figure 1.14 shows the angular distribution in millibarns per steradian vs angle in the center-of-mass system for the ground state and 3-Mev excited state. Corrections, such as those stated above, have been made, and the contribution from three-body breakup has been subtracted in an arbitrary but consistent manner. The absolute cross section for these distributions was obtained by bombarding an LiF target of known weight with the same average deuteron energy as that used here. This absolute measurement was made only at 0 deg for the ground state in order to normalize the entire curve.

These two states must have even parity so that if the reaction proceeds by the Butler stripping process[32] the captured proton will have one unit of orbital angular momentum. Qualitatively, the forward peak in the two angular distribution curves can be attributed to the stripping process with the capture of p-wave protons, and the contribution at large angles can be ascribed to compound-nucleus formation.

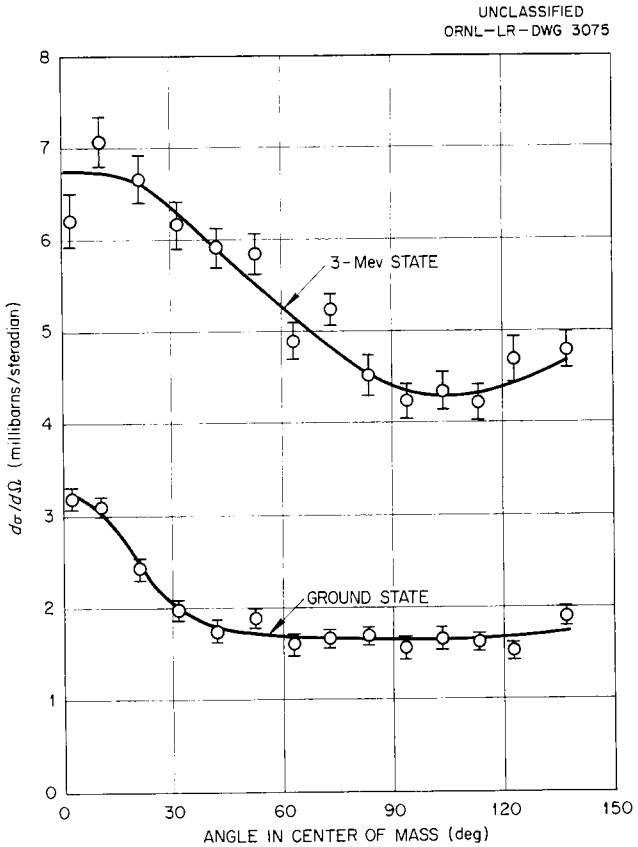

Fig. 1.14. Differential Cross Section in the Center-of-Mass System for the $Li^7(d,n)Be^8$ Leaving Be^8 in the Ground State and First Excited State.

COULOMB EXCITATION

P. H. Stelson F. K. McGowan

Angular Distributions

Alder and Winther,[33] using a semiclassical treatment, have derived explicit expressions for the angular distribution of the gamma radiation following coulomb excitation. If one measures the angular distribution of the gamma radiation with respect to the incident particles, one obtains an angular distribution which is very similar to the angular correlation between two gamma rays in cascade. The distribution function is

$$W(\theta) = 1 + \Sigma_\nu A_\nu a_\nu P_\nu (\cos\theta) \ .$$

The coefficients A_ν are the gamma-gamma angular-correlation coefficients tabulated by Biedenharn and Rose[34] for the spin sequence $j_1(E2)j(L_2)j_2$, where the j's are the spins of the target nucleus, the coulomb excited state, and the final state after gamma-ray emission, respectively. The coefficients

[32] S. T. Butler, *Proc. Roy. Soc.* (*London*) A208, 559 (1951).

[33] K. Alder and A. Winther, *Phys. Rev.* 91, 1578 (1953).

[34] L. C. Biedenharn and M. E. Rose, *Revs. Mod. Phys.* 25, 729 (1953).

a_ν depend on the excitation process, and numerical calculations of the energy dependence of these coefficients for electric quadrupole excitation have been done by Alder and Winther.

Although several workers[35] have reported agreement between theory and experiment for the angular distribution of the 303-kev gamma ray of Ta^{181} and the 550-kev gamma ray of Au^{197}, our measurements have not supported this conclusion. For instance, the energy-dependent coefficient a_2 was observed to be 17% smaller than the theoretical coefficient at $E_p = 4$ Mev for the 303-kev gamma ray in Ta^{181} on the assumption that the spin sequence is $7/2(E2)11/2(E2)7/2$. Since the spin of the coulomb excited state in these odd-mass nuclei was not known with certainty, the angular distributions of the gamma rays from a coulomb excited state of spin 2 have been examined to test the angular-distribution theory. In these cases, the spin of the excited state is known from gamma-gamma directional angular-correlation measurements. The spin sequence $0(E2)2(E2)0$ is particularly suitable because the coefficients A_ν are large. In addition, for the cases that have been examined in these experiments, the gamma-gamma directional angular-correlation measurements have shown no observable influence of extranuclear fields. This point is important for proton-gamma angular-distribution measurements where a target in the solid state is necessary.

Figure 1.15 is the differential pulse-height spectrum of the gamma radiation from platinum for $E_p = 5.0$ Mev. The gamma rays of 330 and 358 kev result from the decay of the known, first excited state in Pt^{194} (32.8%) and Pt^{196} (25.4%), respectively. Finally, the 403-kev gamma ray results from the decay of the first excited state in Pt^{198} (7.2%). This level was not known to exist previously. The proton-gamma angular distribution of the 330- and 358-kev gamma rays taken together has been measured for $E_p = 2.5$ to 5.0 Mev. The results are shown in Fig. 1.16. The solid curves are the thick-target energy-dependent coefficients a_ν deduced from the experimentally observed thick-target yields and the thin-target coefficients a_ν given by Alder and Winther. The observed energy dependence of the coefficients a_ν deviates considerably from the existing theory.

[35] J. T. Eisinger, C. F. Coo, and C. M. Class, *Phys. Rev.* 94, 735 (1954); W. I. Goldburg and R. M. Williamson, *Phys. Rev.* 95, 767 (1954).

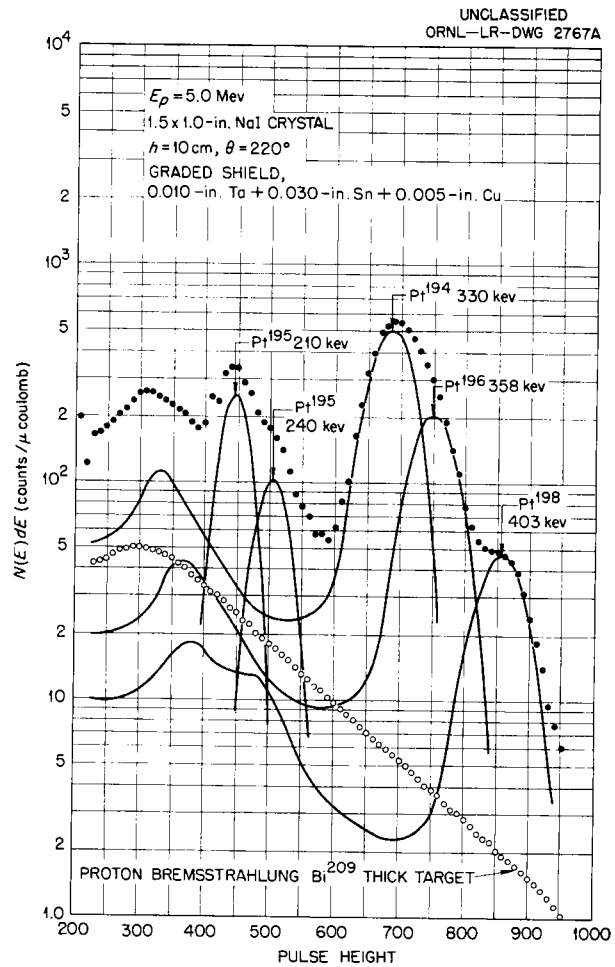

Fig. 1.15. Differential Pulse-Height Spectrum in NaI from Gamma Radiation Produced by Protons on Platinum.

The second excited state in Pt^{194} and Pt^{196} is known to be spin 2. If these states were produced by coulomb excitation, the observed proton-gamma angular distributions would be a composite angular-distribution function. Excitation of the second excited state can be excluded in both isotopes for the following reasons: In Pt^{194} the yield is negligible because the level is at 1.81 Mev; in Pt^{196} the level is at 688 kev and decays 99% of the time by a cascade gamma ray of 330 kev which is 95% $E2$ and 5% $M1$. If it is assumed that the reduced transition probabilities of the 688- and 358-kev transitions are equal, the yield of 330-kev gamma rays by the cascade relative to 330- and 354-kev gamma rays would be 5, 7, 10, and 13% at E_p = 3.5, 4.0, 4.5, and 5.0 Mev, respectively. However,

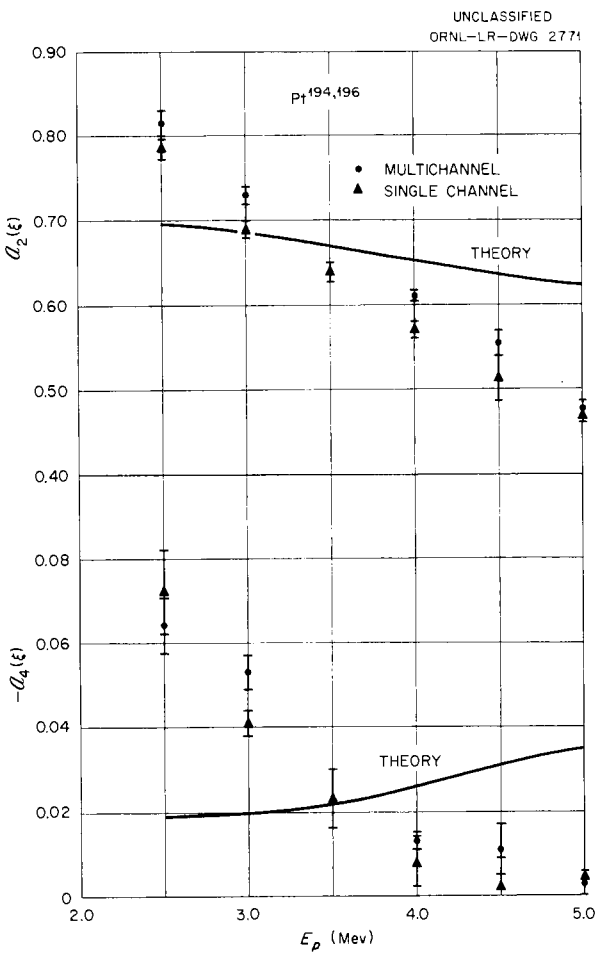

Fig. 1.16. Energy-Dependent Angular-Distribution Coefficients for the 330- and 358-kev Gamma Rays from Pt^{194} and Pt^{196}, as a Function of the Incident-Proton Energy.

the reduced transition probability for the 688-kev transition is probably smaller because the observed reduced transition probability for the 358-kev transition in Pt^{196} is 20 times larger than the theoretical estimates. The assumption above would require the 330-kev cascade reduced transition probability to be 4×10^3 larger, which seems rather unlikely.

A number of other proton-gamma angular distributions have been measured, and the results are listed in Table 1.2. In those cases where the spin for the coulomb excited state is known from other measurements, the energy-dependent coefficients a_ν for thick target are tabulated. The deviations from theory are even larger for the angular distribution of the gamma rays from palladium than they are for the distribution from platinum. An improvement in the angular-distribution theory would be very desirable. In odd-mass nuclei the radiation from the first coulomb excited state and the cascade radiation from the second coulomb excited state will be $E2 + M1$. From the angular-distribution measurements the spin of the excited states can be inferred, and the ratio of the quadrupole-to-dipole intensity can be determined. This information, together with the excitation cross section, is of interest, since the $M1$ reduced transition probability can be directly compared with the static magnetic moment of the ground state.[36]

Observed Gamma Rays, Yields, and Cross Sections

Table 1.3 is a list of the gamma rays we have observed when the indicated target materials were bombarded by protons and alpha particles. Columns 3, 4, 5, and 6 list, respectively, the bombarding particle, its incident energy, the type of target (thick or thin) used, and the observed yield in number of gamma rays per microcoulomb. The bombarding alpha particles were singly ionized so that for both protons and alpha particles there were 6.25×10^{12} incident particles per microcoulomb. In all cases metallic targets were used.

Measurements of the variation in yield with proton energy have been carried out for the 137-, 166-, and 303-kev gamma rays in Ta^{181} with both thick and thin targets and for the (277 + 273)- and 550-kev gamma rays in Au^{197} with a thin target. These yields are given in Tables 1.4, 1.5, and 1.6. For the thick-target tantanlum yields the counter was located at 45 deg to the forward direction. The thin-target yields were observed at 0 deg. The thin targets were prepared by mounting thin foils (Ta, 10.0 mg/cm^2, and Au, 10.5 mg/cm^2) on bismuth backings. In all cases the yields have been corrected for the bremsstrahlung continuum by measuring the spectrum from a bismuth target. Bismuth is well suited to this purpose because of the absence of gamma rays from coulomb excitation. We believe that the extrapolation from $Z = 83$ (Bi) to $Z = 73$ (Ta) will

[36] A. Bohr and B. Mottelson, *Kgl. Danske Videnskab. Selsk. Mat. fys. Medd.* 27, 16 (1953).

TABLE 1.2. PROTON-GAMMA ANGULAR-DISTRIBUTION COEFFICIENTS

Nucleus	E (kev)	E_p (Mev)	Spin Sequence	(a_2A_2)exp	(a_2)exp	(a_4A_4)exp	(a_4)exp
Ta^{181}	303	4.0		0.089 ± 0.004		−(0.006 ± 0.004)	
	166	4.0		0.112 ± 0.006		0.021 ± 0.008	
Au^{197}	550	4.0		0.164 ± 0.004		−(0.018 ± 0.005)	
	277	4.0		−(0.115 ± 0.004)		0.003 ± 0.005	
$Pt^{194,196}$	330, 358	2.5	0(E2)2(E2)0	0.291 ± 0.006	0.816 ± 0.016	−(0.074 ± 0.007)	−(0.064 ± 0.007)
		2.5	0(E2)2(E2)0	0.280 ± 0.004	0.785 ± 0.012	−(0.083 ± 0.013)	−(0.072 ± 0.011)
		3.0	0(E2)2(E2)0	0.261 ± 0.004	0.730 ± 0.010	−(0.061 ± 0.005)	−(0.053 ± 0.004)
		3.0	0(E2)2(E2)0	0.246 ± 0.003	0.688 ± 0.008	−(0.047 ± 0.003)	−(0.041 ± 0.003)
		3.5	0(E2)2(E2)0	0.227 ± 0.003	0.637 ± 0.008	−(0.026 ± 0.008)	−(0.023 ± 0.007)
		4.0	0(E2)2(E2)0	0.218 ± 0.002	0.609 ± 0.003	−(0.015 ± 0.002)	−(0.013 ± 0.002)
		4.0	0(E2)2(E2)0	0.204 ± 0.003	0.571 ± 0.007	−(0.009 ± 0.006)	−(0.008 ± 0.006)
		4.5	0(E2)2(E2)0	0.198 ± 0.006	0.555 ± 0.015	−(0.013 ± 0.007)	−(0.011 ± 0.006)
		4.5	0(E2)2(E2)0	0.183 ± 0.010	0.513 ± 0.028	−(0.003 ± 0.007)	−(0.002 ± 0.007)
		5.0	0(E2)2(E2)0	0.170 ± 0.002	0.475 ± 0.007	−(0.004 ± 0.003)	−(0.003 ± 0.003)
		5.0	0(E2)2(E2)0	0.168 ± 0.003	0.471 ± 0.008	0.006 ± 0.003	0.005 ± 0.003
Rh^{103}	305	2.5		−(0.255 ± 0.003)		0.007 ± 0.004	
	365	2.5	1/2(E2)5/2(E2)1/2*	0.227 ± 0.003	0.795 ± 0.011	−(0.023 ± 0.004)	−(0.060 ± 0.011)
$Pd^{110?}$	380	2.5	0(E2)2(E2)0	0.270 ± 0.004	0.756 ± 0.011	−(0.050 ± 0.007)	−(0.044 ± 0.006)
$Pd^{108?}$	445	2.5		0.255 ± 0.009		−(0.071 ± 0.008)	
Pd^{106}	513	2.5	0(E2)2(E2)0	0.341 ± 0.005	0.954 ± 0.14	−(0.108 ± 0.018)	−(0.094 ± 0.016)
$Ag^{107,109}$	325	2.5		−(0.282 ± 0.004)		0.007 ± 0.007	
	427	2.5	1/2(E2)5/2(E2)1/2*	0.248 ± 0.004	0.868 ± 0.14	−(0.039 ± 0.009)	−(0.102 ± 0.024)

*Suggested from the position of energy level by Heydenburg and Temmer.

TABLE 1.3. GAMMA RAYS OBSERVED WHEN LISTED ELEMENTS WERE BOMBARDED BY PROTONS AND/OR ALPHA PARTICLES[a]

Target Material (Metallic)	Gamma-Ray Energy, E_γ (kev)	Bombarding Particle[b]	Energy, E, of Bombarding Particle (Mev)	Type of Target	Yield (number of gamma rays per microcoulomb of incident particles)
Th	53 ± 3	α	4.0	Thick	
	760 ± 10	p	5.0	Thick	3.32×10^4
Pb^{206}[c]	810 ± 10	p	5.0	Thick	4.92×10^4
Tl	205 ± 3	p	4.0	Thick	7.72×10^4
		α	4.0	Thick	2.60×10^3
	279 ± 3	p	4.0	Thick	3.90×10^4
		α	4.0	Thick	4.25×10^2
	410 ± 5	p	4.0	Thick	1.50×10^4
Au	191 ± 3	p	4.0	Thick	5.42×10^4
		α	4.0	Thick	7.44×10^2
	273[d]	p	4.0	Thick	4.46×10^3
		p		Thin	See Table 1.6
	277 ± 3	p		Thin	See Table 1.6
		p	4.0	Thick	2.92×10^5
		α	4.0	Thick	3.50×10^3
	550 ± 5	p		Thin	See Table 1.6
		p	4.0	Thick	1.16×10^5
Pt	100 ± 3	α	4.0	Thick	
	130 ± 3	α	4.0	Thick	
	210 ± 3	p	5.0	Thick	3.57×10^5
	240 ± 3	p	3.0, 4.0, 5.0	Thick	1.67×10^5[e]
	330 ± 5	p	2.5 to 5.0	Thick	1.35×10^6[e]
	358 ± 5	p	2.5 to 5.0	Thick	6.38×10^5[e]
	403 ± 5	p	2.5 to 5.0	Thick	1.89×10^5[e]
W	112[f]	p	4.0	Thick	2.87×10^6
	295 ± 5	p	4.0	Thick	1.08×10^4
Ta	137 ± 2	p		Thin	See Table 1.5
		p		Thick	See Table 1.4
		α	4.0	Thick	2.05×10^5
	167 ± 3	p		Thin	See Table 1.5
		p		Thick	See Table 1.4
		α	4.0	Thick	
	303 ± 3	p		Thin	See Table 1.5
		p		Thick	See Table 1.4
Hf	90 ± 3	p	4.0	Thick	1.74×10^6
	112 ± 3	p	4.0	Thick	5.33×10^5
	248 ± 5	p	4.0	Thick	1.19×10^5
Ag	104 ± 3	p	2.1 to 2.9	Thick	1.32×10^4[g]
	325 ± 5	p	2.1 to 2.9	Thick	3.45×10^5[g]
	427 ± 5	p	2.1 to 2.9	Thick	2.89×10^5[g]

TABLE 1.3. (continued)

Target Material (Metallic)	Gamma-Ray Energy, E_γ (kev)	Bombarding Particle[b]	Energy, E, of Bombarding Particle (Mev)	Type of Target	Yield (number of gamma rays per microcoulomb of incident particles)
Pd	380 ± 5	p	2.1 to 2.9	Thick	1.32×10^{5}[g]
	445 ± 5	p	2.1 to 2.9	Thick	2.29×10^{5}[g]
	520 ± 7	p	2.1 to 2.9	Thick	1.14×10^{5}[g]
	575 ± 10	p	2.1 to 2.9	Thick	2.55×10^{4}[g]
Rh	65 ± 3	p	2.1 to 2.9	Thick	2.76×10^{4}[g]
	305 ± 5	p	2.1 to 2.9	Thick	4.18×10^{5}[g]
	365 ± 5	p	2.1 to 2.9	Thick	4.44×10^{5}[g]
Mo	212 ± 3	p	2.1 to 2.9	Thick	2.26×10^{4}[g]
	540 ± 7	p	2.1 to 2.9	Thick	4.64×10^{4}[g]

[a]Singly ionized alpha particles were used.
[b]α, alpha particles; p, protons.
[c]Target made of radiogenic lead enriched to 88% Pb^{206}.
[d]Existence of this gamma ray was established from coincidence measurements.
[e]Yield for 5.0-Mev protons.
[f]Observed width too large for a single gamma ray (see McClelland *et al.*[44]).
[g]Yield for 2.9-Mev protons.

give little error, since our investigations of the bremsstrahlung process show relatively little change in character for this amount of change in Z. The relative accuracy of the yield values is approximately 5% except where noted, and the absolute accuracy is 10 to 20%. We have also listed in Tables 1.5 and 1.6 the mean proton energies based on the integration of theory (Alder and Winther) over the thickness of the foil.

From these gamma-ray yields we have deduced cross sections for excitation of the levels involved. The following values were taken for the total internal conversion coefficients of the gamma rays: Ta, 137, 2.09 (ref. 37); Ta, 166, 1.11 (ref. 38); Ta, 303, 7.93×10^{-2} (ref. 39); Au, 277, 0.36 (ref. 40); Au, 550, 1.6×10^{-2} (ref. 39); Au, 273, 0.36 (value is not known; we have rather arbitrarily taken it to be the same as for the 277-kev gamma ray). We find that for the 303-kev level in Ta^{181} the ratio of the number of decays by cascade to the number of decays by cross-over is 3.50. For the 550-kev level in Au^{197} this number is 0.06 (obtained from coincidence measurements).

The calculation of the cross section from thick-target yields and the calculation of the mean proton energies for thin-target yields require the knowledge of the rate of energy loss of the protons as a function of energy. Allison and Warshaw[41] have recently reviewed this subject. We have taken their recommended values for $dE/d(\rho x)$ for protons in gold. However, this extends only to 2.0 Mev. We have extrapolated to higher energies by means of a theoretical curve. The stopping power of tantalum was calculated from this curve on the assumption that stopping power in units of kev/mg/cm^2 varies as $Z^{-1/2}$.

The excitation cross sections for the 137- and 303-kev levels in Ta^{181} are shown in Fig. 1.17. Since the cross-section values deduced from the thick-target yields require differentiation of the yield curve, there are errors caused by the uncertainty in finding the derivative, especially near the ends of the yield curve. Figure 1.18 shows the cross sections for excitation of the 277- and 550-kev levels of Au^{197}.

[37]F. K. McGowan, *Phys. Rev.* 93, 471 (1954).
[38]T. Huus and T. H. Bjerregaard, *Phys. Rev.* 92, 1579 (1953).
[39]M. E. Rose *et al.*, *Phys. Rev.* 83, 79 (1951).
[40]O. Huber *et al.*, *Helv. Phys. Acta* 26, 591 (1953).
[41]S. K. Allison and S. D. Warshaw, *Revs. Mod. Phys.* 25, 779 (1953).

TABLE 1.4. THICK-TARGET YIELDS OF THE 137-, 166-, AND 303-kev GAMMA RAYS OF Ta^{181} GIVEN AS NUMBER OF GAMMA RAYS PER MICROCOULOMB OF PROTONS

Incident-Proton Energy, E_p (Mev)	I_{137} ($\times 10^{-5}$)	I_{166} ($\times 10^{-4}$)	I_{303} ($\times 10^{-4}$)
2.00	1.54	0.527	0.284
2.10	1.98	0.782	0.421
2.20	2.50	1.10	0.591
2.30	2.92	1.52	0.819
2.40	3.68	2.14	1.15
2.50	4.22	2.76	1.49
2.60	5.08	3.64	1.96
2.70	6.00	4.48	2.41
2.80	6.83	5.64	3.04
2.90	7.95	7.21	3.88
3.00	8.60	8.26	4.45
3.20	11.2	11.6	6.41
3.40	13.9	15.3	8.48
3.60	16.5	19.8	10.9
3.80	20.5	25.7	14.2
4.00	23.2	30.3	16.8
4.20	27.9	40.1	22.1
4.40	32.7	46.1	25.4
4.60	37.6	52.9	29.2
4.80	43.4	63.0	34.8

TABLE 1.5. THIN-TARGET YIELDS OF THE 137-, 166-, AND 303-kev GAMMA RAYS OF Ta^{181} GIVEN AS NUMBER OF GAMMA RAYS PER MICROCOULOMB OF PROTONS[a]

Incident-Proton Energy, E_p (Mev)	I_{137} ($\times 10^{-4}$)	I_{166} ($\times 10^{-3}$)	I_{303} ($\times 10^{-2}$)
1.43	2.44		0.60[b]
1.60	4.28		3.62[c]
1.80	7.70	2.53	11.3[d]
2.00	11.8	5.34	28.9
2.20	16.0	11.0	57.2
2.40	20.0	17.7	100
2.60	24.7	26.2	148
2.80	30.2	38.2	211
3.00	34.2	48.5	280
3.20	37.5	59.7	341
3.40	43.3	76.5	408
3.60	47.7	86.9	480
3.80	50.5	93.9	538
4.00	54.4	105	591
4.20	57.8	118	674
4.40	59.2	123	725
4.60	64.7	133	777
4.80	70.2	143	847
5.00	72.6	156	931

[a]The target was a foil 10.5 mg/cm^2 in thickness mounted on a bismuth backing.

[b]Relative accuracy: +75%, −35%.

[c]Relative accuracy: +45%, −20%.

[d]Relative accuracy: ±7%.

The curves shown in Figs. 1.17 and 1.18 are those given by theory. In calculating the theoretical curves we have used the difference in the reciprocal velocities before and after collision to calculate the parameter ξ. The general agreement between theory and experiment is good.

In Table 1.7 we give our present interpretation of the experimental data given in the previous tables. The values of the reduced transition probabilities, $B_e(2)/e^2$, are of particular interest. To obtain these it is first necessary to evaluate the quantity

$$\int \frac{g_2(\xi)E\Delta E}{\Delta E/\Delta(\rho x)} .$$

We list our values of this quantity in units of kev × mg/cm^2. The fact that the values of $B_e(2)/e^2$ for a given transition are nearly the same for different conditions of excitation, e.g., proton and alpha-particle bombardment, is additional support for the theory of coulomb excitation. We also list values of Q_0 for the spin assignment, I, of the excited state.

From the knowledge of $B_e(2)/e^2$ and the percentage of the time the state decays by the emission of an $E2$ gamma ray, it is possible to predict the lifetime of the state. We list the values of the calculated half lives in the column headed by $T_{1/2}$. In several cases the half lives have been measured directly, and it is of interest to compare values obtained by the two methods. The half life of the Hf^{176} 90-kev state has been measured to be 1.35×10^{-9} sec by McGowan.[42]

[42]F. K. McGowan, *Phys. Rev.* 87, 542 (1952).

TABLE 1.6. THIN-TARGET YIELDS OF THE 277-, 273-, AND 550-kev GAMMA RAYS FROM Au^{197} GIVEN AS NUMBER OF GAMMA RAYS PER MICROCOULOMB OF PROTONS[a]

Incident-Proton Energy, E_p (Mev)	$I_{277,273}$ ($\times 10^{-3}$)	I_{550} ($\times 10^{-3}$)
1.60	0.315[b]	
1.80	1.34[c]	
2.00	3.95	
2.20	7.32	0.326[d]
2.40	13.1	1.07[e]
2.60	19.2	2.80[f]
2.80	27.8	6.41
3.00	35.4	11.6
3.20	44.0	19.1
3.40	54.6	29.3
3.60	64.3	40.0
3.80	75.3	52.9
4.00	83.5	66.9
4.20	93.4	83.7
4.40	103	99.9
4.60	117	118
4.80	123	135
5.00	129	156

[a]The target was a foil 10.5 mg/cm^2 in thickness mounted on a bismuth backing.
[b]Relative accuracy: ±15%.
[c]Relative accuracy: ±7%.
[d]Relative accuracy: ±15%.
[e]Relative accuracy: ±10%.
[f]Relative accuracy: ±7%.

Recently, Sunyar[43] measured the half life of the 90-kev state in Hf^{180} and found the value to be 1.39×10^{-9} sec. Sunyar[43] also measured the half life of the 100-kev state in W^{182} and obtained a value of 1.27×10^{-9} sec. For the hafnium states the value deduced from coulomb excitation agrees well with the directly measured values. The agreement for the W^{182} state is also quite good when one remembers that the half life is connected to $B_e(2)/e^2$ by the fifth power of the energy. The average value of 112 kev for the three even isotopes was taken in calculating the value listed. When we take, instead, 100 kev, which is the excitation energy[44] in W^{182}, we get 1.35×10^{-9} sec, as compared to the direct value of 1.27×10^{-9} sec.

[43]A. W. Sunyar, *Phys. Rev.* 95, 626 (1954).

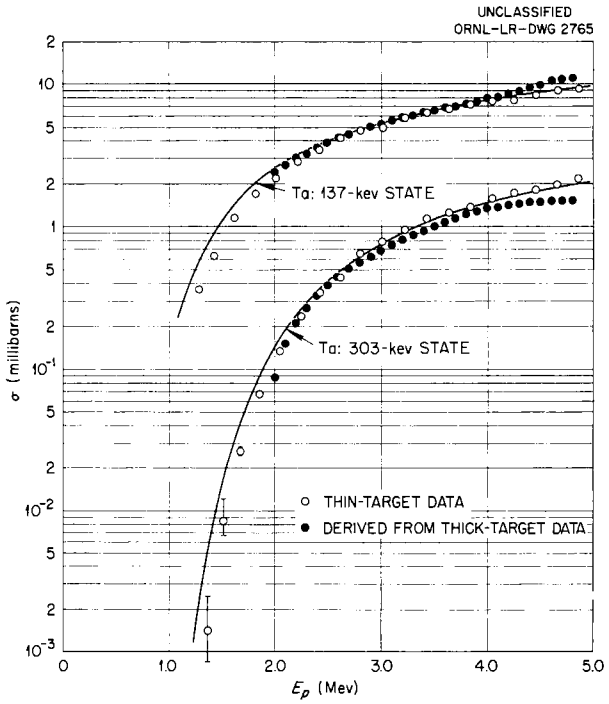

Fig. 1.17. Cross Section in Millibarns for the Excitation of the 137- and 303-kev Levels in Ta^{181}. The open circles are values derived from the thick-target yields listed in Table 1.4. The solid circles are obtained from thin-target (10.0 mg/cm^2) yield measurements. At low proton energies the cross section changes rapidly and the thin target is no longer very thin, so that there is some uncertainty in the proton energies taken in plotting the values of the cross section.

GAMMA RAYS FROM BORON AND CARBON-13 BOMBARDED BY PROTONS

J. K. Bair J. D. Kington
H. B. Willard

The work reported in the last semiannual report (ORNL-1705) under the heading, "Gamma-Ray Spectrum and Gamma-Ray Yield from Boron Bombarded by Protons," has been extended to above 5-Mev proton bombarding energy with the use of

[44]C. L. McClelland, H. Mark, and C. Goodman, *Phys. Rev.* 93, 904 (1954).

TABLE 1.7. INTERPRETATION OF DATA FROM TABLES 1.3 TO 1.6 IN TERMS OF THE THEORY OF COULOMB EXCITATION

Nucleus	Excitation Energy, E (kev)	Bombarding Particle[a]	Energy of Bombarding Particle, E' (Mev)	Type of Target	Yield[b] or Cross Section, σ	$\int \frac{g_2(\xi)E\Delta E}{\Delta E/\Delta(px)}$	$\frac{B_e(2)}{e^2}$ ($\times 10^{48}$)[c]	Lifetime for Decay of Excited State, $T_{1/2}$ (sec)	Spin Value Taken for Excited State, I	Q_0 Calculated from $B_e(2)/e^2$ (cm$^2 \times 10^{24}$)
$_{72}Hf^{176,178,180}$	90	p	4.0	Thick	1.83×10^7	1.99×10^5	5.96	1.13×10^{-9}[d]	2	7.74
$_{73}Ta^{181}$	137	p	2.0	Thin	2.58		2.52	3.77×10^{-11}	9/2	7.73
		p	2.0	Thick	4.64×10^5	1.57×10^4	2.00	4.77×10^{-11}		6.89
		p	4.0	Thick	6.60×10^6	1.87×10^5	2.39	4.01×10^{-11}		7.53
		α	4.0	Thick	6.63×10^5	6.18×10^3	1.76	5.41×10^{-11}		6.47
	303	p	2.0	Thin	0.140		0.597	1.14×10^{-11}	11/2	7.43
		p	2.0	Thick	1.45×10^4	2.13×10^3	0.461	1.47×10^{-11}		6.52
		p	4.0	Thick	8.35×10^5	1.14×10^5	0.495	1.37×10^{-11}		6.75
$_{74}W^{182,184,186}$	112	p	4.0	Thick	1.40×10^7	1.96×10^5	5.05	7.65×10^{-10}[e]	2	7.11
$_{78}Pt^{194}$	330	p	4.0	Thick	1.74×10^6	9.03×10^4	1.60	4.21×10^{-11}	2	4.01
		p	5.0	Thick	4.42×10^6	2.31×10^5	1.59	4.23×10^{-11}		4.00
$_{78}Pt^{196}$	358	p	4.0	Thick	1.21×10^6	8.02×10^4	1.26	3.59×10^{-11}	2	3.56
		p	5.0	Thick	2.66×10^6	2.16×10^5	1.03	4.42×10^{-11}		3.22
$_{78}Pt^{198}$	403	p	4.0	Thick	9.02×10^5	6.45×10^4	1.17	2.19×10^{-11}	2	3.43
		p	5.0	Thick	2.72×10^6	1.88×10^5	1.21	2.11×10^{-11}		3.49
$_{79}Au^{197}$	(191)	p	4.0	Thick	1.13×10^5	1.55×10^5	(0.0629)			
		α	4.0	Thick	1.55×10^3	1.98×10^3	(0.0167)			
	268	p	4.0	Thick	1.13×10^5	1.17×10^5	0.0833			
		α	4.0	Thick	1.55×10^3	4.46×10^2	0.0750			
	277	p	3.0	Thin	0.290		0.262	7.28×10^{-11}	5/2	2.26
		p	4.0	Thick	3.98×10^5	1.12×10^5	0.307	6.21×10^{-11}		2.45
		α	4.0	Thick	4.76×10^3	3.92×10^2	0.262	7.28×10^{-11}		2.26
	550	p	3.0	Thin	0.0920		0.434	5.09×10^{-12}	7/2	3.91
		p	4.0	Thick	1.17×10^5	3.00×10^4	0.336	6.62×10^{-12}		3.43
$_{81}Tl^{203}$	279	p	4.0	Thick	1.46×10^5	1.13×10^5	0.121	3.67×10^{-10}	3/2	1.75
		α	4.0	Thick	1.90×10^3	3.66×10^2	0.123	3.61×10^{-10}		1.76
	682	p	4.0	Thick	1.69×10^4	1.38×10^4	0.117	1.19×10^{-2}	5/2	1.40
$_{81}Tl^{205}$	205	p	4.0	Thick	1.93×10^5	1.44×10^5	0.127		3/2	1.78
		α	4.0	Thick	6.49×10^3	1.28×10^3	0.128			1.80
	615	p	4.0	Thick	2.11×10^4	2.03×10^4	0.0981		5/2	1.28

[a] α, alpha particle; p, protons.

[b] Yield in excitation per microcoulomb of incident particle for thick targets (singly ionized alpha particles were used) or cross section in millibarns for thin targets.

[c] $B_e(2)/e^2$ is the reduced transition probability (in cm^4) for exciting the nucleus from the ground state to the excited state by electric quadrupole excitation.

[d] Direct measurement of lifetime for Hf^{176} gives 1.35×10^{-9} sec (McGowan[42]); direct measurement of lifetime for Hf^{180} gives 1.39×10^{-9} sec (Sunyar[43]).

[e] Direct measurement of lifetime of the 100-kev level in W^{182} gives 1.27×10^{-9} sec (Sunyar,[43] see text).

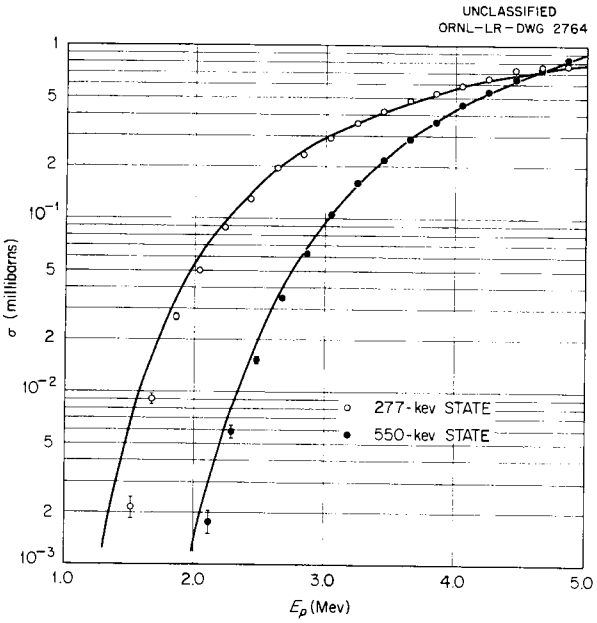

Fig. 1.18. Cross Section in Millibarns for the Excitation of the 277- and 550-kev Levels in Au^{197}. The points are based on the yield of gamma rays from a thin target (10.5 mg/cm^2). At low proton energies the cross section changes rapidly and the thin target is no longer very thin, so that there is some uncertainty in the proton energies taken in plotting the values of the cross section.

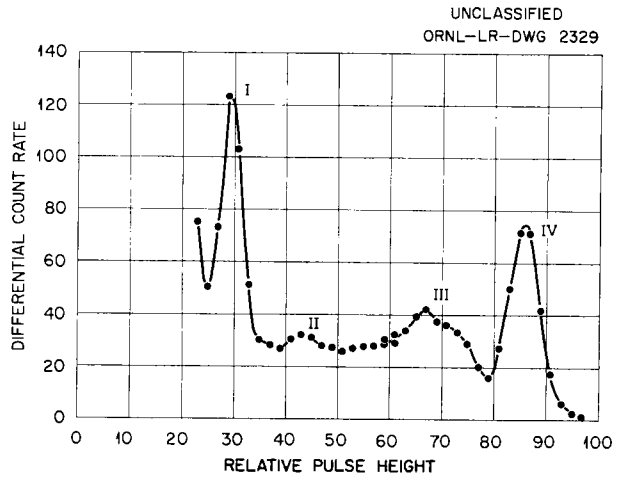

Fig. 1.19. Gamma-Ray Spectrum Taken at a Proton Energy of 2.8 Mev for $B^{10}(p,p')B^{10*}(\gamma)B^{10}$ and $B^{11}(p,p')B^{11*}(\gamma)B^{11}$.

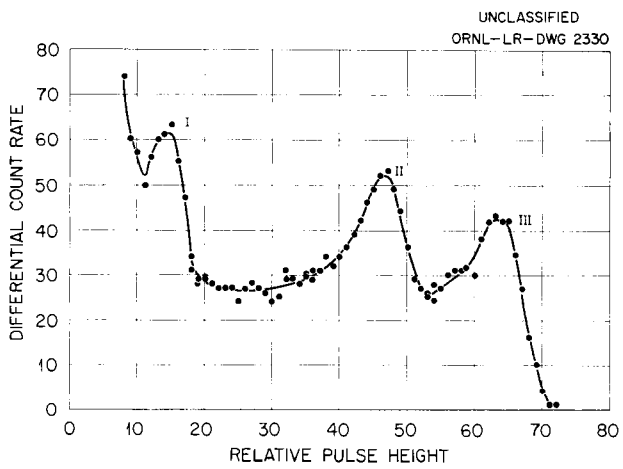

Fig. 1.20. $B^{11}(p,\gamma)C^{12}$ Gamma-Ray Spectrum Taken at a Proton Energy of 1.4 Mev.

new boron targets of greater chemical purity. In addition to the previously reported capture-gamma-ray yields, the inelastic-scattering gamma-ray yields resulting from the $B^{11}(p,p')B^{11*}(\gamma)B^{11}$ reaction are given for proton bombarding energies from 2.6 to 5.3 Mev.

The fact that the new targets did indeed have higher chemical purity is shown by Fig. 1.19, which gives the spectrum of the gamma rays, below 2.5-Mev energy, which resulted when a natural-isotopic-mixture boron target was bombarded with 2.8-Mev protons. The large, 3 × 3 in., sodium iodide crystal counter was used to obtain these data. Peak I is the full energy peak due to the 0.72-Mev gamma ray from the reaction $B^{11}(p,p')B^{11*}(\gamma)B^{11}$. These spectra show no indication of the impurity peaks discussed in the previous report.

Figure 1.20 shows a differential pulse-height curve of the B^{11} capture gamma rays for a bombarding proton energy (1.4 Mev) well below the threshold for neutron production. The maximum labeled I is due to the gamma ray from the 4.4-Mev excited state in C^{12}, with the usual three peaks unresolved due to a wide window width in the pulse-height analyzer. Peaks II and III correspond to the capture transition to the 4.4-Mev state in C^{12} and to the ground state, respectively. It is to be noted that the peaks caused by target impurities in the earlier work do not appear here.

The top two curves of Fig. 1.21 represent the yield of the capture gamma rays as measured at 0 deg to the proton beam. The middle two curves

are for measurements taken at 90 deg. The crosses are for the transition direct to the ground state of C^{12}, whereas the solid points are for the transition to the 4.4-Mev excited state. A preliminary run on the B^{10} capture gamma ray taken at 90 deg to the proton beam, made for the purpose of checking any possible effects of the B^{10} content of the natural-boron targets, indicated only a single broad (~0.5-Mev) level at a proton energy of about 4 Mev. The lower curve of Fig. 1.21 is the yield of the 2.1-Mev gamma rays from the reaction $B^{11}(p,p')B^{11*}(\gamma)B^{11}$ and was measured at 0 deg to the proton beam. A similar curve taken at 90 deg differed in no essential respects and is not shown. Table 1.8 gives the figures on the gamma-ray resonances, uncorrected for target thickness (about 50 kev at 3-Mev proton energy). Column 1 lists arbitrary numbers assigned to the observed levels for identification purposes; column 2, the energy of the proton beam for 0-deg resonances in the "12-Mev" gamma ray; column 3, the same data at 90 deg; column 4, the energy of the proton beam for 0-deg resonances in the "16-Mev" gamma ray; column 5, the same data at 90 deg; column 6, the proton energy for the 2.1-Mev inelastic-scattering gamma-ray resonances; column 7, the proton resonances from the $B^{11}(p,n)C^{11}$ reaction for comparison; and column 8, the energy of excitation in the C^{12} compound nucleus.

Thin carbon targets (approximately 5 kev at 3 Mev) were prepared by cracking methyl iodide vapor on platinum. The methyl iodide was obtained from Eastman Kodak Company with a C^{13} enrichment of 61%. Capture gamma rays produced by

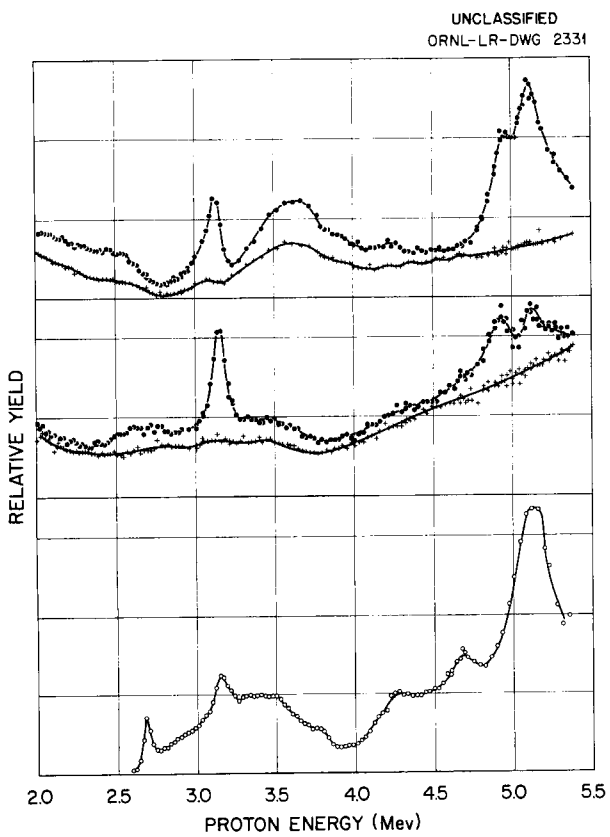

Fig. 1.21. Gamma-Ray Yield from $B^{11}(p,\gamma)C^{12}$ in the Forward Direction (top pair of curves); Similar Data at 90 deg (middle pair of curves). Solid points represent the transition to the 4.4-Mev state in C^{12}, and the crosses represent transitions to the ground state. The bottom curve is the 0-deg yield of the 2.1-Mev gamma rays resulting from the reaction $B^{11}(p,p')B^{11*}(\gamma)B^{11}$.

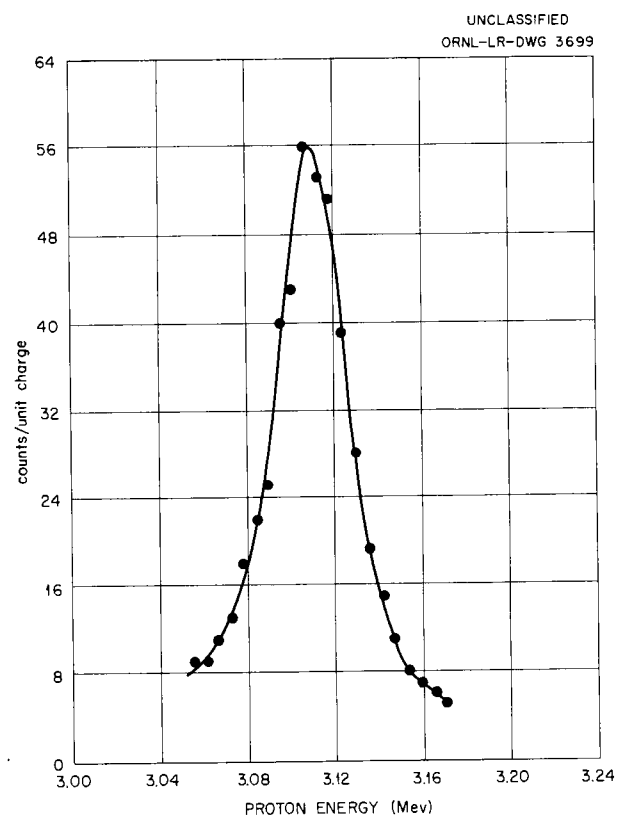

Fig. 1.22. Gamma-Ray Resonance at 3.11 Mev from the Proton Bombardment of C^{13}.

TABLE 1.8. DATA ON GAMMA-RAY RESONANCES, UNCORRECTED FOR TARGET THICKNESS

Level	$\gamma_{12}0^\circ$	$\gamma_{12}90^\circ$	$\gamma_{16}0^\circ$	$\gamma_{16}90^\circ$	$\gamma_{inel.}$	Neutrons	$E_{ex.}$
1	2.5	2.65	Weak				18.33
2					2.67		18.40
3	3.13	3.15	Weak		3.15	3.18	18.84
4	3.65	3.5	3.6	Weak	3.4	3.63	19.2
5					3.78		19.42
6						4.06	19.67
7	Weak				4.26		19.86
8					4.68	4.70	20.25
9	4.97	4.93					20.49
10	5.12	5.12			5.13		20.64

proton bombardment were detected with a 3 × 3 in. NaI(Tl) crystal located $9\frac{1}{8}$ in. from the target (mounted at 45 deg with respect to the proton beam). The ground-state transition exhibits a strong resonance at E_p = 3.11 Mev (Γ = 30 kev) as shown in Fig. 1.22.

Angular distributions of this 10.43-Mev gamma ray fit the expansion

$$W(\theta) = 1 - A_2 P_2(\cos\theta) \quad .$$

A ratio of the yield at 0 deg to that at 90 deg gives the coefficient without correction for absorption in the target backing. The measured value is $A_2 = 0.40 \pm 0.02$.

Analysis of these data by the method of Biedenharn and Rose[45] leads to the conclusion that this level is formed by the capture of d-wave protons to give on excited state in N^{14} of $J = 2^-$, followed by electric dipole radiation to the ground state (1^+). The mixing ratio of channel spin 0 to channel spin 1 is 3 to 2, in agreement with either j-j or Russell-Saunders coupling.

[45] L. C. Biedenharn and M. E. Rose, *Revs. Mod. Phys.* 25, 729 (1953).

2. RADIOACTIVITY AND NUCLEAR ISOMERISM

IMPROVED TOTAL-ABSORPTION SPECTROMETER

P. R. Bell
G. G. Kelley
N. H. Lazar
C. C. Harris
R. C. Davis
J. H. Neiler
R. R. Hall
R. H. Sampley

The largest sodium iodide crystal that we have been able to obtain is still far too small to make a good total-absorption spectrometer. The crystal is equivalent to a sphere of NaI about 5¼ in. in diameter and would have to be about 10 in. in diameter for essentially complete absorption.

A very great improvement in the response has been obtained by surrounding the crystal and its photomultiplier with a large tank of solution phosphor with its own photomultipliers. The energy resolution of a large solution phosphor is much too poor to use it alone or to add its signal to that of the sodium iodide. The response, however, is quite satisfactory if the solution phosphor is used as an anticoincidence counter so that only those pulses in the sodium iodide counter are recorded that have no simultaneous count in the solution counter.

By the use of this anticoincidence arrangement, the Compton pulse part of the gamma-ray response is reduced by a factor of 8 to 10 times for both the large crystal and for a 3-in.-dia, 3-in.-long sodium iodide crystal.

The solution phosphor is contained in a sheet-iron tank of roughly spherical shape with a large re-entrant aluminum tube. The re-entrant tube has a large 0.005-in. window section opposite the crystal. A solution phosphor tank with its own photomultiplier plugs up the unused part of the re-entrant tube. Details are shown in Fig. 2.1. The four DuMont type 6364, 5-in. photomultipliers are arranged approximately at the corners of an inscribed tetrahedron for best optical coverage of the tank. The interior of the tank is coated with a special α-alumina–sodium silicate mixture of very high reflectivity (separately reported). The solution phosphor is xylene (redistilled over sodium) with 5 g of *p*-terphenyl per liter and 10 mg of α-naphthylphenyloxazole fluor converter per liter. The phototubes in contact with the solution must be operated with their cathodes grounded to prevent destructive leakage through the glass faces. This is a difficult arrangement never used in our regular spectrometers and requires special care in the amplifier input circuits.

Outputs from all the solution phosphor tubes are paralleled and applied to the input of an especially modified A-1 amplifier. Every pulse in the tank must disable the analyzer. The unmodified A-1's pulse-height selector was not suitable, therefore, because it has a dead time associated with each firing. Figure 2.2 is a diagram showing the modified circuit. The discriminator is adjusted to have a flat frequency response, which causes it to recover essentially instantly when the input grid returns to its normal value. The signal from the plate of V-1 is limited and lengthened to provide a minimum pulse length of about 2 μsec for all signals out of V-1 large enough to limit. Other changes in the pulse-height selector were necessitated by the fact that the duty cycle may run above 30%.

The overload characteristics of the amplifier had to be modified because of the very large overload effects produced by cosmic-ray pulses in the tank. The input time constant was reduced to 0.65 μsec, and the normal differential time constant was increased to 0.36 μsec, which double-differentiated the signal. Two germanium diodes with opposite polarities were shunted to ground across the gain-control switch, strongly limiting the signal at this point, and anti-overshoot diodes were added at the plates of the second and third tubes in the first feedback group. These changes cause extreme gain nonlinearity, but linearity is not needed in this amplifier.

Because of the high duty cycle it was necessary to add an 80-μf condenser to ground from the +70-v bus supplying the gate tube in the 20-channel analyzer and to short the gate input coupling condenser.

Because fluctuations in anticoincidence counting rate change the dead time and, therefore, the counting loss in the analyzer, the average dead time during a run must be known. A device has been made that will record the dead time continuously; the circuit diagram of this device is shown in Fig. 2.3. An essentially constant current of 0.18 ma flows in the common cathode circuit of both tubes. Tube V-1 is biased sufficiently positive with respect to V-2 that it normally

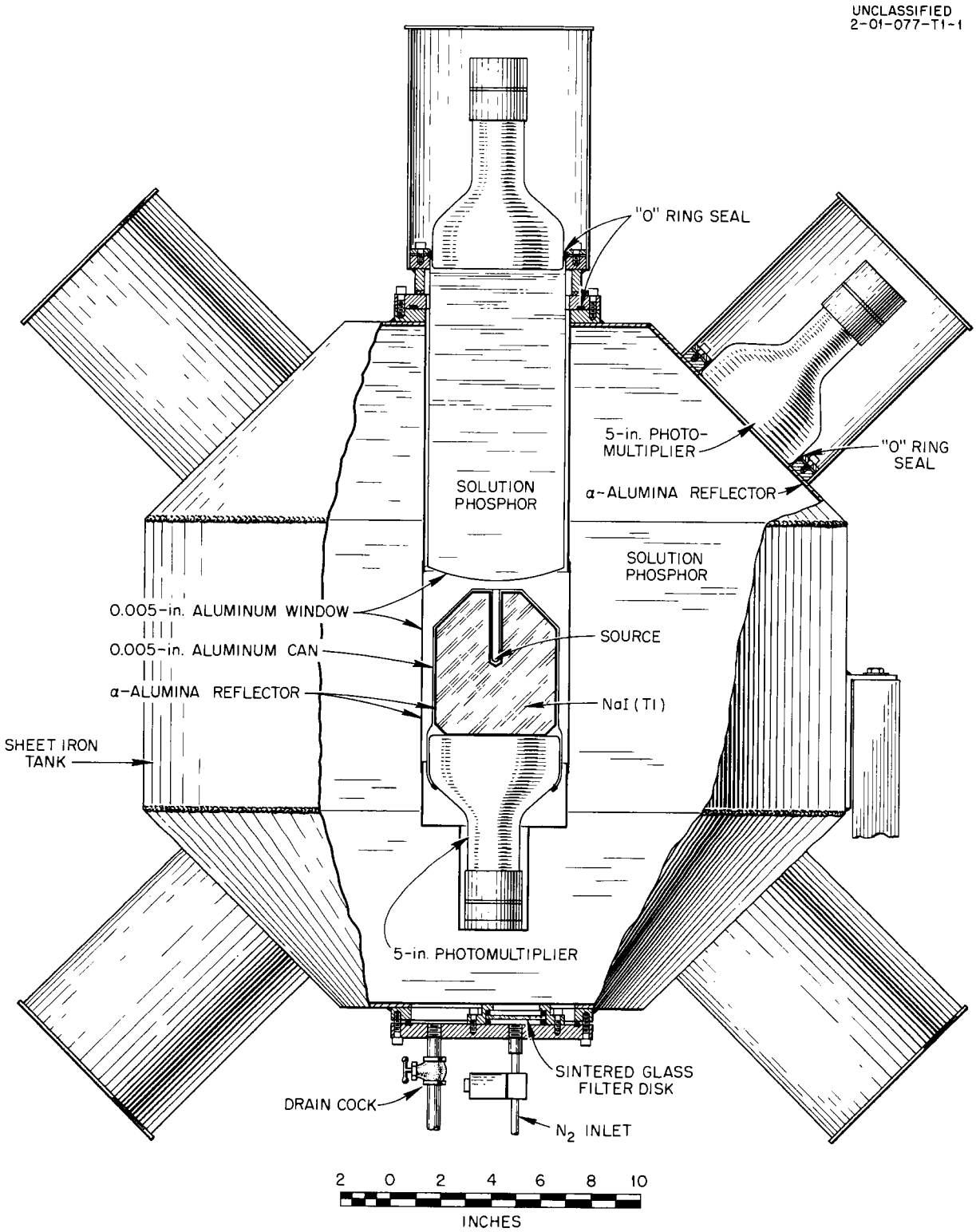

Fig. 2.1. Solution Phosphor Tank.

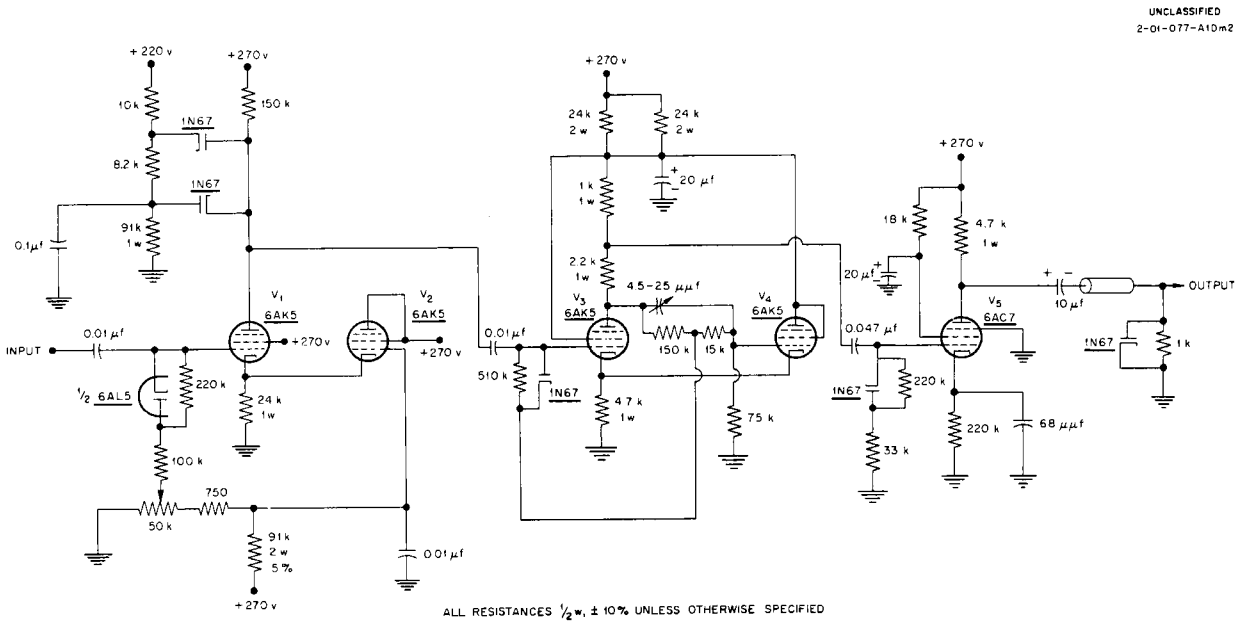

Fig. 2.2. Zero-Dead-Time Pulse-Height Selector.

passes all the current. The grid of tube V-1 is connected to the anticoincidence signal which cuts off this tube during the dead time, and causes the cathode current to flow in V-2. This current is RC filtered in the plate circuit of V-2, and the average value of the current read on a strip chart recorder. The trimmer condenser between the grid of V-1 and the common cathodes provides the charge required to change the cathode potential. This charge, being proportional to the number of pulses rather than to the pulse area, would cause an error in relative reading when the pulse width changed, if it were supplied by the cathode resistor.

The performance of the tank spectrometer is illustrated by the figures discussed in the following paragraphs.

The 1.114-Mev gamma rays of Zn^{65} give the response shown in Fig. 2.4. This is plotted on linear paper for easy comparison with magnetic-spectrometer curves. Over most of the Compton distribution the counting rate is below one-sixtieth of the peak counting rate. The peak at 300 divisions is annihilation radiation from the weak positron branch.

The source was placed at the center of the $4\frac{3}{4}$-in. crystal in a $\frac{1}{4}$-in. hole. This hole is lined with 0.005-in. aluminum foil which joins to the 0.005-in. aluminum crystal can so that the crystal is completely sealed. Thicker materials in this hole or in the crystal can or re-entrant tube are avoided due to Compton scattering from them. This scattering is already visible (beginning at 120 divisions).

Figure 2.5 shows the response to the standard source Cs^{137} (661 kev) plotted in the usual semi-log manner. The shape of the backscatter peak in this spectrometer is characteristically different from that usually found, because the scattering must come principally from the photomultiplier, the source holder, or the lining of the internal hole or from the crystal cover or re-entrant tube walls. Scattering from most of this material can reach the crystal after scattering through angles

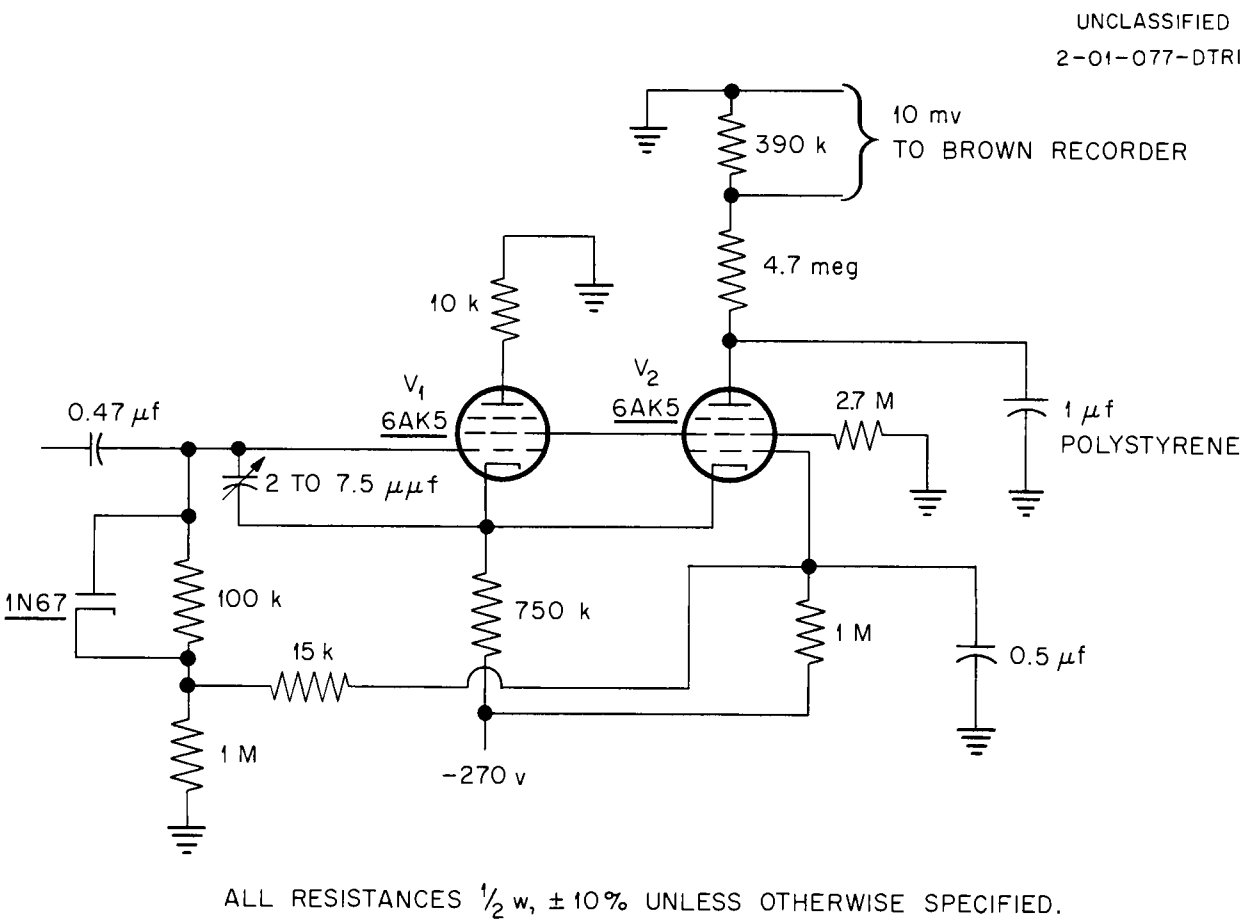

Fig. 2.3. Dead-Time Recorder.

much less than 180 deg. In the usual spectrometer most of the scattered photons must be scattered over angles near 180 deg to reach the phosphor.

The low Compton response is especially useful in the analysis of continuous spectra. Figure 2.6 is the response produced by a sample of Y^{91}. The source was covered with sufficient copper to prevent the 1.3-Mev beta rays from reaching the crystal. The upper curve is the total curve; the lower is the remainder found by subtracting the weak nuclear gamma-ray response. Without the tank, the bremsstrahlung spectrum would have become uselessly uncertain at one-half the energy of the gamma ray.

At high gamma-ray energies, where pair production is prominent, the effect of the tank in reducing the lower pair lines is spectacular. Figure 2.7 shows the response of a 3 × 3 in. NaI crystal to the gamma rays of Na^{24} (1.38 and 2.76 Mev). The radiation reached the crystal through a 3-in.-dia lead collimator and a 3½-in.-dia open re-entrant tube tunnel from outside the tank. The upper curve was without anticoincidence. The lower pair peak (420 divisions) disappears, and the upper pair peak (550 divisions) is greatly reduced.

When the same kind of source is placed against the surface of the 3 × 3 in. crystal or inside the 4¾-in. crystal, the coincident sum line at 4.14 Mev is quite strong, Fig. 2.8, and the single gamma lines are reduced. The curves may be compared with those in a previous progress report, ORNL-1620.

DECAY OF Bi^{207}

N. H. Lazar

The gamma rays following electron capture by Bi^{207} have been studied with the use of both single-crystal and coincidence NaI spectrometers. The source was prepared from the same chemically separated sample used previously by McGowan

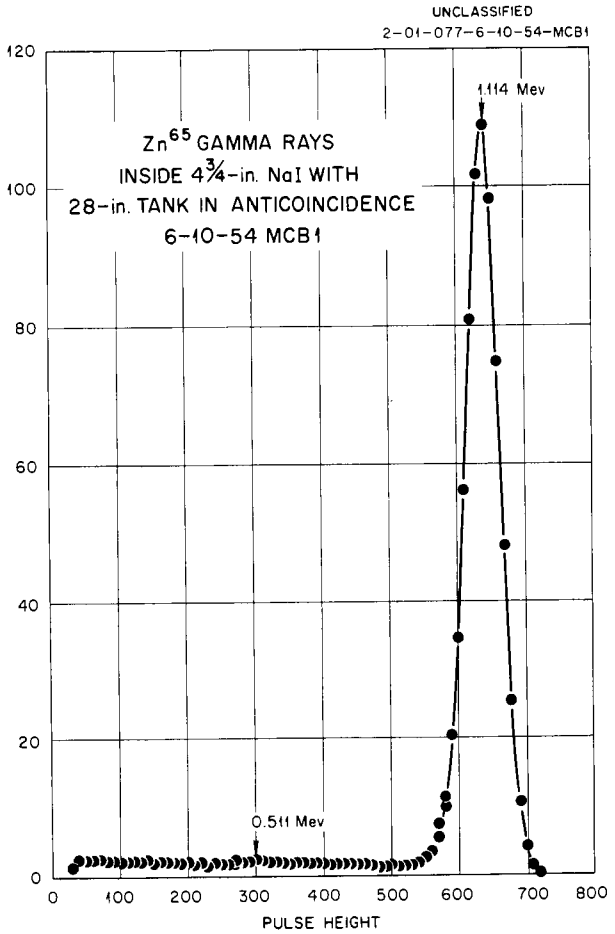

Fig. 2.4. Zn^{65} Gamma Rays Inside 4¾-in. NaI Crystal with 28-in. Tank in Anticoincidence.

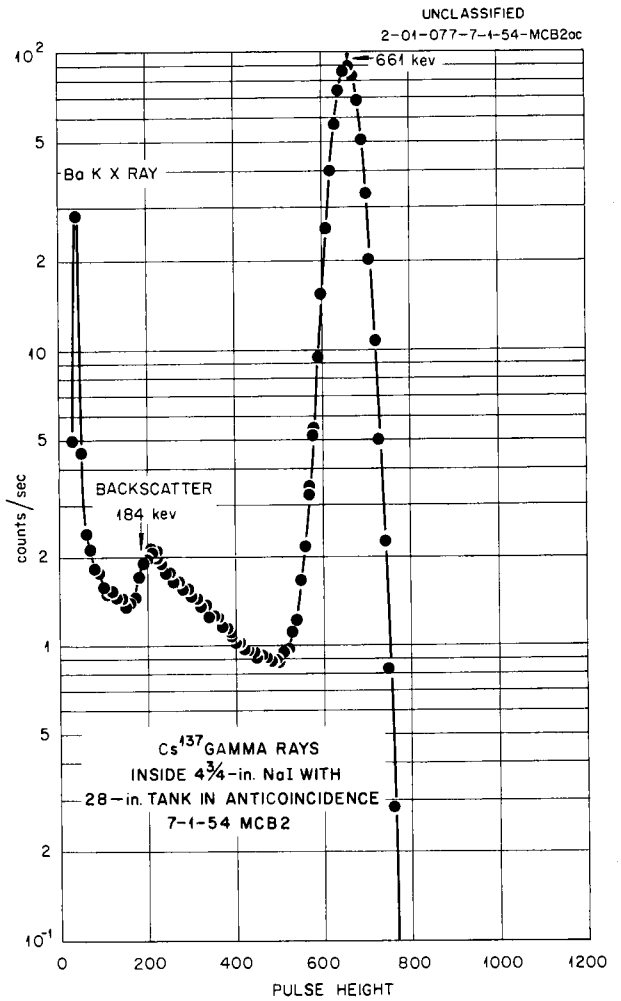

Fig. 2.5. Cs^{137} Gamma Rays Inside 4¾-in. NaI Crystal with 28-in. Tank in Anticoincidence.

and Campbell.[1] For single-crystal spectroscopy, a 3-in.-dia by 3-in.-thick NaI(Tl) crystal was used in conjunction with a multichannel analyzer.[2] The pulse-height spectrum obtained with the source 9.3 cm above the crystal is shown in Fig. 2.9. The intensity of the gamma rays may be determined from the peak areas with the use of the measured (peak-area)/(total-area) curve and the calculated total intrinsic efficiency for this crystal and geometry. After corrections were made for internal conversion of the 0.570- and 1.07-Mev gamma rays,[1] the relative intensities shown below were obtained:

Gamma-Ray Energy (Mev)	Relative Intensity
0.570	1.00
1.067	0.84 ±0.06
1.77	0.098 ±0.007

The energy calibration was made with the source in place to eliminate shifts in pulse height with counting-rate changes.

Limits may be placed on the intensities of two other gamma rays which have previously been reported[3] at 1.46 and 2.45 Mev. The region of

[1] F. K. McGowan and E. C. Campbell, *Phys. Rev.* **92**, 523 (1953).

[2] G. G. Kelley, P. R. Bell, and C. G. Goss, *Phys. Quar. Prog. Rep. Dec. 20, 1951*, ORNL-1278, p 27.

[3] J. R. Prescott, *Proc. Phys. Soc. (London)* **A67**, 540 (1954).

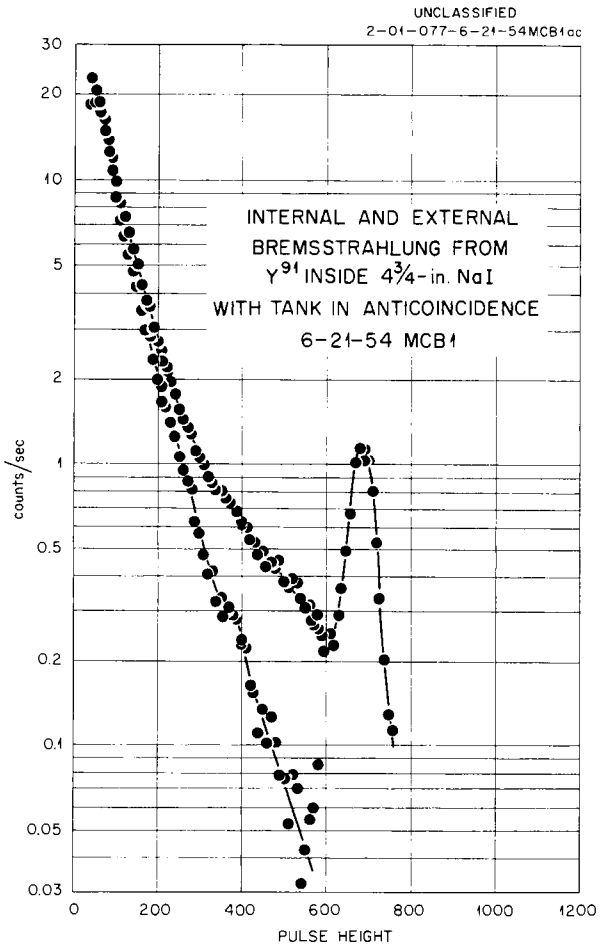

Fig. 2.6. Internal and External Bremsstrahlung from Y^{91} Inside $4\frac{3}{4}$-in. NaI Crystal with Tank in Anticoincidence.

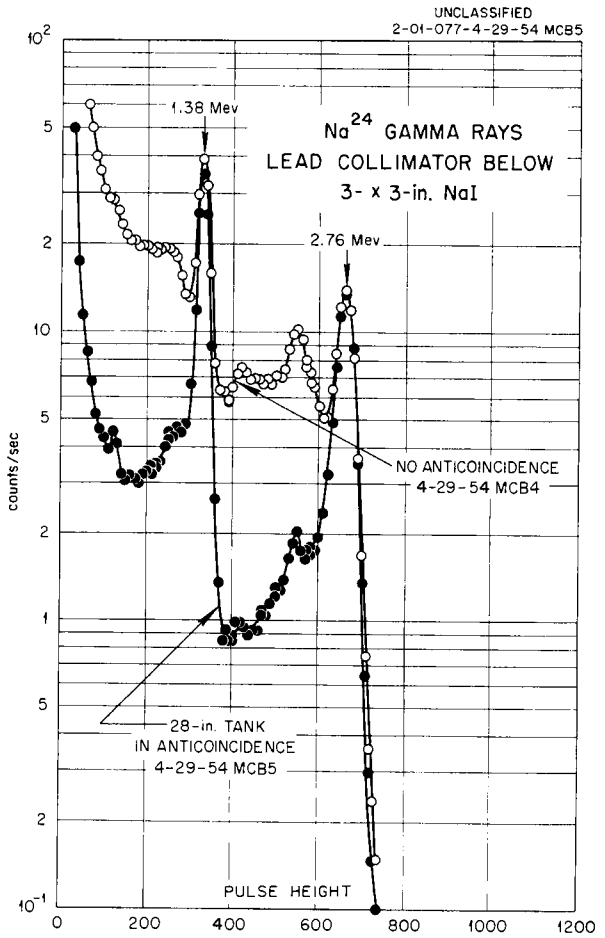

Fig. 2.7. Response of a 3 × 3 in. NaI Crystal to Na^{24} Gamma Rays.

1.5 Mev is distorted in Fig. 2.9 due to the partial absorption in the crystal of the 0.570- and 1.07-Mev gamma rays following a single transition. This effect of "coincidence summing" may be reduced by moving the source to 18.6 cm from the crystal. An upper limit of 0.25% of the intensity of the 1.77-Mev gamma ray may be placed on the 1.46-Mev gamma ray. A similar coincidence summing occurs at 2.34 Mev as a result of the complete absorption of both the 0.570- and 1.77-Mev gamma rays. The area under this peak, $N_{c.s.}$, may be calculated from

$$N_{c.s.} = \frac{N_{1.77}}{[1 - (\epsilon\Omega)_{0.570}]} (\epsilon\Omega R)_{0.570} ,$$

where

$N_{1.77}$ = area under the full energy peak due to the 1.77-Mev gamma ray,

$\epsilon_{0.570}$ = total intrinsic efficiency of the crystal for 0.570 Mev,

$R_{0.570}$ = ratio $\left(\frac{\text{peak area}}{\text{total area}}\right)_{0.570}$,

Ω = relative solid angle subtended by the crystal.

The calculated area agrees to within 10% of the observed peak. If this figure were taken as an upper limit for the intensity of a 2.34-Mev gamma ray, its intensity would be less than 0.2% of the 1.77-Mev transition. A limit of 0.1% of the intensity of the 1.77-Mev gamma ray may be placed on the reported 2.45-Mev transition.

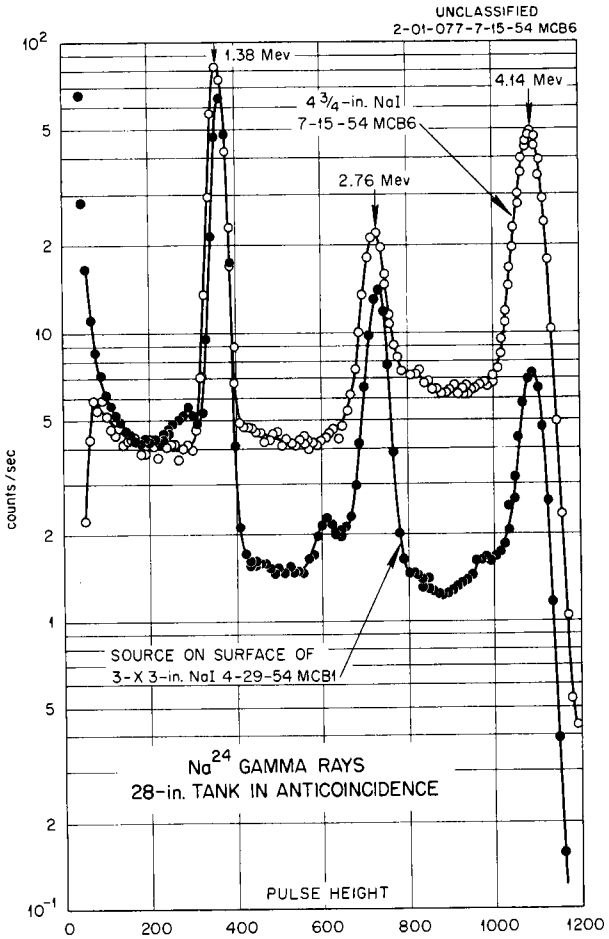

Fig. 2.8. Na^{24} Gamma Rays Inside $4\frac{3}{4}$-in. NaI Crystal and on the Surface of the 3 × 3 in. Crystal in 28-in. Tank, Corrected for Decay.

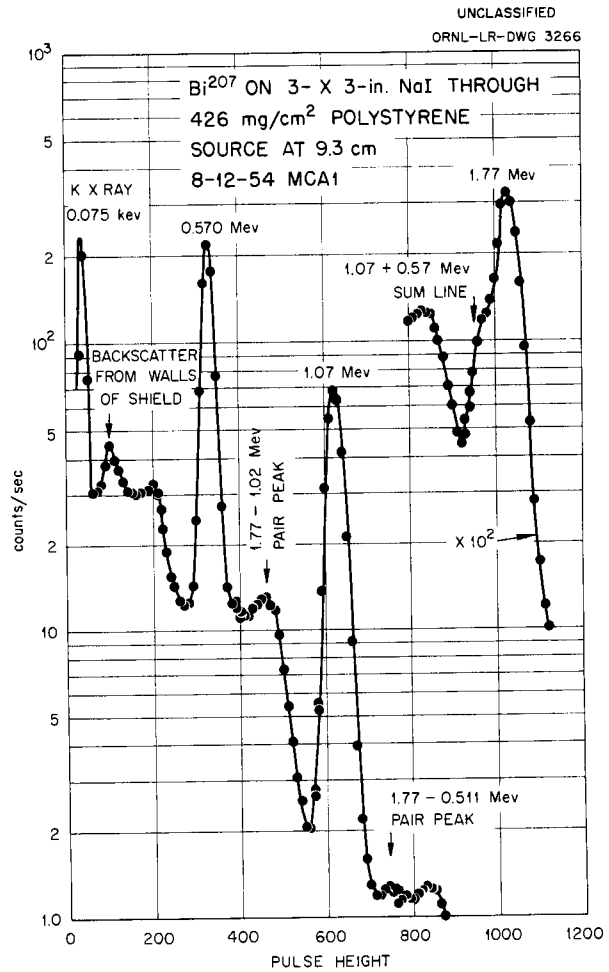

Fig. 2.9. Pulse-Height Spectrum of Gamma Rays from Bi^{207}.

Coincidence spectra were obtained with the use of two 3 × 3 in. NaI crystals with a multichannel analyzer in one channel and a single-channel analyzer in the second channel.[4] The "singles" spectrum obtained with the single-channel analyzer is shown in Fig. 2.10 with the various positions of the window indicated. With the window set on the peak of the x ray, coincidences were observed with the 0.570-, 1.07-, and 1.77-Mev gamma rays (Fig. 2.11). One may measure the expected area under the full energy peak of the 1.07-Mev gamma ray due to coincidences with Compton electron pulses in the window from the others by shifting the window just off the x-ray peak (*b* in Fig. 2.10) and by measuring the coincidence spectrum. In addition, one may calculate the number of coincidences with *K* x rays, following internal conversion of the 0.570-Mev gamma ray, which is expected to fall in the coincidence peak of the 1.07-Mev gamma ray from

$$N_{1.07} = \frac{N_{0.570}}{(\epsilon\Omega R)_{0.570}} \alpha^{k}_{0.570} \times f_{pb} F(\epsilon\Omega R)_{1.07} \frac{1}{1+\alpha_{1.07}} q \frac{1.07}{0.570} ,$$

where

$N_{0.570}$ = measured "singles" full-energy-peak area from the 0.570-Mev gamma ray,

[4] J. E. Francis and P. R. Bell, *Precision Single-Channel Analyzer; Model No. 5-Q-1192*, ORNL-1470 (Feb. 10, 1953).

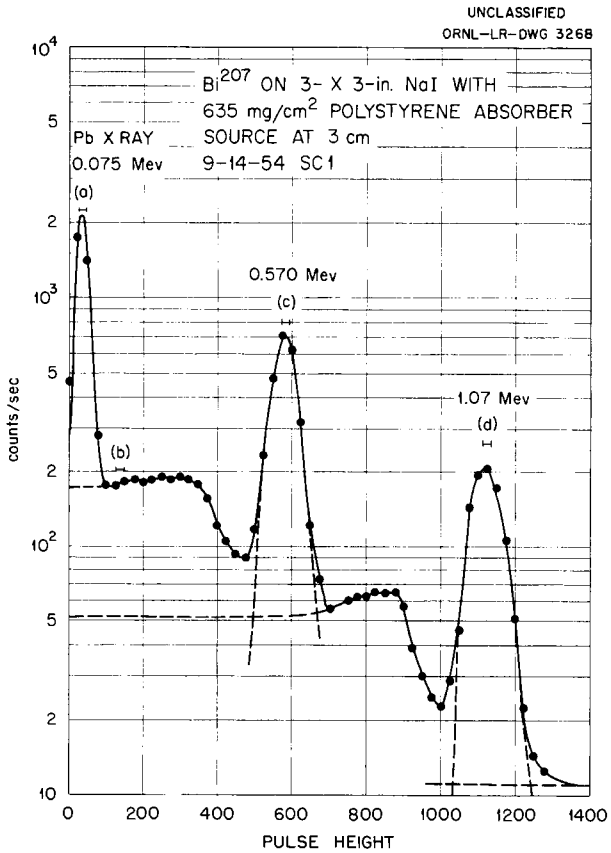

Fig. 2.10. "Singles" Spectrum of Gamma Rays from Bi^{207} Using Single-Channel Analyzer. (a), (b), (c), and (d) indicate the position of the window in various coincidence runs.

$\alpha^k_{0.570}$ = k conversion coefficient of the 0.570-Mev gamma ray and was measured[1] to be 0.017,

f_{pb} = fluorescent yield from the K shell in lead, taken as 0.95,

$\alpha_{1.07}$ = total internal conversion coefficient of the 1.07-Mev gamma ray, taken as 0.10,

$q\frac{1.07}{0.570}$ = fraction of 1.07-Mev transitions per 0.570-Mev transition,

F = fraction of the K x rays emitted which are observed in the window and can be calculated from

$$F = \frac{C_x}{(\epsilon\Omega R)_x e^{-\lambda l}} \frac{N_x}{},$$

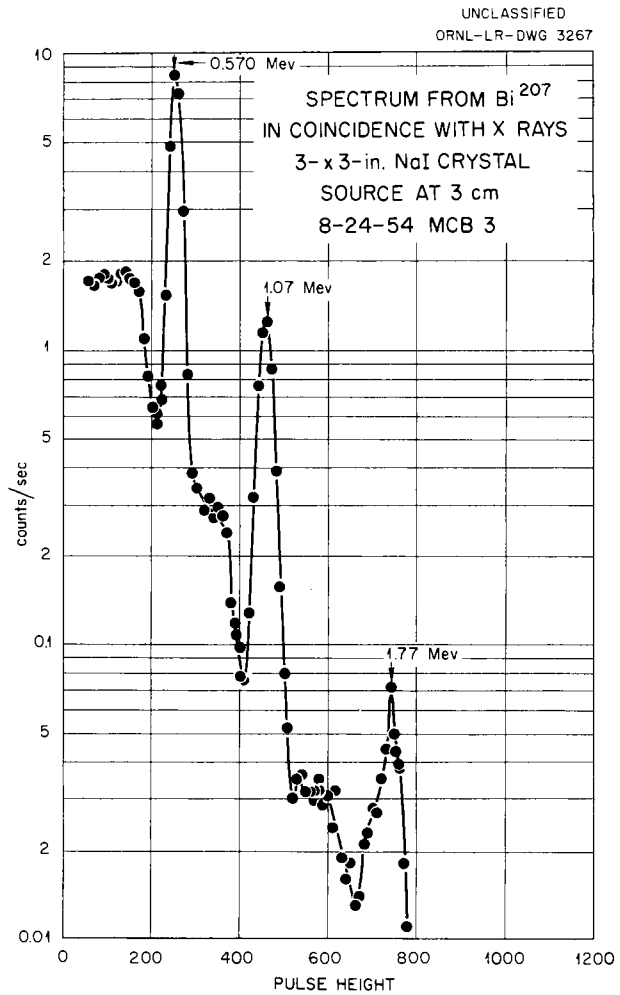

Fig. 2.11. Spectrum Observed in Multichannel in Coincidence with Window at (a) in Fig. 2.10.

in which

C_x = x-ray "singles" counting rate in the window,

N_x = "singles" peak area,

ϵ_x = 1,

R_x = ratio $\left(\frac{\text{peak area}}{\text{total area}}\right)_{x\ \text{ray}}$ and is different from unity due to the escape of the iodine x rays from the crystal; R was taken[5] as 0.925,

$e^{-\lambda l}$ = fraction of the x rays absorbed in the 635 mg/cm^2 polystyrene used to remove the conversion electrons from the 1.07-Mev gamma ray.

[5] F. K. McGowan, *Phys. Rev.* 93, 163 (1954).

The calculated peak area, $N_{1.07}$, was 4.47 counts/sec. The observed area was 4.19 counts/sec after the random rate was subtracted. One may conclude from these data that the state at 1.64 Mev is delayed following the electron capture, in agreement with the measured half life[6] for this state of 0.84 sec and in disagreement with the recent results of Prescott.[3] Similar calculations show no K x-ray–1.77-Mev gamma-ray coincidences which are not accounted for in the same way. The transition to the 2.34-Mev state is therefore presumed to occur through L-electron capture only, which fixes the ground state of Bi^{207} at less than 70 kev above this state. The expected area under the 0.570-Mev peak was also determined in a similar way, and the number of transitions directly to this level was obtained from the difference between expected and observed areas. On this basis, 3.6% of the transitions feed this level directly. The peak areas obtained in coincidence with windows set on the 0.570- and 1.07-Mev peaks (c and d in Fig. 2.10) agreed with the calculated intensities to within 7%.

A decay scheme may now be constructed (Fig. 2.12) which will be consistent with all the above information. The spin assignment of the 2.34-Mev level is still uncertain despite the angular-correlation experiment performed by E. D. Klema (*cf.* "Angular Correlation of Gamma Rays," this report).

[6] E. C. Campbell and M. Goodrich, *Phys. Rev.* **78**, 640 (1950); E. C. Campbell and F. Nelson, *Phys. Rev.* **91**, 499 (1953).

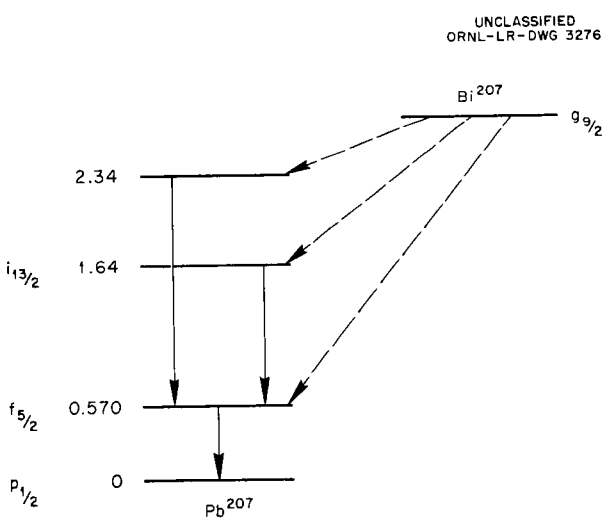

Fig. 2.12. Proposed Decay Scheme of Bi^{207}.

The data are subject to two possible interpretations consistent with 7/2→5/2→1/2 or 9/2→5/2→1/2 for the 1.77–0.570-Mev cascade.

DECAY OF Sb^{124}

N. H. Lazar

The gamma radiation following the beta decay of Sb^{124} has been studied with a 3 × 3 in. NaI(Tl) scintillation spectrometer. The pulse-height spectrum obtained is shown in Fig. 2.13. For purposes of subtraction, the Compton distributions for the gamma rays at 2.11, 1.71, and 1.38 Mev were constructed from gamma radiation from Pr^{144} (2.18 Mev), Y^{88} (1.85 Mev), and Na^{24} (1.38 Mev). Relative areas of the gamma rays are given in the following tabulation and were determined from the

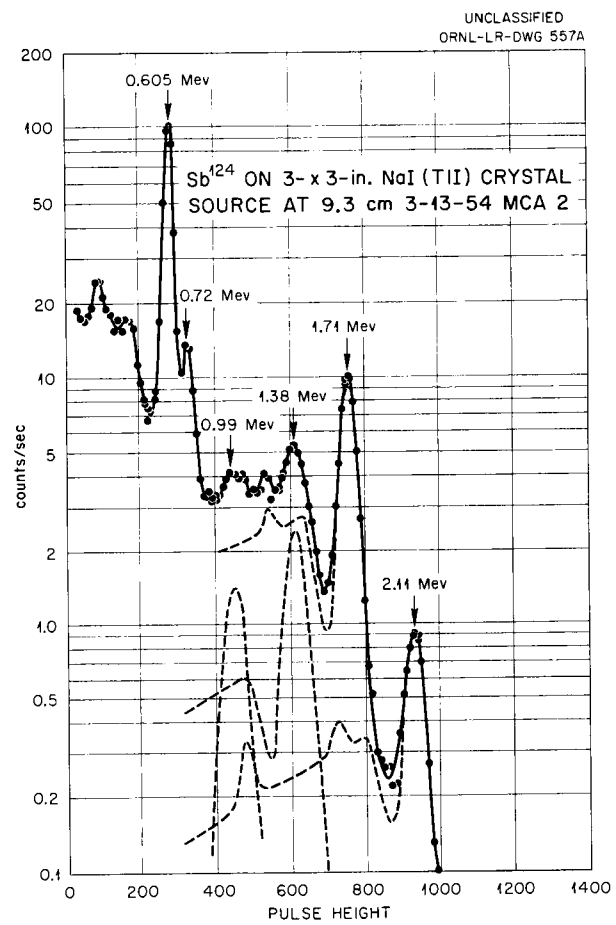

Fig. 2.13. Pulse-Height Spectrum from Gamma Rays of Sb^{124}; Sb^{124} on 3 × 3 in. NaI(Tl) Crystal Source at 9.3 cm.

peak areas and measured peak-to-total efficiency data for this crystal and geometry.

Gamma-Ray Energy (Mev)	Relative Intensity
0.603	1.00
0.99	0.054
1.38	0.062
1.71	0.457
2.11	0.099

From the intensities and energies of the gamma rays and from the previously reported beta-ray analysis,[7] a consistent decay scheme may be constructed (Fig. 2.14). The ratio of the sums of intensities of the gamma radiation leaving the levels at 2.7 and 2.3 Mev above the ground state was determined as 0.32. From the previous beta-ray analysis, the ratio of intensities of beta rays feeding this level is 0.29. The energy of the 1.38- and 0.99-Mev gamma rays fixes the energy of the second excited state. The gamma rays at 0.99 and 1.38 Mev are exceedingly difficult to observe with smaller NaI crystals because of the relatively smaller peak intensity of these gamma rays in such detectors and the unfortunate coincidence, energy-wise, with expected effects due to other gamma rays.

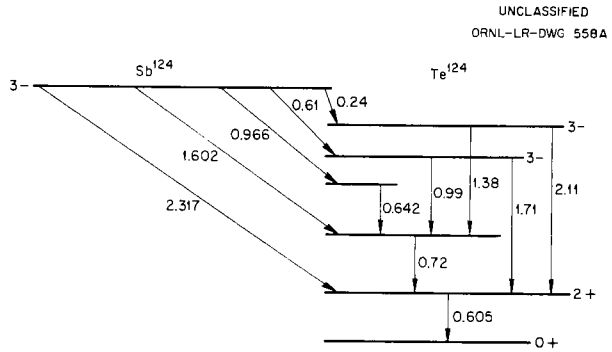

Fig. 2.14. Proposed Decay Scheme for Sb^{124}.

RESPONSE OF LITHIUM IODIDE (EUROPIUM) PHOSPHOR

J. H. Neiler F. J. Muckenthaler
J. Schenck W. E. Kunz
W. M. Good

Thermal-neutron responses have been obtained for lithium iodide crystals grown from melts with europium activator concentrations as high as 0.25 mole %. The gamma-ray equivalent for this concentration was 5.13 Mev; however, the resolution was of the order of 15 to 20% on the thermal peak, probably as a result of excessive light absorption in the crystal. This concentration appears to be near the maximum of the equivalent pulse-height vs concentration curve.

Pulse-height spectra have been obtained with a 25 × 10 mm crystal having a nominal europium concentration of 0.1% for incident-neutron energies of 2.18, 3.64, 5.07, and 16.7 Mev (Figs. 2.15 to

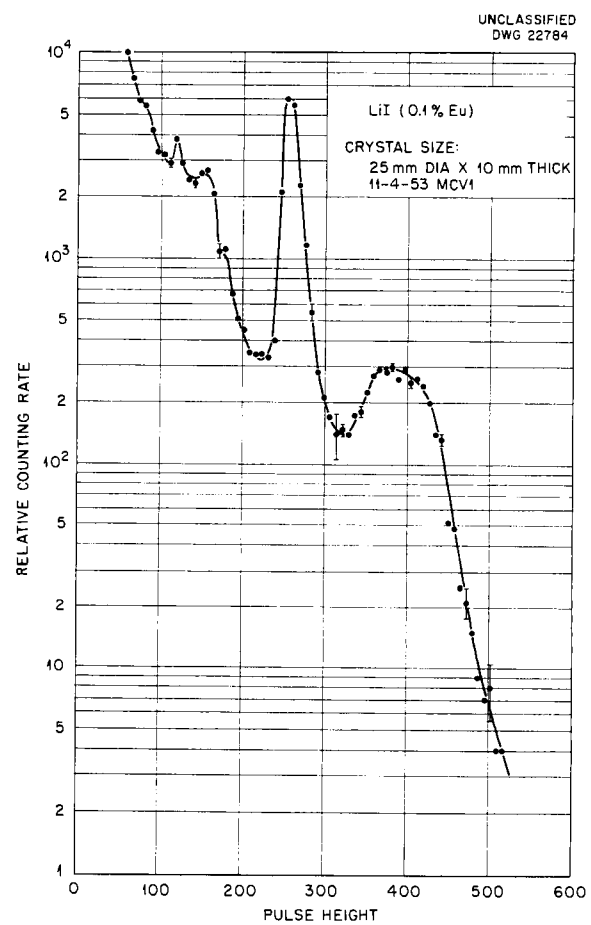

Fig. 2.15. Pulse-Height Spectrum Obtained with a 25 × 10 mm Crystal (Nominal Europium Concentration, 0.1%) for Incident-Neutron Energy of 2.18 Mev.

[7] L. M. Langer, N. H. Lazar, and R. J. D. Moffat, *Phys. Rev.* 91, 338 (1953).

2.18). A gamma-ray calibration is provided by the response to a Po-Be neutron source, which is also plotted on Fig. 2.17. The peak at 200 pulse-height units corresponds to an energy of 3.43 Mev left in the crystal when a 4.44-Mev gamma ray from C^{12*} in the source is absorbed by a pair-production event and both annihilation quanta escape from the crystal. The peaks at 260 pulse-height units in Figs. 2.15 to 2.17 and at 115 units in Fig. 2.18 are due to thermal neutrons.

The upper and lower edges of the broad peaks produced by the fast neutrons have been fitted by error integral functions corresponding to the appropriate resolution. The pulse-height spacing between the half-intensity points of these error integral functions is plotted vs the energy released in the crystal in Fig. 2.19. The solid line represents the response of the crystal to gamma rays, based on calibrations obtained with Zn^{65} and the 3.43-Mev peak from C^{12*}.

The broadness of the peaks is explainable in terms of the range of energies available to the α and triton from the fast-neutron-induced $Li^6(n,\alpha)T$ reaction and the nonlinearity of pulse height with heavy-particle energy, which is characteristic of known scintillators. It is surprising that for the heavy particles from the Li^6 reaction the pulse height per Mev is in some cases greater than it is for gamma rays. Some rough checks have indicated that for alphas of 3 to 5 Mev the pulse height per Mev is about 50 to 60% of that for gamma rays; thus it appears that unusual response must be attributed to the triton.

This unusual behavior may perhaps be explained by the large amount of overlap of the absorption and emission spectra of europium-activated lithium

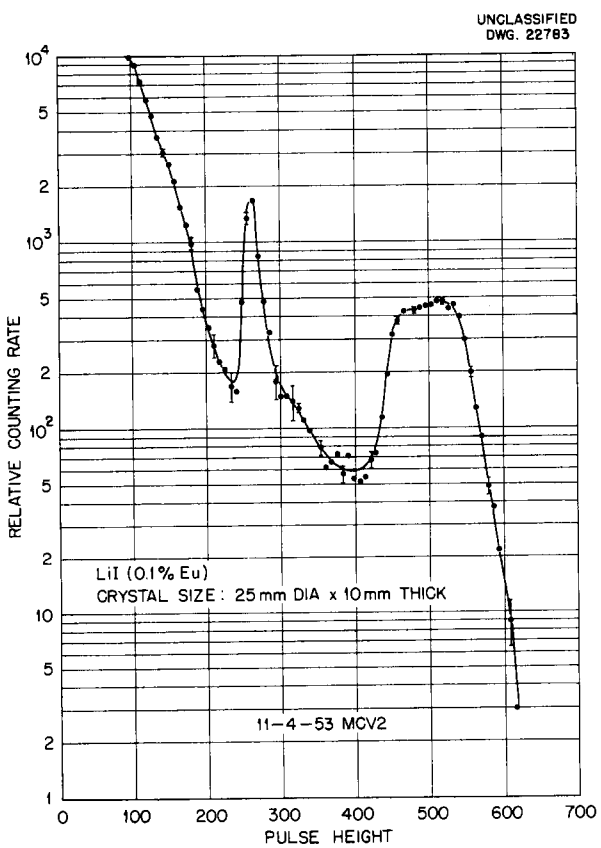

Fig. 2.16. Pulse-Height Spectrum Obtained with a 25 × 10 mm Crystal (Nominal Europium Concentration, 0.1%) for Incident-Neutron Energy of 3.64 Mev.

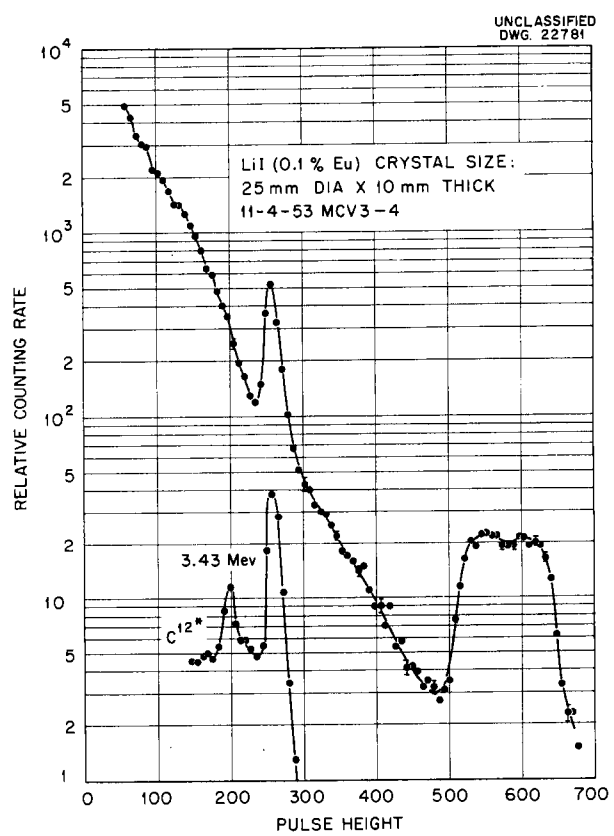

Fig. 2.17. Pulse-Height Spectrum Obtained with a 25 × 10 mm Crystal (Nominal Europium Concentration, 0.1%) for Incident-Neutron Energy of 5.07 Mev.

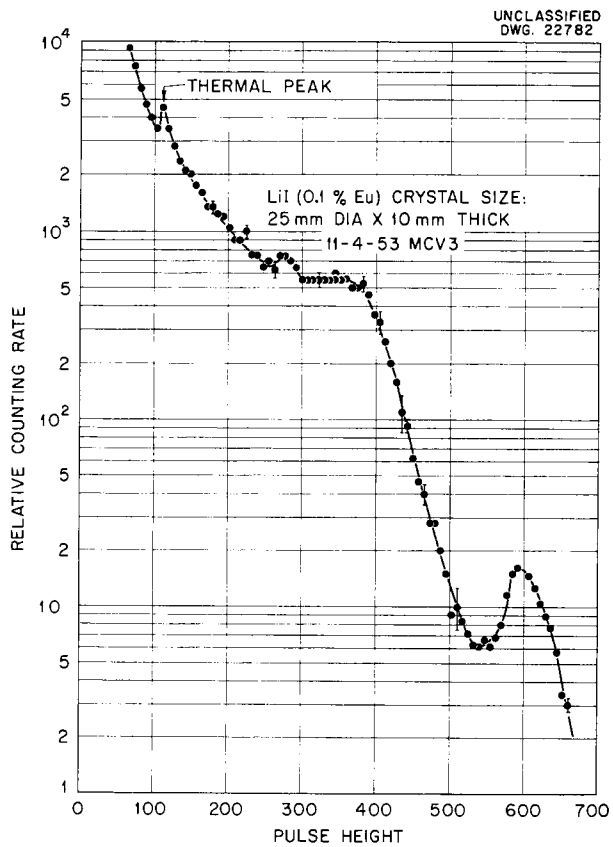

Fig. 2.18. Pulse-Height Spectrum Obtained with a 25 × 10 mm Crystal (Nominal Europium Concentration, 0.1%) for Incident-Neutron Energy of 16.7 Mev.

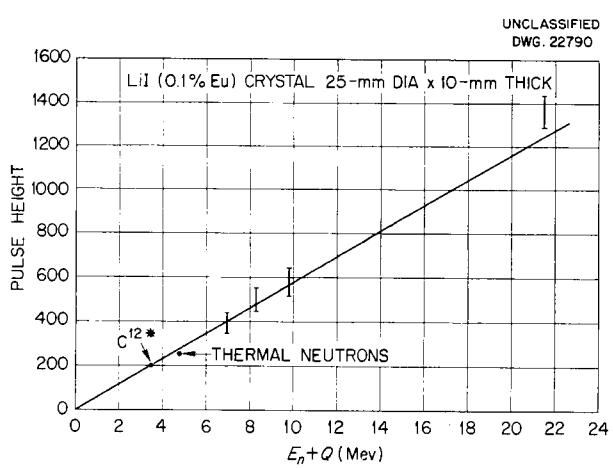

Fig. 2.19. Pulse-Height Spacing Between Half-Intensity Points of Error Integral Functions vs Energy Released in Crystal.

iodide.[8] The ionization density of the triton track may produce a perturbation of the energy levels of the emitting centers which is just sufficient to shift the emission spectrum toward longer wavelengths and out from under the absorption edge somewhat, without greatly increasing the probability of nonradiative transitions. The result would be that in thick crystals, such as were used here, the technical light output per Mev would be greater for the triton than for gamma rays, for which the probability is greater for the emitted photons to fall within the absorption band. The heavier ionization density of the alphas apparently must perturb the energy levels of the emitting levels so that the radiationless-transition probabilities become quite high and the pulse height per Mev is reduced.

A quick experiment with a thin (~ ½-mm) crystal (0.1 mole % europium) with the use of protons, tritons, and alphas from deuterons on Be^9 has provided additional evidence in favor of this theory. The pulse height per Mev for all the heavy particles was less than that for gamma rays.

A COMPARISON OF LARGE-SINGLE-CRYSTAL AND MULTIPLE-CRYSTAL GAMMA-RAY SPECTROMETERS

F. C. Maienschein R. W. Peelle
T. A. Love

An attempt has been made to determine whether a large single NaI(Tl) crystal would be useful as a gamma-ray energy spectrometer for applications involving gamma-ray sources having continuous distributions in both space and energy. The results obtained with several possible arrangements in which such a crystal was used have been compared to results obtained with the multiple-crystal spectrometer, with respect to the degree of uniqueness of response. For all measurements a lead shield was used to reduce background. Such a lead shield would, in practical applications, be required for collimation of a spatially distributed source.

As a test of the performance of the different types of spectrometers, the peak-to-total ratios were determined for several sources of monoenergetic gamma rays. The peak-to-total ratio is the fraction of the total area under the pulse-

[8] J. Schenck, *Phys. Semiann. Prog. Rep. Sept. 10, 1953*, ORNL-1620, p 62.

TABLE 2.1. ENERGY RESOLUTION (PEAK-TO-TOTAL RATIOS) OF GAMMA-RAY SCINTILLATION SPECTROMETERS USING NaI(Tl) CRYSTALS

Spectrometer							Peak-to-Total Ratio			
							Source			
Type	Number of Crystals	Size of Crystals	Size of Well in Crystal	Source Geometry	Photomultiplier	Distance from Nearest Lead Wall (in.)	Hg^{203}, 0.279 Mev	Cs^{137}, 0.663 Mev	Zn^{65}, 1.118 Mev	Na^{24}, 2.76 Mev
Large crystal	1	4-in. dia by 4 in.	1-in. dia by 1 in.	Inside well	DuMont K-1198	$2\frac{1}{2}$	0.87	0.59	0.42	
Large crystal	1	4-in. dia by 4 in.	1-in. dia by 1 in.	Collimated into well	DuMont K-1198	$2\frac{1}{2}$	0.92	0.67[a]	0.38[a]	
Large crystal	1	4-in. dia by 4 in.	None	Uncollimated[b] next to crystal	DuMont K-1198	$2\frac{1}{2}$	0.60	0.37	0.31	
Compton	2	1-in. dia by 1 in.; $1\frac{1}{2}$-in. dia by $1\frac{1}{2}$ in.		Collimated onto initial crystal	DuMont 6292	~1	0.84	0.74	0.69	~0.36
Pair	3	1-in. dia by 1 in.; $1\frac{1}{2}$-in. dia by $1\frac{1}{2}$ in.		Collimated onto initial crystal	DuMont 6292	~1				0.88

[a]Results with a collimated source of radiation directed upon a crystal with no well gave essentially the same results.

[b]Little change in the peak-to-total ratio was observed when the distance between source and crystal was increased to a very large value (~4 ft).

height distribution curve which is contained in the peak corresponding to the gamma-ray energy. Typical pulse-height curves which were obtained with a Cs^{137} source (0.663 Mev) are shown in Fig. 2.20. A summary of the peak-to-total ratios obtained with four sources and five types of gamma-ray spectrometers is presented in Table 2.1. The first columns of this table describe the gamma-ray spectrometers which were tested.

The results of Table 2.1 appear to show that the peak-to-total ratio for the 4-in. crystal becomes so low above approximately 1 Mev that the interpretation of results obtained with a continuous spectrum would be very difficult. The multiple-crystal spectrometer would, of course, give usable results with an extended source of continuous energy spectrum if sufficient source intensity were available.

The proximity of the lead shield in the above experiments tends to lower the observed peak-to-total ratios. This effect should be considered when comparing these results with other data taken under conditions not requiring a lead shield. Further, the Compton and pair spectrometers utilized poor geometry in order to attain high sensitivity. With good geometry (and the resulting lower sensitivity) for a Compton spectrometer and a Zn^{65} source, Kreger[9] has reported a peak-to-total ratio of 80%.

NUCLEAR ISOMERS OF SHORT HALF LIFE

E. C. Campbell R. W. Peelle
F. C. Maienschein

New measurements are reported on the gamma energies and half lives of rapidly decaying nuclear isomers produced by short neutron bombardment in the fast pneumatic tube installed in the ORNL Graphite Reactor. A scintillation spectrometer

[9] W. E. Kreger, private communication.

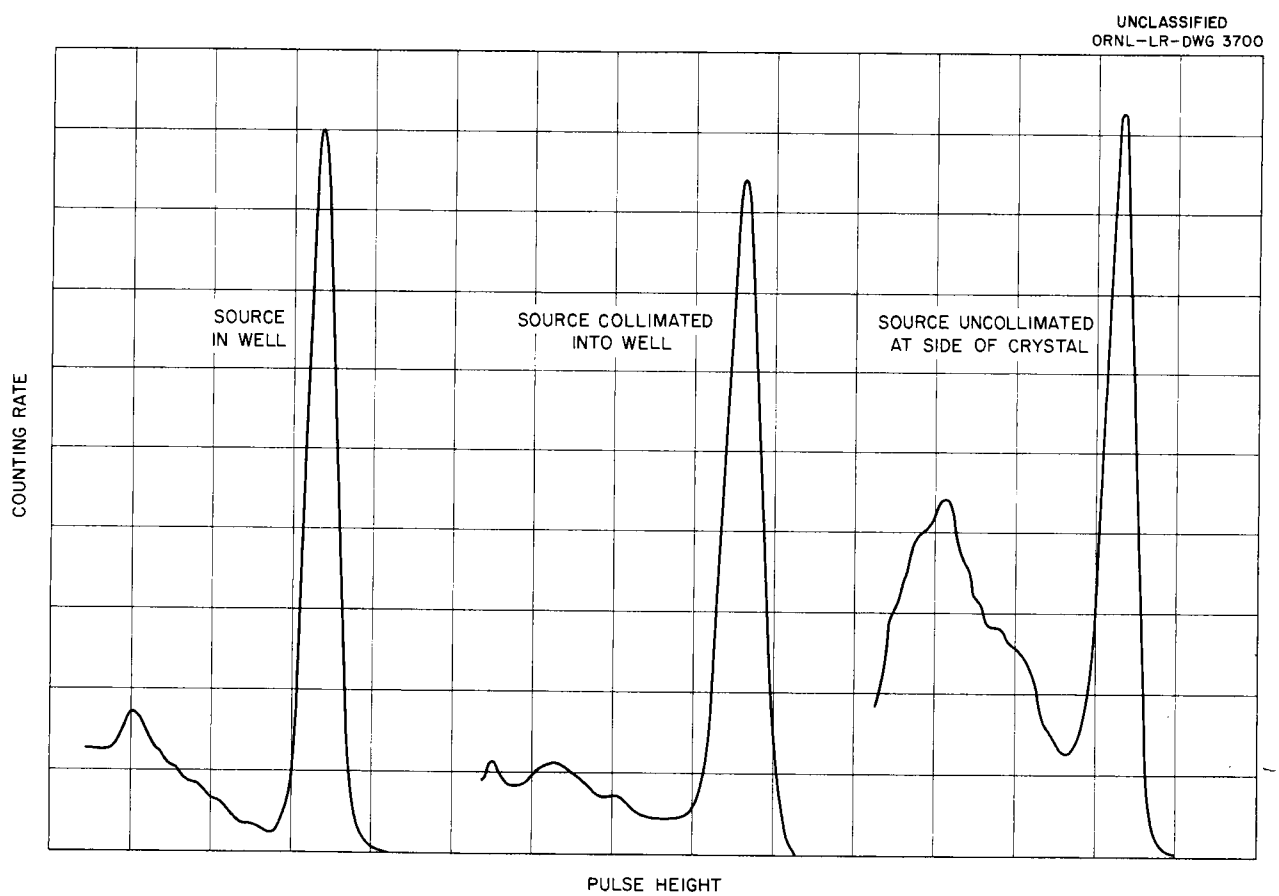

Fig. 2.20. Pulse-Height Curves Obtained with an NaI(Tl) Crystal (4 in. dia. by 4 in.) and a Cs^{137} Source.

with a 40-channel pulse-amplitude analyzer was used for the gamma-energy measurement. Substantial improvement in the half-life measurement resulted from the use of a single-channel analyzer, the window of which was set to pass only those pulses associated with the desired gamma ray. Four isomers not previously reported have been found in germanium, cadmium, and iridium, and new measurements are given for isomers produced by neutron bombardment of zirconium, germanium, ytterbium, and lead. By irradiation of separated isotopes of zirconium and germanium, identification was made of the target nucleus responsible for isomer production in these elements. All the isomers discussed have half lives between 0.05 and 5 sec.

Apparatus

The NaI scintillation spectrometer installed at the fast pneumatic tube of the ORNL Graphite Reactor is designed to detect and measure gamma radiation emitted by substances which have been exposed to the neutrons in the reactor. The irradiated sample contained in a nylon sample carrier may be ejected from the reactor into the spectrometer housing so that the total elapsed time from reactor to spectrometer is of the order of 0.1 sec. Recently, arrangements were completed to send the pulses from the spectrometer through coaxial cable to a 40-channel analyzer located several hundred feet away in another building. A special preamplifier was designed for this purpose. Constant communication between the two stations is provided by a standard intercommunication system.

In addition, an electronic timer,[10] designed by F. M. Glass of the Instrument Department, has been installed. The timer consists of a precision master oscillator and three scalers which control in succession the exposure time of the sample in the reactor, the waiting time, and the counting time of the multichannel analyzer. It has been found that with this timer the number of counts accumulated in successive runs of a short-lived sample is reproduced within statistics. Moreover, the background pulse-height spectrum associated with the activation of the nylon sample carrier is easily obtained in blank runs with the same timing sequence. This background, although small, is not usually negligible.

Half-life measurements were made with the aid of a single-channel pulse-height analyzer. The window of this analyzer is adjusted to correspond to the pulse-height interval associated with the gamma-ray peak of a sample as measured previously with the multichannel analyzer. The output of the single-channel analyzer is fed to a fast scaler, whose output is recorded on a fast-moving paper strip by the pen galvanometer of a Brush recorder. Using the single-channel analyzer has the effect in most cases of reducing the background considerably, as compared with the desired short-period decay.

Considerable difficulty was experienced in pulse-height spectrum measurements of two isomers having extremely short half lives (less than 0.1 sec) due to the limitation (10^4 counts/sec) on the maximum integral counting rate of the multichannel analyzer. Here the counting rate of the sample was changing so rapidly that the number of significant counts in the pulse-height specfrum accumulated in a single exposure was small, due to the fact that the time interval between ceiling (maximum permissible analyzer counting rate) and floor (background counting rate) was so short. As a result, (1) a large number of runs had to be made with a small sample rather than (2) a few runs with a larger sample in order to obtain a pulse-height spectrum. It is evident, then, that the background constitutes a greater fraction of the total accumulated count in the spectrum in case 1 than in case 2, and therefore a higher permissible counting rate is not merely a convenience but a necessity if the spectra of very rapidly decaying species are to be investigated with some precision.

Results

The results of the present study are shown in Table 2.2.

Discussion

The isomer in iridium found to decay with a 4.4-sec half life is probably to be identified with that found in the decay of Os^{191} by rapid chemical separation[11] of iridium from osmium. The half life

[10] F. M. Glass, *Instrumentation and Controls Semiann. Prog. Rep. July 31, 1954*, ORNL-1768, p 19.

[11] F. T. Howard and W. H Sullivan, *Oak Ridge National Laboratory Status and Progress Report for April 1954*, ORNL-1719, p 21 (cf. "Separation of Ge^{73m} from As^{73} and of Ir^{191m} from Os^{191}," this report).

TABLE 2.2. CHARACTERISTICS OF NUCLEAR ISOMERS WITH HALF LIVES IN THE REGION OF 1 sec

Bombarded Element or Isotope	Half Life (sec)	Gamma Energy (Mev)	Isomer Assignment	Reaction
Ir	4.4 ± 0.5	0.127	Ir^{191m}	$Ir^{191}(n,n)Ir^{191m}$
Ir	0.05 ± 0.01	0.065	?	?
Cd	2.40 ± 0.1	0.16	?	?
Ge^{73}	2.30 ± 0.1	0.16	?	?
Zr^{90}	0.83 ± 0.03	2.30	?	Zr^{90}(fast n)
Ge^{72}	0.53 ± 0.03	0.054	Ge^{73m}	$Ge^{72}(n,\gamma)Ge^{73m}$
Yb	0.08 ± 0.01	0.51	?	?
Pb^{207}	0.84 ± 0.02	0.57 1.06	Pb^{207m}	$Pb^{207}(n,n)Pb^{207m}$

derived from that experiment (4.9 sec) is probably a better value, since the neutron-irradiated sample had in it a large background due to Ir^{192m} (1.5 min).

The 0.05-sec isomer in iridium decays with a 65-kev radiation, which might be identified with the K x ray of iridium (64.9 kev). The isomer in ytterbium was previously reported[12] to have a somewhat longer half life. The present measurements are thought to be more reliable since the large background associated with the 6.6-sec isomer in ytterbium is largely eliminated in the present experiment. As far as is known, these isomers are the first to be found in the half-life interval between 0.01 and 0.10 sec.

The identification of the 0.53-sec isomer as Ge^{73m} is based on chemical evidence, since a short-period activity was found[13] in the decay of As^{73}. The gamma energy (54 kev) agrees with that (53.9 kev) found in the As^{73} decay. The present half-life measurement is derived from a decay curve which is followed over a factor of 100. The previous measurement of 0.35 sec was based on a decay curve of unseparated germanium to which the isomers Ge^{75m} and Ge^{77m} (both about 50-sec half life) gave a large background and in which the decay could be followed over only a factor of 3. The 0.53-sec isomer is also found in the neutron irradiation of our Ge^{73} sample. It is not known whether it is produced also by the $Ge^{73}(n,n)Ge^{73m}$ reaction or whether the observed yield is associated with the activation of the small amount of Ge^{72} (11.8%) in the sample enriched to 68.9% in Ge^{73}.

The additional 2.30-sec isomer in germanium is somewhat surprising, and one would be tempted to attribute it to an impurity. However, a spectrographic analysis of the enriched Ge^{73} sample reveals no impurity which could possibly be responsible for this new activity.

Still more surprising is the high energy (2.30 Mev) associated with the short-period isomer in zirconium. Irradiation of the separated isotopes of zirconium showed that this activity was unequivocally associated with Zr^{90} as the target nucleus. Exposure of the sample with and without a cadmium cover showed that the cadmium had very little effect, comparable to what was observed in a similar experiment with the lead isomer Pb^{207m}, known to be produced by fast neutrons (threshold 1.64 Mev) inelastically scattered from Pb^{207}. The conclusion is that thermal neutrons are not responsible for the activation. It appears likely that this isomer is associated with the closed 50-neutron shell. It is proposed to continue

[12] J. H. Kahn, *An Investigation of X-Ray and Gamma Ray Spectra of Short Period Radioisotopes*, ORNL-1089 (Nov. 8, 1951); E. C. Campbell, *Phys. Quar. Prog. Rep. June 20, 1952*, ORNL-1365, p 10.

[13] W. H Sullivan and F. T. Howard, *Oak Ridge National Laboratory Status and Progress Report for April 1953*, ORNL-1545, p 17 (cf. "Separation of Ge^{73m} from As^{73} and of Ir^{191m} from Os^{191}," this report).

the study of this isomer by measuring the activation cross section as a function of neutron energy, thus distinguishing between the various possibilities.

In Fig. 2.21 is shown the NaI pulse-height spectrum of Pb^{207m} taken with the multichannel analyzer. The energies of the two gamma rays are 0.57 and 1.06 Mev. The total recording time for this spectrum was 58 sec. Figure 2.22 shows the decay curve of the 0.53-sec isomer Ge^{73m} taken with the single-channel analyzer set to pass 54-kev pulses.

[14]ORNL Chemistry Division.

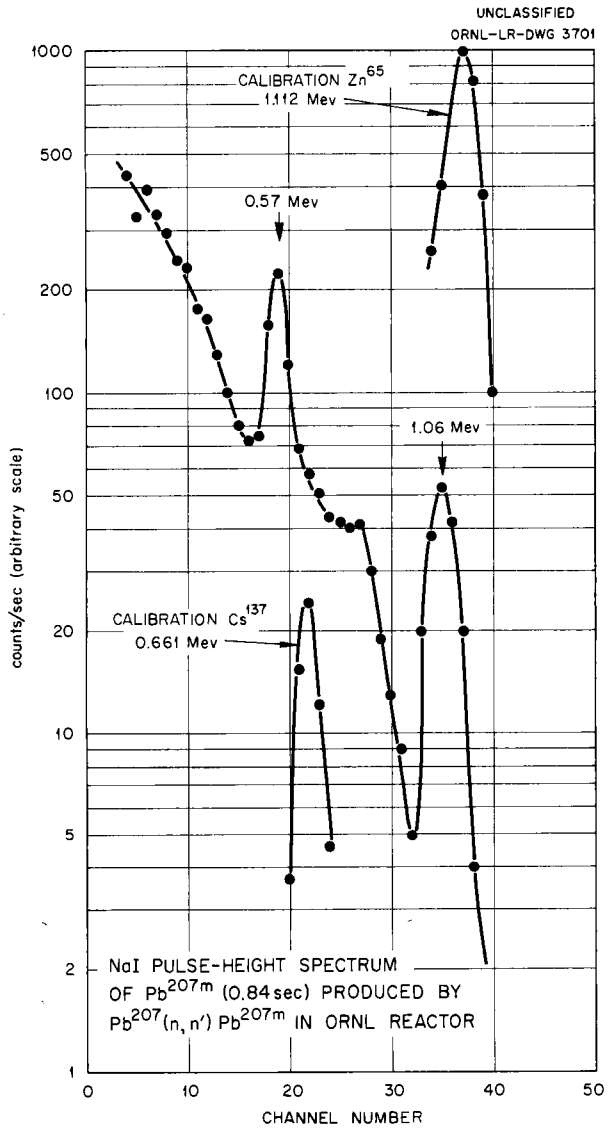

Fig. 2.21. NaI Pulse-Height Spectrum of Pb^{207m} (0.84 sec) Produced by $Pb^{207}(n,n')Pb^{207m}$ in ORNL Graphite Reactor.

SEARCH FOR ISOMER DAUGHTER OF Nb^{90}

F. Nelson[14] E. C. Campbell

In order to decide whether or not the gamma ray associated with the decay of the 0.8-sec isomer produced by fast neutrons on Zr^{90} was identical with the 2.2-Mev gamma ray found in the decay of Nb^{90}, a rapid anion-exchange-resin separation of zirconium from niobium was made. It was established that the 0.8-sec activity is not a daughter of Zr^{90}.

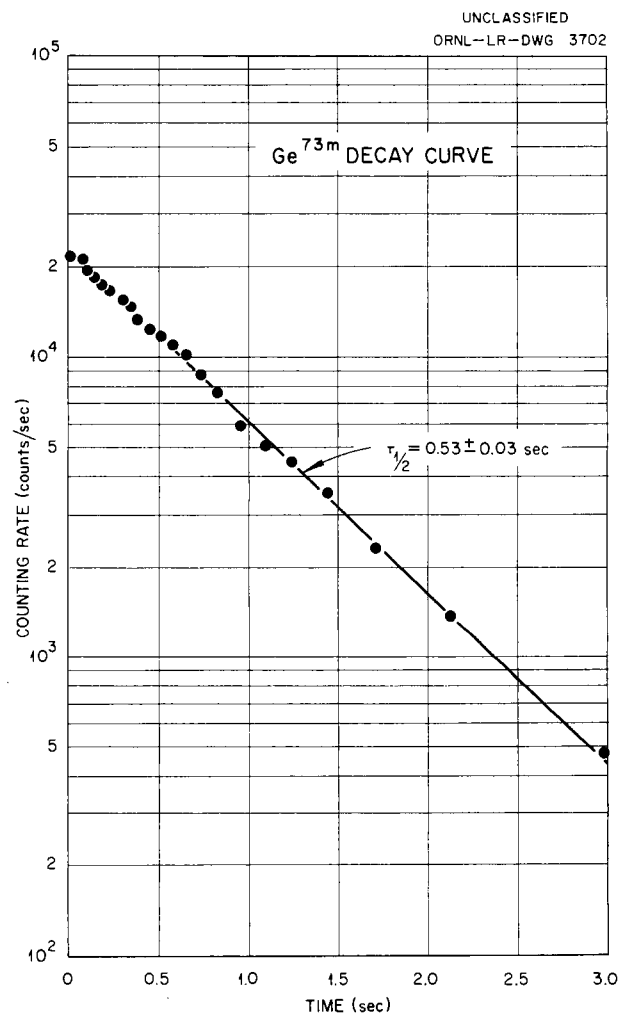

Fig. 2.22. Ge^{73m} Decay Curve; Single-Channel Analyzer Set at 54 kev.

SEARCH FOR O^{20}

R. K. Sheline E. C. Campbell
R. W. Peelle

An unsuccessful search was made for O^{20} by irradiating (in the fast pneumatic tube of the ORNL Graphite Reactor) the compound LiOH enriched in Li^6 and O^{18} (1.5%). It was thought that O^{20} produced in the reaction $O^{18}(t,p)O^{20}$ by the fast tritions from the $Li^6(n,\alpha)H^3$ might be observed. The scintillation spectrometer was set to observe the 1.64-Mev gamma ray associated with the decay for F^{20} (12 sec) which might be expected to grow in from the decay of its supposed parent, O^{20}. Several exposures of a single sample were made. No activity attributable to O^{20} could be observed.

SEPARATION OF Ge^{73m} FROM As^{73} AND OF Ir^{191m} FROM Os^{191}

F. Nelson[14] E. C. Campbell

A rapid chemical separation method has been used to show that the new 0.5-sec isomer found in germanium irradiated by neutrons in the ORNL Graphite Reactor is identified with a metastable excited state of Ge^{73}. The same activity is produced in the electron-capture decay of the 76-day As^{73}. In the separation process which makes use of the well-known volatility of $GeCl_4$, gas was bubbled through a solution containing the radioactive As^{73}, and this gas swept $GeCl_4$ out of the solution into an NaI scintillation counter. Measurements of the decrease in the observed activity taken with the counter at various distances from the bubbling solution, together with measurements of the gas flow, have given a value for the half life which is in fair agreement with the previous result.

Since it has been found that osmium could be strongly adsorbed from chloride solutions by Dowex-1 and since iridium under the same conditions showed very little adsorption, attempts were made to isolate the Ir^{191} isomer, which was suspected to be formed in the decay of Os^{191}. By using an anion-exchange technique and very short columns, it was possible to isolate the Ir^{191} isomer and to determine its half life to be 4.9 sec.

ANGULAR CORRELATION OF GAMMA RAYS

E. D. Klema

Tellurium-124

The directional angular correlation of the 1380–720-kev gamma-gamma cascade in Te^{124} has been measured in a series of seven experiments with a total of 4.7×10^4 coincidence counts obtained at 19 angular positions. The correlation function obtained, after correcting for the finite angular resolution of the detectors, is

$$W(\theta) = 1 - (0.020 \pm 0.013)P_2(\cos\theta) + (0.017 \pm 0.021)P_4(\cos\theta) .$$

This measurement, along with other information, allows one to conclude that the cascade does not consist of two pure radiations; at least one of the transitions is mixed. However, there are several assignments of spin and parity of the intermediate state which, on the basis of this experiment, cannot be differentiated.

Lead-207

The angular correlation of the 1770–570-kev gamma-gamma cascade in Pb^{207} has been measured in a series of five experiments with a total of 8.7×10^4 counts. The correlation function found is

$$W(\theta) = 1 - (0.0087 \pm 0.0089)P_2(\cos\theta) + (0.029 \pm 0.014)P_4(\cos\theta) .$$

Again, in this case, one can rule out the possibility that both transitions in the cascade consist of pure radiation. The correlation functions appropriate to the various possibilities of one mixed and one pure radiation are being calculated on the ORACLE.

Chromium-52

All three of the possible gamma-gamma correlations of the 730–940–1460 triple cascade in Cr^{52} have been measured, and the data are undergoing analysis.

3. NEUTRON DIFFRACTION

NEUTRON-DIFFRACTION STUDIES OF PEROVSKITE-TYPE COMPOUNDS $LaRO_3$

W. C. Koehler E. O. Wollan

Neutron-diffraction data have been obtained for a number of perovskite-type compounds of the form $La^{3+}R^{3+}O_3$ in which R^{3+} is a trivalent ion of the 3*d* transition series. In the preceding semiannual report,[1] preliminary results for $LaMnO_3$ and for mixed oxides of $LaMnO_3$–$CaMnO_3$ were presented. A further consideration of this problem is given in the next section. In the past six months the compounds $LaVO_3$, $LaCrO_3$, $LaFeO_3$, and $LaCoO_3$ have been investigated.

These compounds were prepared by firing stoichiometric mixtures of the sesquioxides of lanthanum and the appropriate transition metal in a suitable atmosphere, and the preparations were all followed by x-ray diffraction examination. Neutron-diffraction data were obtained at room temperature, at one or more reduced temperatures, and also at the temperature of boiling water in several cases.

A summary of the neutron-diffraction results is shown in Table 3.1. Of the five oxides which have so far been examined, antiferromagnetic structures have been found for $LaCrO_3$, $LaMnO_3$, and $LaFeO_3$, but the structure for $LaMnO_3$ was different from that for $LaFeO_3$ and $LaCrO_3$. As we have previously mentioned, the magnetic structure of $LaMnO_3$ is a layer type. Manganese ions are coupled ferromagnetically in sheets, and adjacent layers are then coupled with opposite spins. This structure is designated in Table 3.1 as *A*. With respect to the iron and chromium compounds, the magnetic structure is similar to that previously found for $CaMnO_3$, in which each ion is surrounded by six antiferromagnetically coupled nearest neighbors. This structure is designated as *G*. The approximate transition temperatures indicated for $LaCrO_3$ and $LaMnO_3$ were obtained by following the intensity of a magnetic-scattering maximum during warmup from low temperature. The transition temperature of $LaFeO_3$ has not yet been determined, but it is known to be higher than 100°C. Of the remaining oxides, no magnetic ordering has been found for $LaVO_3$ at temperatures down to 20°K or for $LaCoO_3$ to 4.2°K.

In these compounds the transition-group atoms are present in the form of trivalent ions, and, as such, their magnetic properties are due to a definite number of unpaired 3*d* electrons which range from two in V^{3+} to four in Co^{3+}, where the 3*d* shell is more than half filled. If the distortions of the structures from the ideal perovskite structure are neglected, the transition metal ions are arrayed on a simple cubic lattice and are separated by oxygen ions situated midway between them. According to Anderson,[2] this linear array is favorable for a superexchange coupling of transition-metal

[1] E. O. Wollan and W. C. Koehler, *Phys. Semiann. Prog. Rep. March 10, 1954*, ORNL-1705, p 34.

[2] P. W. Anderson, *Phys. Rev.* **79**, 350 (1950).

TABLE 3.1. NEUTRON-DIFFRACTION RESULTS FOR PEROVSKITE-TYPE COMPOUNDS $LaRO_3$

Compound	Number of Unpaired 3*d* Electrons	Magnetic Structure	Neél Temperature (°K)	Crystallographic Data
$LaVO_3$	2			Cubic, $a_1 = 7.842$ Å
$LaCrO_3$	3	*G*	~300	Monoclinic, $a_1 = a_3 = 7.777$ Å, $a_2 = 7.750$ Å, $\beta = 90°15'$
$LaMnO_3$	4	*A*	~140	Monclinic, $a_1 = a_3 = 7.960$ Å, $a_2 = 7.698$ Å, $\beta = 91°52'$
$LaFeO_3$	5	*G*	>373	Cubic, $a_1 = 7.852$ Å
$LaCoO_3$	4			Rhombohedral, $a_1 = 7.651$ Å, $\alpha = 90°40'$

ions via the intermediate oxygen ion. However, Anderson's theory predicts that if both ions of the pair have less than five $3d$ electrons a positive exchange coupling will result. This is clearly not the case in $LaCrO_3$, although in $LaMnO_3$ some positive coupling does appear to exist; in fact, twice as many ion pairs are ferromagnetically coupled as are antiferromagnetically coupled. For ion pairs having five or more $3d$ electrons, the theory predicts negative exchange coupling. More recently, Polder[3] has taken into account the effect of electrostatic crystalline field interactions and has found that for ions containing less than five $3d$ electrons either positive or negative coupling may be expected.

It should be emphasized, however, that the structures of all the compounds, to a greater or lesser degree, are distorted from the ideal perovskite lattice. Although the x-ray diffraction patterns of $LaVO_3$ and $LaFeO_3$ suggest cubic symmetry, a number of weak lines appear which require a large unit cell. In $LaCoO_3$ the strong lines of the simple cell are split in a manner characteristic of a rhombohedral cell, and in $LaCrO_3$ and $LaMnO_3$ the splitting is either monoclinic or orthorhombic. The greatest distortion occurs in the $LaMnO_3$ structure, in which distances in the a_1, a_3 plane appear abnormally large as compared with the a_2 lattice period. It is not possible, from the neutron powder data alone, to determine along which of the crystallographic directions the moments are directed; it is reasonable, however, to assume that the moments are coupled ferromagnetically in the a_1, a_3 plane.

Now the indirect exchange coupling between two manganese-ion spins, separated by an oxygen ion, is effected, according to Anderson, by an excited state in which one of the oxygen $2p$ electrons goes over into one of the manganese ions. The coupling energy depends sensitively upon the overlap between the p and d orbitals and also upon the energy of promotion of the p electron to the d orbital with spin parallel or antiparallel to the original d electrons. If it can be assumed that the energy term is independent of crystal direction in $LaMnO_3$, then the sign of the interaction in, and normal to, the a_1, a_3 plane will be governed by the sign of the p-d exchange integral. Factors which may affect this sign are the differences in separations of the ions in different directions, departures from linearity of the Mn–O–Mn configurations, and the anisotropic charge distribution in trivalent manganese ion. It is tempting to regard the separations as an important factor, since both Cr^{3+} and Mn^{3+} have asymmetric ground-state charge distributions (F and D states, respectively) and for $LaCrO_3$, where the distortions are small, the same type of coupling is found for all nearest neighbors. However, if the separation is the important parameter, then the p-d exchange integral would presumably be on either side of zero for the two directions of the $LaMnO_3$ crystal, and one might expect the coupling energy to be low. This is measured roughly by the Neél temperature, and indeed the transition point is appreciably below that of $LaCrO_3$ and $LaFeO_3$ but still represents on an absolute scale a substantial interaction energy.

Presumably the magnitude of the exchange integral is very small in $LaVO_3$ and $LaCoO_3$. Further work is planned on these compounds to improve the sensitivity of the measurement and also on $LaTiO_3$ and $LaNiO_3$ in order to complete the series of accessible trivalent transition-element oxides.

It is a pleasure to acknowledge the cooperation of H. L. Yakel, Jr., in making the x-ray diffraction measurements and to thank D. E. LaValle for his assistance with the chemical preparations.

CONTINUATION OF MAGNETIC STUDY OF THE SERIES OF COMPOUNDS $[xLa, (1-x)Ca]MnO_3$

E. O. Wollan W. C. Koehler

A considerable proportion of the experimental data for this problem has already been presented in the preceding semiannual report (ORNL-1705). To recapitulate briefly, these compounds were found by Jonker and Van Santen[4] to be ferromagnetic over the composition range $x = 1$ to $x = 0.5$; see the saturation moments reproduced here as the solid curve in Fig. 3.1. (It is actually not the La-Ca composition which is important but rather the proportion of Mn^{3+} and Mn^{4+}, which depends also to some extent on the firing temperature used in the sample preparation.) In the neutron-diffraction study, patterns were obtained at room temperature and at temperatures below the Curie or Neél points for a series of values of

[3] M. D. Polder, *J. phys. radium* 12, 126 (1951).

[4] G. H. Jonker and J. H. Van Santen, *Physcia* 16, 337 (1950); 19, 120 (1953).

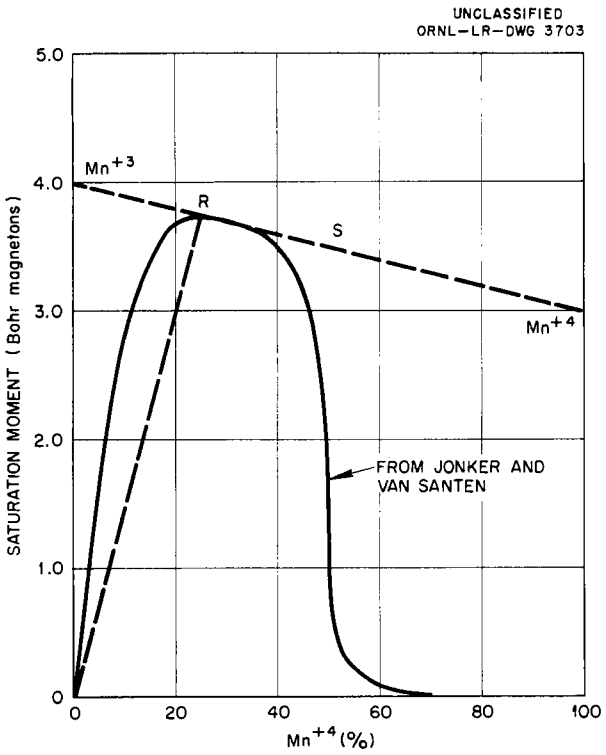

Fig. 3.1. Saturation Magnetization vs Composition.

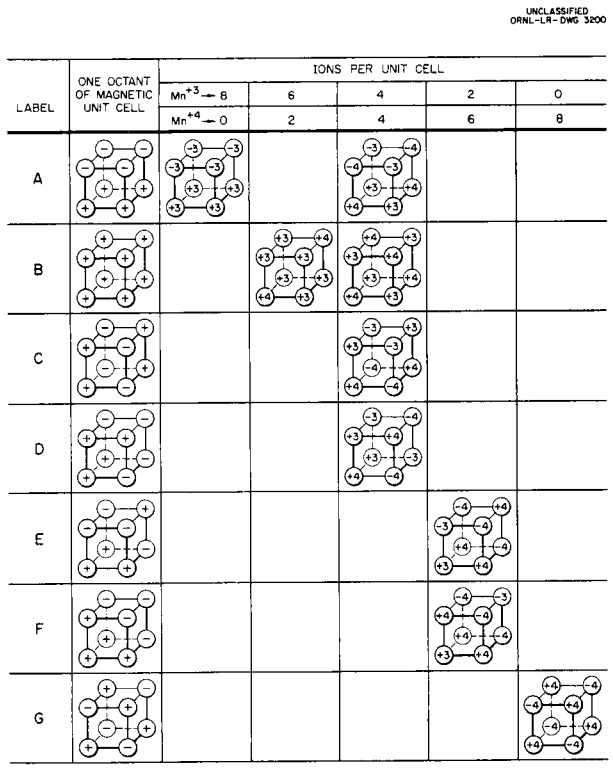

Fig. 3.2. Possible Magnetic Structures in [xLa, (1 – x)Ca]MnO_3. The plus and minus signs refer to opposite spin directions in the crystal. The numbers 3 and 4 refer to Mn^{3+} and Mn^{4+}, respectively.

x from 1 → 0, the results of which were presented in terms of the difference $I_{T°C} - I_{300°C}$ which represent primarily the magnetic scattering features as a function of composition. Ferromagnetic reflections were observed over the range $x \cong 0.9$ to 0.5, and over most of this range simultaneous occurrence of both ferro- and antiferromagnetic reflections was also observed. Patterns corresponding to several types of antiferromagnetic structure were obtained for $x = 1$ and $x \to 0.5$ to 0. A partial discussion of these magnetic structures has been given; they are now more completely represented here in the first column of Fig. 3.2.

The structures *A*, *C*, *D*, *E*, *F*, and *G* represent all the possible ways in which equal numbers of + and – moments can be ordered into cells in which none of the three dimensions are greater than twice those of the fundamental chemical cell. *B* represents the special case of ferromagnetism. Since the last report, a pattern has been obtained for pure $CaMnO_3$ with essentially 100% Mn^{4+}, and, as expected, the results show the existence of structure *G* in which each Mn^{4+} ion is coupled antiferromagnetically to each of its six nearest neighbors.

In the composition range below 25% Mn^{4+} and near 50% Mn^{4+}, both ferromagnetic scattering contributions which occur at the positions of the nuclear peaks and superstructure reflections are simultaneously observed. On the basis of the intensity data it was assumed that these two types of reflections corresponded to the existence of individual domains of ferro- and antiferromagnetism. To rule out the possibility that these apparently mixed patterns could not be accounted for on the basis of a type of ferrimagnetic cell, the intensities of the two types of reflections were studied at 77°K with and without a magnetic field applied along the scattering vector (see next section for equipment details). With a sample containing about 15% Mn^{4+} it was found that the magnetic contributions at the positions of the nuclear peaks (ferromagnetic) disappeared as expected when the

field was applied, but no diminution of intensity was observed in the superstructure reflections. This confirms the previous conclusion that in this composition range there is a coexistence of independent ferromagnetic and antiferromagnetic regions or domains in the crystallites.

Up to now nothing has been said about the possible ordering of the Mn^{3+} and Mn^{4+} ions in the crystals and how this ordering might be expected to change with, or be a determining factor for, the particular magnetic structure found for the various compositions.

From even a casual consideration of the data one is led to the conclusion that in this series of compounds the superexchange coupling through the oxygen ion intermediary is ferromagnetic between Mn^{3+} and Mn^{4+} ions, antiferromagnetic between Mn^{4+} and Mn^{4+} ions, and either ferromagnetic or antiferromagnetic between Mn^{3+} and Mn^{3+} ions, depending on the value of the ionic separation and probably also on the amount of puckering of the intervening oxygen bonds, as well as on other crystallographic factors.

If one accepts these conclusions, then one is led also to the conclusion that ordering of the moments on magnetic lattices will be accompanied by an ordering of the Mn^{3+} and Mn^{4+} ions on correspondingly appropriate lattice sites. This ordering requires only that electrons can shift readily from one ion to another.

On the basis of these hypotheses it is then possible to order the magnetic structure data into a reasonably self-consistent scheme. The results are shown in Fig. 3.2. Pertient points relative to some of these proposed structures will be considered in the order in which they appear. For convenience they will be labeled with the letter in the first column and the Mn^{3+}, Mn^{4+} content in the last five column headings.

A-8-0

Since this structure consists of like ions, one must look to a crystallographic origin for the fact that there is ferromagnetic coupling along two axes and antiferromagnetic coupling along the third axis. X-ray patterns taken at room temperature show this composition to be monoclinic with $a = c = 7.96$ Å, $b = 7.70$ Å, and $\angle ac = 91.5$ deg. (This work was done by H. L. Yakel, Jr.; cf. "On the Structures of Some Compounds of the Perovskite Type," this section.)

It seems logical to associate the smaller b axis (see Fig. 3.3) with the unique axis in the magnetic cell. If one considers the separation distance as the explicit variable affecting the exchange coupling, then the critical distance for ferro- and antiferromagnetic coupling for Mn^{3+}–O–Mn^{3+} must lie somewhere between 7.96 and 7.70 Å. A secondary factor associated with the cell spacing is the puckering of the oxygen bonds, which has been suggested by Megaw[5] from x-ray intensity studies and which is required to account for the intensity of the nuclear peaks in the neutron pattern. The largest spacing, 7.96 Å, observed here is close to the value of 8.08 Å obtained from the sum of the ionic radii. The shorter spacing of 7.7 Å must then correspond to an appreciable puckering of the oxygen bond. If we consider the oxygen and manganese atoms to be hard contacting spheres, then the separation distance can be thought of as the unique parameter, the oxygen

[5] H. D. Megaw, *Acta Cryst.* 5, 739 (1952); 7, 187 (1954).

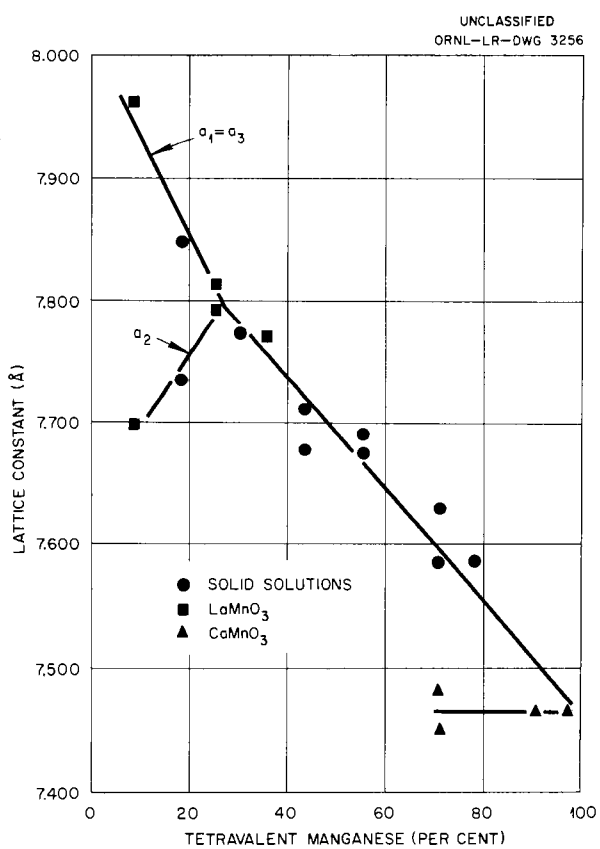

Fig. 3.3. Cell Spacing vs Composition.

bond angles being thus determined, at least in some arbitrary plane, by the spacing values. It is, of course, possible also that ion asymmetry can be a factor, but this could also be reflected in the separation distances. It thus seems justifiable to consider the spacing as the primary variable affecting the exchange.

As one progressively increases the Mn^{4+} content of these compounds from 0 → 0.5, the *A*-8-0 antiferromagnetic phase diminishes, ferromagnetism grows in, and the saturation moment reaches a maximum at about 25% Mn^{4+} and rather abruptly falls off at 50% Mn^{4+}.

B-6-2

With a relatively strong ferromagnetic coupling for Mn^{3+}–O–Mn^{4+}, one is led to predict the magnetic cell shown in column four of Fig. 3.2 for the 6-2 (25% Mn^{4+}) composition. If the cell required the full 25% Mn^{4+} composition for ferromagnetism, the saturation moment would follow the dashed line from 0 → 25% Mn^{4+} in Fig. 3.1. The shape of the measured saturation-moment curve shows that somewhat less than 25% Mn^{4+} is required for the ferromagnetic ordering.

B-4-4

The cell shown in the fifth column of Fig. 3.2 is likewise satisfactory for ferromagnetic coupling, and growth of this cell would hold the saturation moment along the line *R*–*S* to 50% Mn^{4+}. If the only competing interaction at this point were from the Mn^{4+}–O–Mn^{4+} antiferromagnetic exchange, one would expect a gradual decrease of ferromagnetism toward 100% Mn^{4+} content. One still has, however, the Mn^{3+}–O–Mn^{3+} exchange, and it seems probable that this plays an important role in bringing about the sudden change from ferromagnetic to antiferromagnetic ordering at about 50% Mn^{4+}.

At a composition of about 40% Mn^{4+} the average cube-edge spacing becomes smaller than the value 7.7 Å for which there is antiferromagnetic coupling of the Mn^{3+} ions in the *A*-8-0 form. It is to be noted also that at 40% Mn^{4+} content the saturation moment begins to drop off rather rapidly. These facts suggest that strong competition sets in between the Mn^{4+}–O–Mn^{3+} ferromagnetic exchange, which may be decreasing in strength as the spacing decreases, and antiferromagnetic exchange between Mn^{3+} ions and between Mn^{4+} ions, the strength of both of which may be increasing with decreasing spacing. Such a trend in the exchange coupling could easily account for the sudden falloff of the saturation moment at 50% Mn^{4+}.

Antiferromagnetic Cells with Mn^{4+} Content Greater Than 50%

If no account is taken of the possible decrease in strength of the Mn^{4+}–O–Mn^{3+} ferromagnetic coupling with progressive decrease in spacing value, the magnetic cell *A*-4-4 would seem to be quite stable. The fact that there is no evidence for this structure would indicate that other structures are more stable. A relatively clean pattern for a *C*-type cell was obtained, but it was not entirely certain from the analysis that it should be placed in the 4-4 (50% Mn^{4+}) class. It seems impossible, however, to arrive at a logical ordering of the moments if it were of the form *C*-2-6. If this form, which best fits the general trend, is accepted, one would conclude, since *C*-4-4 with four ferromagnetic bonds has an apparent greater stability than *A*-4-4 with eight ferromagnetic bonds, that at this value of the lattice spacing the ferromagnetic coupling is rapidly becoming weaker than the antiferromagnetic coupling.

Although no clean patterns have been obtained for *D*-4-4 and *E*-2-6, there is strong evidence for them from patterns which can be interpreted as mixtures of *C* and *E* and of *D* and *G*. No evidence exists for *F*, a fact which is again consistent with the progressive importance of antiferromagnetic over ferromagnetic coupling.

NEUTRON-DIFFRACTION SPECTROMETER WITH CRYOSTAT AND MAGNETIC FIELD

E. O. Wollan W. C. Koehler

In studies of magnetic scattering of neutrons it is frequently necessary to apply magnetic fields to the sample in order to separate the magnetic and nuclear scattering, to determine the direction of the magnetic vector relative to the crystalline axes, and to aid in distinguishing between ferrimagnetism and mixtures involving both ferro- and antiferromagnetic ordering (see next section).

It is convenient to have the field direction in the plane of scattering (horizontal plane), and in addition it should be possible to rotate the field to bring it into coincidence with the scattering

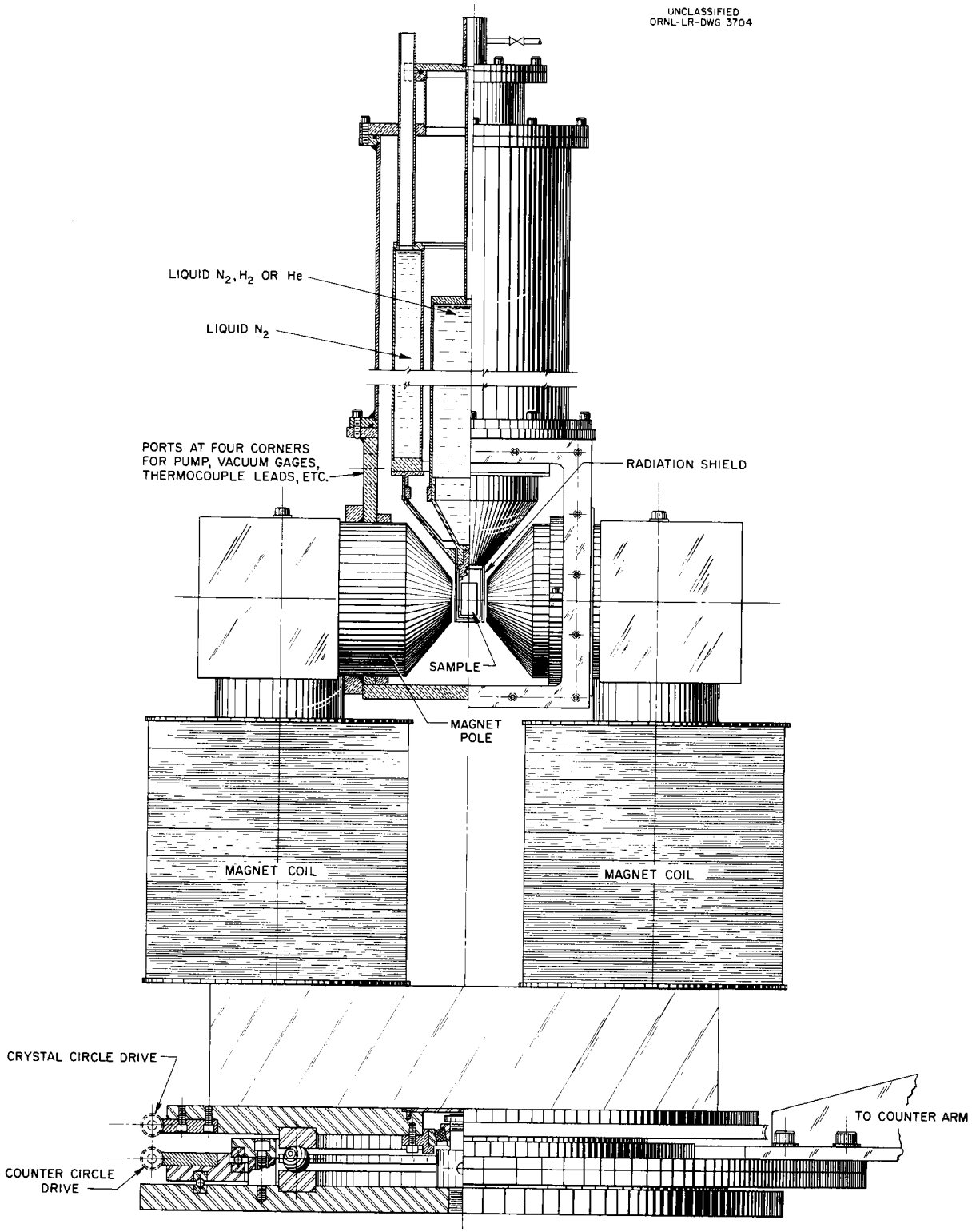

Fig. 3.4. Neutron Spectrometer with Cryostat and Magnetic Field.

vector. The coherent magnetic-scattering intensity is proportional to $\sin^2 \alpha$, where α is the angle between the scattering vector and the magnetic-moment vector in the scattering crystallite. Application of a sufficiently strong field (usually a few thousand oersteds for a ferromagnetic system) along the scattering vector forces the angle α, and thus the magnetic scattering, to zero. Measurements with and without a field thus give a direct measure of the magnetic scattering in a given case.

Since many of the interesting magnetic systems have Curie points at low temperatures, it is desirable to be able to study the sample at low temperatures in a magnetic field. To incorporate a magnetic field at low temperatures required the building of a new spectrometer, which is shown here as an assembly drawing in Fig. 3.4. The magnet and cryostat assembly sits on the crystal table of a low, sturdily built spectrometer. The counter (for which only a part of the support arm is shown) rotates around the center of the crystal table, and the counter and crystal table are geared together in the usual 2 to 1 speed ratio. The flat character of this spectrometer was dictated by the small distance from the floor to the center of the neutron beam from the pile.

The lower part of the cryostat vacuum chamber consists of a brass box sealed around the pole pieces with O-rings. The front and rear faces are O-ring-sealed aluminum covers with thin-wall cylindrical sections for entrance and exit of the neutron beam from the crystal monochromator. The front cover plate is removed for sample mounting and alignment.

The fact that the magnet, cryostat, and sample rotate as a whole makes this arrangement convenient for single-crystal, as well as powdered-crystal, studies.

MAGNETIC STRUCTURE OF NICKEL-IRON ALLOYS

C. G. Shull M. K. Wilkinson

The investigations of the magnetic structure of alloys of the transition elements have been extended to include a series of nickel-iron alloys. It is known from magnetization studies that the ferromagnetism in disordered alloys of nickel-iron becomes stronger with the addition of iron, but these measurements cannot offer information on the individual atomic magnetic moments in the alloys. However, when the magnetization data are combined with results from neutron-diffraction measurements, information of this type can be obtained.

In the disordered state, ferromagnetic binary alloys give rise to a ferromagnetic disorder scattering which is superimposed on the normal diffuse scattering in the neutron-diffraction pattern. This magnetic scattering can be determined as the difference between the diffuse scattering levels when the sample is unmagnetized and when it is magnetized parallel to the scattering vector. The cross section for this type of diffuse scattering is given by the expression

$$d\sigma = 0.0484 g_1 g_2 (\mu_1 - \mu_2)^2 f^2 \times 10^{-24}\ \mathrm{cm}^2/\text{average atom},$$

where g_1 and g_2 are the fractional abundances of the two types of atoms, μ_1 and μ_2 are their magnetic moments expressed in Bohr magnetons, and f is the magnetic-form factor descriptive of the spatial origin of the atomic magnetic moment. Hence, an analysis of the diffuse scattering results in the determination of the difference between the two atomic moments. This difference in the atomic magnetic moments, combined with results from magnetization data, which give the weighted sum of the moments, allows evaluation of the individual moments of the atoms. However, because of the quadratic nature of the above equation, alternative sets of results are obtained, and the experiment does not permit the solution of this ambiguity.

Three members of the nickel-iron series of alloys, which contained 49.9, 60.1, and 74.3 at. % nickel, were prepared and examined. These samples were cast into bar form from inductively heated melts of the electrolytically pure elements, homogeneized at 1300°C in a 95% helium–5% hydrogen atmosphere, and then filed with a tungsten carbide file into a 100-mesh sample preparation. In this state all the alloys showed the face-centered cubic structure with precision lattice-constant values and neutron intensities characteristic of a disordered solid solution. The ferromagnetic disorder scattering for these alloys, obtained from a comparison of the diffuse intensity for the samples unmagnetized and for those magnetized along the scattering vector, is shown in Fig. 3.5. The decrease in scattering at small angles may indicate the presence of short-range magnetic order in the samples. Drawn through the various sets of data is the

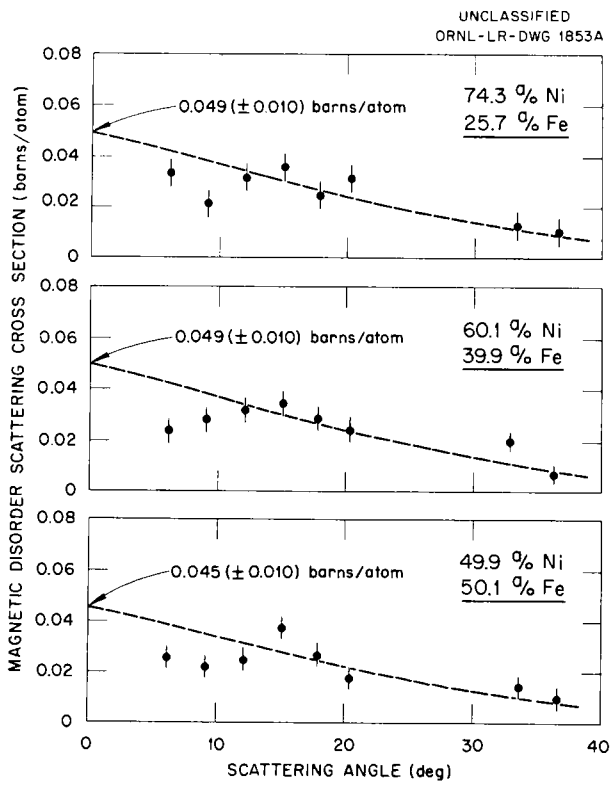

Fig. 3.5. Ferromagnetic Disorder Scattering Obtained for a Series of Disordered Ni-Fe Alloys.

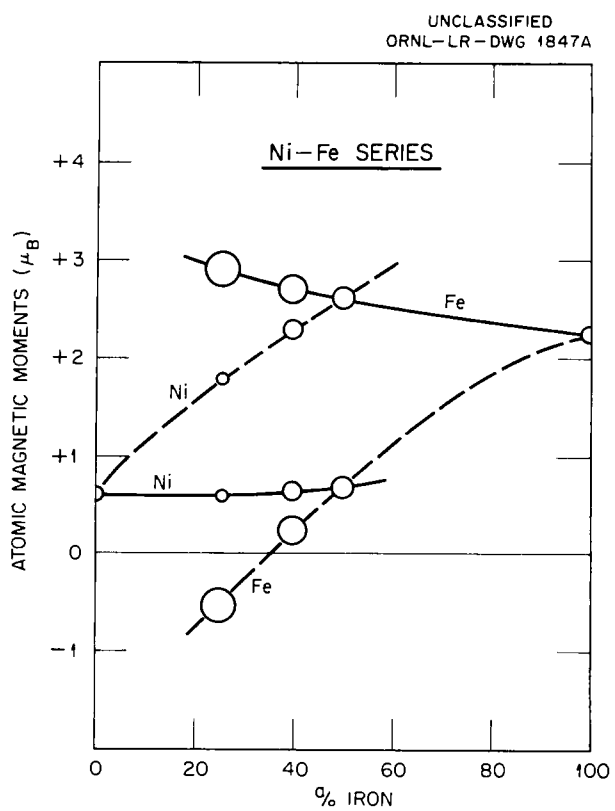

Fig. 3.6. Variation of the Nickel and Iron Atomic Magnetic Moments with Atomic Composition in Disordered Ni-Fe Alloys. Alternative solutions are represented by the points connected either by the solid lines or by the dashed lines. The size of the experimental points is a measure of their accuracy.

magnetic-form factor calculated by Steinberger and Wick for metallic iron. The intercepts of the matched form-factor curves at zero scattering angle can then be used to calculate the differences in the atomic magnetic moments of the nickel and iron atoms. These differences, combined with results from magnetization data, allow the determination of the individual moments, and the alternative sets of solutions are shown in Fig. 3.6, with the size of the points representing their accuracy. Either set of solutions indicates that the nickel moment increases when iron is added, but the possible iron moments differ widely in the two solutions.

In addition to the investigations of the disordered alloys, a portion of the 74.3 at. % nickel alloy was ordered, and the magnetic structure of the ordered alloy was determined. In investigations of ordered ferromagnetic alloys, the magnetic scattering present in the superstructure lines is also determined by a study of magnetized and unmagnetized samples. This magnetic scattering is again proportional to the square of the difference of the atomic magnetic moments of the two types of atoms, and the analysis is similar to that for the disordered samples, giving alternative sets of moments. This sample of Ni_3Fe was given a very elaborate ordering heat treatment, and indirect evidence indicated a long-range order parameter of about 0.9. The magnetic-scattering data agreed very closely with those for another sample of Ni_3Fe which was studied previously, and the results obtained for the magnetic moments were very close to the values obtained for the disordered sample of the same composition.

From these investigations it appears that ordering of the lattice has little or no effect on the component magnetic moments. This suggests that the local electron concentration of surrounding atoms

has little effect on the magnetic moment and hence on the electron configuration of a central atom. Rather, the over-all lattice composition seems to determine the individual moments. Changing the composition is seen to change the local moments, although the significance of this is obscured because of the alternative sets of moment values consistent with the experimental data.

MAGNETIC STRUCTURE OF Mn_2Sb

M. K. Wilkinson C. G. Shull

Additional neutron-diffraction experiments have been performed to determine the magnetic structure of Mn_2Sb. This material has a tetragonal unit cell containing two molecules, with the manganese atoms located at positions with coordinates of (0, 0, 0); (½, ½, 0); (0, ½, Z_1); (½, 0, $\overline{Z}_1$), while the antimony coordinates are (0, ½, Z_2) and (½, 0, $\overline{Z}_2$). Recent neutron and x-ray data have indicated that the published values for Z_1 and Z_2 are in error and that the correct values are 0.295 and −0.280. According to a model by Guillaud which was based on macroscopic magnetic measurements, this material is a *ferrimagnetic* substance in which the two manganese atoms possess different atomic magnetic moments that are coupled in an antiparallel arrangement. Specifically, this model predicts that in the temperature range from 240°K to the Curie temperature of 550°K the magnetic moments are directed along the *c*-axis of the unit cell. At temperatures below 240°K, the direction of the moments is changed and they are located in the base plane of the unit cell. Guillaud predicts values of 3 and −5 Bohr magnetons for the values of the atomic moments, and his magnetic data indicate that at room temperature the magnetization is 71% of its value at absolute zero. Previous neutron-diffraction investigations have been performed on this material with powdered samples, and data taken at various temperatures from 78°K through the Curie temperature were found to agree in general with the suggested model. However, the complexity of the powder diffraction patterns and the difficulties of analysis did not permit a straightforward determination of the magnetic-scattering amplitudes and the corresponding magnetic moments.

In order to overcome some of these difficulties, a neutron-diffraction investigation was performed which employed single crystals of the material. These specimens were in the form of small pillars cut from a large single crystal along various crystal planes so that studies could be made of the important magnetic reflections. They were placed between the pole pieces of an electromagnet which could produce a magnetic field of approximately 9000 oersteds across a gap of ⅝ in., and data were taken with the samples magnetized and unmagnetized. Since the magnetic contribution to the observed intensity depends upon the orientation of the atomic magnetic moments of the scattering specimen with respect to the scattering vector, the amount of magnetic scattering could be changed by the application of the external magnetic field. In these single-crystal investigations, the magnetic field was applied in the direction which would give the largest change in intensity from that of the unmagnetized sample for the particular reflection being studied. The neutron-diffraction patterns shown in Fig. 3.7 are typical of those which were obtained. These patterns show the neutron reflectivities for the (00*l*) planes taken for the sample unmagnetized and for the sample magnetized along the (00*l*) planes perpendicular to the scattering vector. In

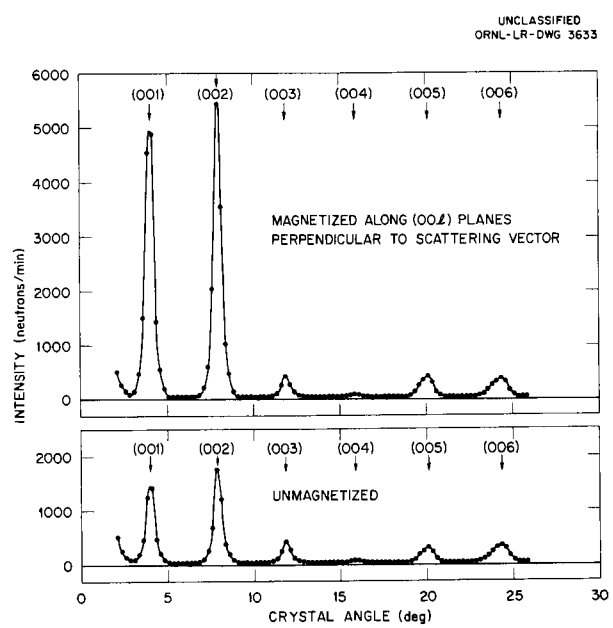

Fig. 3.7. Neutron-Diffraction Patterns of the (00*l*) Single-Crystal Reflections from Mn_2Sb. The lower pattern represents data obtained with the sample unmagnetized, and the top pattern was taken with the sample magnetized along the (00*l*) planes perpendicular to the scattering vector.

the unmagnetized sample there was no contribution from magnetic scattering, while for the magnetized sample, the entire magnetic scattering allowed by the structure factor was present in the diffraction peaks. The difference in the intensities in the two cases was therefore a measurement of the magnetic contribution in the reflections. The magnetic-scattering amplitude for each reflection was calculated from the ratio of observed magnetic intensity to observed nuclear intensity, together with the value of the nuclear-scattering amplitude for the particular reflection as calculated from the known nuclear-scattering amplitudes of manganese and antimony. These magnetic-scattering amplitudes were referred to zero scattering angle with the use of the magnetic-form factor determined experimentally for the divalent manganese ion by Erickson. With the observed values of magnetic-scattering amplitudes and the calculated expressions from known structure parameters, an equation was obtained for each magnetic reflection which contained the magnetic-scattering amplitudes, $f_{Mn(I)}$ and $f_{Mn(II)}$ for the two manganese atoms. These equations are represented graphically in Fig. 3.8. Only those reflections with a reasonably large magnetic contribution are plotted. Furthermore, because of the rather large differences in the various experimental and calculated magnetic-form factors at large values of sin θ/λ, no reflections at large scattering angles were considered. The experimental data were obtained for several pillars with different cross-sectional areas and were found to be quite reproducible. The magnetic-scattering amplitudes are thus determined to be $0.496 \cdot 10^{-12}$ cm and $-0.765 \cdot 10^{-12}$ cm.

It was of interest to make an experimental determination of the degree of magnetic saturation at room temperature for the particular sample of Mn_2Sb which was studied. This was accomplished by placing one of the small crystals in a low-temperature cryostat and by measuring the (001) and (002) reflectivities as the temperature of the specimen was lowered to 78°K. Measurements of the (001) peak intensity as a function of temperature are shown in Fig. 3.9. The sharp intensity change at about 250°K is due to the change in direction of the atomic magnetic moments from the c-axis to the base plane of the unit cell. Neutron data indicate that in the low-temperature region the moments are aligned along the other two cell axes. At temperatures above the transition, there is no magnetic scattering in the (001) reflection, while at the lower temperatures the full magnetic contribution is present. The absolute temperature measurements were not particularly accurate; therefore the difference between the transition temperature for the neutron data and the value of 240°K obtained by Guillaud is not considered significant. A comparison of the magnetic intensity at low temperatures to that ob-

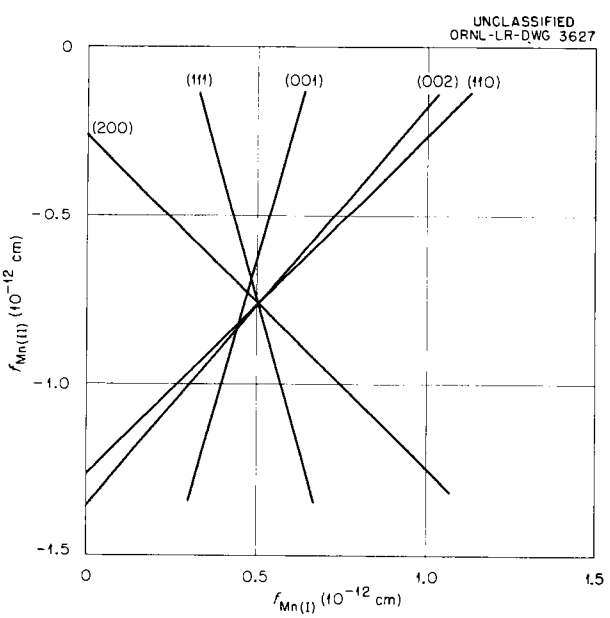

Fig. 3.8. Magnetic-Scattering Amplitudes of the Most Significant Magnetic Reflections from Mn_2Sb Plotted as a Function of the Individual Magnetic-Scattering Amplitudes, $f_{Mn(I)}$ and $f_{Mn(II)}$, of the Two Manganese Atoms.

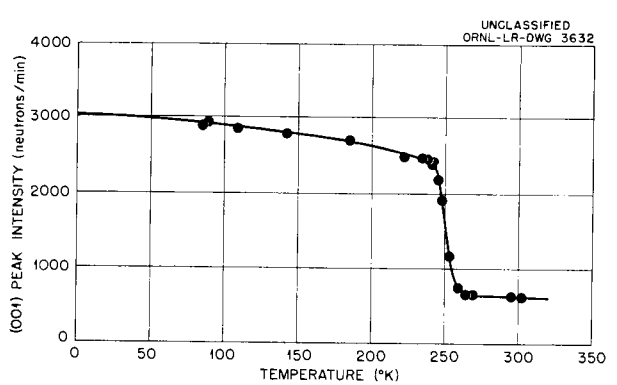

Fig. 3.9. Variation of the (00*l*) Peak Intensity from Mn_2Sb with Temperature.

tained in the electromagnet at room temperature for the (001) and (002) reflections indicated that the ratio of the magnetization at room temperature to that at absolute zero was 0.78. This is to be compared with the value of 0.71 obtained by Guillaud for his sample.

With the experimental determinations of the magnetic-scattering amplitudes and the degree of magnetic saturation, the values of the atomic magnetic moments for the two manganese atoms were found to be 2.36 and −3.63 Bohr magnetons. These values do not agree with those previously predicted by Guillaud. One possible cause for this discrepancy is a difference in the exact chemical composition of the two samples. A chemical analysis is now in progress for the samples studied at this laboratory. Further investigations and interpretations will await the results of this analysis.

STUDY OF $CuCl_2 \cdot 2H_2O$

T. J. Turner[6] W. C. Koehler
E. O. Wollan

Since the discovery by Poulis and Hardeman[7] that $CuCl_2 \cdot 2H_2O$ becomes antiferromagnetic at a temperature (T_c = 4.3°K) just above that of liquid helium, many studies of the properties of this compound at low temperatures have been made. These include specific heat, susceptibility, and magnetic-resonance studies. Although indirect evidence as to the magnetic structure has been obtained from the magnetic-resonance studies, it was felt that the direct neutron-diffraction approach to the structure would be desirable. In addition to the magnetic study it would also be of interest to obtain neutron-diffraction data on the proton positions in the crystal, since these play a role in the interpretation of the magnetic-resonance results. Runs at room temperature on both powdered and single crystals have indicated the feasibility of determining the hydrogen parameters. Preliminary results show reasonable agreement with the values given by Poulis and Hardeman, but the indications are that relatively small but significant changes in these values will be required. No magnetic-scattering results are yet available from preliminary low-temperature data.

[6] Research participant, Wake Forest College, N. C.

[7] N. J. Poulis and G. E. G. Hardeman, *Physica* 18, 201 (1952); 18, 315 (1952).

ON THE STRUCTURES OF SOME COMPOUNDS OF THE PEROVSKITE TYPE

H. L. Yakel, Jr.[8]

Introduction

Current crystallographic interest in compounds of the type ABO_3 which have structures closely related to the so-called perovskite structure stems from the unusual physical properties of these substances.[9] While a complete description of the small atomic displacements responsible for the pseudosymmetric structures so often found in such compounds seems to require single-crystal diffraction data,[10,11] much useful information can be derived from the unit-cell dimensions and apparent lattice symmetries observed in powder-diffraction experiments.[12]

It is the purpose of this paper to describe the x-ray powder-diffraction results obtained for a group of compounds of the perovskite type whose neutron-diffraction patterns at liquid-nitrogen temperatures indicate the presence of several interesting ferromagnetic and antiferromagnetic structures.[13] All the x-ray experiments were performed at room temperatures, but it was hoped that they would provide some clues to the behavior of the compounds at low temperatures.

Experimental Procedure

The compounds (nominal, not necessarily actual, formulas) included in the present investigation were $LaMnO_3$, $CaMnO_3$, $LaCoO_3$, $SrCoO_3$, $LaFeO_3$, $SrFeO_3$, $LaCrO_3$, and $LaVO_3$. Some solid solutions of the type $[xLa, (1 - x)Ca]MnO_3$, $[xLa, (1 - x)Sr]CoO_3$, etc., were also studied. Pure compounds and solid solutions were prepared from stoichiometric amounts of the appropriate oxides, hydroxides, or carbonates by firing at temperatures in excess of 1000°C in atmospheres ranging from pure oxygen to 99% N_2–1% O_2 for periods of 2 to 25 hr. Chemical analyses for tetrapositive transition-metal ions were made as a check on the purity of the compound preparations

[8] Member of Metallurgy Division. This report is included here because of its relation to neutron-diffraction studies of the same compounds.

[9] H. D. Megaw, *Acta Cryst.* 5, 739 (1952); 7, 187 (1954).

[10] H. T. Evans, Jr., *Acta Cryst.* 4, 377 (1951).

[11] P. Vousden, *Acta Cryst.* 4, 545 (1951); 7, 321 (1954).

[12] P. Vousden, *Acta Cryst.* 4, 373 (1951).

[13] E. O. Wollan and W. C. Koehler, work to be published.

and on the accuracy of the nominal solid-solution compositions. As an example of the effects of varying temperatures and atmospheres on the resultant preparations, it was found that $LaMnO_3$ samples prepared at temperatures of 1100 to 1400°C in air or nitrogen atmospheres, with long firing periods, contain about 8 to 10% Mn^{4+}, while samples of the same substance prepared at 1000°C in pure oxygen, with short firing times, contain as much as 35% Mn^{4+}. The ease with which such variations from ideal composition can be introduced into compounds having perovskite-like structures has frequently been noted.[14]

Attempts to prepare sizable single crystals of these compounds were not successful; so only powder-diffraction techniques could be used. A 57.3-mm-radius Debye-Scherrer camera of standard design was employed for photographic measurements, and a Norelco high-angle x-ray goniometer was used in spectrometer work. Radiations appropriate for the substance studied were used throughout.

Results

The diffraction patterns of all the compounds and solid solutions enumerated above are closely related to the patterns which would be expected from simple perovskite structures.[15] Differences between the ideal and observed patterns are the split reflections and superlattice reflections shown in the latter, which imply distortions of the lattice from cubic symmetry and an ordering of the atomic displacements and/or defects responsible for these distortions.

As shown by Megaw,[16] the number and intensity of the diffraction lines into which a given cubic perovskite reflection is split by distortion of the unit cube are quite different, depending on the nature of the distortion. Thus, except in cases where the splitting is so very slight as to make the separate reflections all but indistinguishable, the assignment of probable lattice symmetry and the indexing of the pattern are routine. The measured unit-cell parameters and lattice symmetries of the compounds and solid solutions studied are presented in Table 3.2. Wherever possible, the results of chemical analyses for tetrapositive transition-metal ions are listed. Some of the compounds included in the present investigation have been examined previously, and in these cases results of the earlier investigations are also given.

It must be remembered that, since the materials studied were available only as powders, the diffraction patterns obtained therefrom may indicate a higher lattice symmetry than the true one. This is especially to be feared in cases where apparent cubic symmetry is found.

Ionic Radii

In the discussion of the results listed in Table 3.2, it is convenient to introduce ionic radii. For the nontransition-metal ions, the ionic radii given by Pauling[17] are used. When available, empirical crystal radii of the transition-metal ions have been assumed.[17] In the case of the Mn^{4+} ion, Goldschmidt's value[15] for the radius has been used, while for ions such as Cr^{4+}, Fe^{4+}, Co^{3+}, and Co^{4+}, for which radii have not been given, an attempt has been made to interpolate a set of values which will be consistent with the empirical radii of other ions of the transition group. The curves used in this interpolation are shown in Fig. 3.10. A list of the radii to be employed in the following section is given in Table 3.3.

Discussion

The ideal perovskite structure for compounds of the type ABO_3 may be described as cubic, with twelvefold coordinated A ions at the corners, sixfold coordinated B ions at the body centers, and sixfold coordinated O ions at the face centers of the unit cubes. In the series of structures reported here, the transition-metal ions correspond to the octahedrally coordinated B ions.

Since the departures from cubic symmetry exhibited by the compounds included in Table 3.2 are generally small, reasonable average values for interionic distances can be calculated from the equations

$$r_{O-B} = \frac{1}{4} V^{1/3} , \quad (1)$$

$$r_{O-A} = \frac{\sqrt{2}}{4} V^{1/3} , \quad (2)$$

[14] A. F. Wells, *Structural Inorganic Chemistry*, p 331, Clarendon Press, Oxford, 1945.

[15] V. M. Goldschmidt, *Skrifter Norske Videnskaps-Akad. Oslo. I. Mat. Naturv. Kl.*, Vol. 1, No. 2 and Vol. 2, No. 8 (1926).

[16] H. D. Megaw, *Proc. Phys. Soc. (London)* 58, 133 (1946).

[17] L. Pauling, *The Nature of the Chemical Bond*, 2d ed., p 346–350, Cornell University Press, Ithaca, N. Y., 1945.

TABLE 3.2. X-RAY CRYSTALLOGRAPHIC DATA FOR PEROVSKITE STRUCTURES STUDIED

Compound	B Concentration (%)	a (Å)	b (Å)	c (Å)	β or α	V (Å)	Symmetry	Previous Investigation
$LaMnO_3$	8.9	7.960[a]	7.698	7.960	91°52′	487.5	Monoclinic	Cubic, a = 3.88 Å[d]
		11.439[b]	7.698	11.072			Orthorhombic	
$LaMnO_3$	25.4	7.812[a]	7.794	7.812	90°13′	475.6	Monoclinic	
		11.069	7.794	11.027			Orthorhombic	
$LaMnO_3$	35.3	7.769			90°35′	468.8	Rhombohedral	
(0.93 La–0.07 Ca)MnO_3		7.909[a]	7.708	7.909	91°26′	482.0	Monoclinic	
		11.324	7.708	11.044			Orthorhombic	
(0.85 La–0.15 Ca)MnO_3	18.5	7.848[a]	7.734	7.848	90°45′	476.3	Monoclinic	
		11.171	7.734	11.026			Orthorhombic	
(0.75 La–0.25 Ca)MnO_3	30.5	7.772				469.1	Unmeasurable monoclinic-orthorhombic splitting	
(0.60 La–0.40 Ca)MnO_3	43.5	7.710		7.677		456.4	Tetragonal	
(0.50 La–0.50 Ca)MnO_3	49.4	7.697				456.0	Cubic	
(0.50 La–0.50 Ca)MnO_3	56.4	7.689[a]	7.675	7.689	90°7′	453.8	Monoclinic	
		10.884	7.675	10.864			Orthorhombic	
(0.40 La–0.60 Ca)MnO_3	71.2	7.628		7.584		441.3	Tetragonal	
(0.25 La–0.75 Ca)MnO_3	78.5	7.568				433.5	Cubic	
$CaMnO_3$	71.0	7.481[a]	7.449	7.481	91°7′	416.8	Monoclinic	Distorted cubic, a = 3.73 Å for 80% Mn^{4+} [e]
		10.683	7.449	10.476			Orthorhombic	
$CaMnO_3$	90.8	7.465				416.0	Cubic	
$CaMnO_3$	96.9	7.465				416.0	Cubic	
$LaFeO_3$	5.0	7.852				484.1	Cubic	Cubic, a = 3.89 Å[d]
$SrFeO_3$		3.869				463.3[c]	Cubic	
$LaCoO_3$		7.651			90°40′	447.8	Rhombohedral	Rhombohedral, a = 3.82 Å, α = 90°42′[f]
(0.80 La–0.20 Sr)CoO_3	34.1	7.658			90°30′	449.1	Rhombohedral	
(0.65 La–0.35 Sr)CoO_3		7.664			90°23′	450.1	Rhombohedral	
(0.50 La–0.50 Sr)CoO_3		7.668				450.9	Cubic	
$SrCoO_3$		7.725				461.0	Cubic	
$LaCrO_3$	3.8	7.777[a]	7.750	7.777	90°15′	467.1	Monoclinic	Cubic, a = 3.88 Å[d]
		11.022	7.750	10.975			Orthorhombic	Cubic, a = 3.90 Å[g]
(0.50 La–0.50 Sr)CrO_3		7.754				466.2	Cubic	
$SrCrO_3$							Structure unrelated to perovskite	
$LaVO_3$		7.842				482.3	Cubic	Cubic, a = 3.91 Å[g]

[a]But for a few very weak reflections, the unit cell defined by these monoclinic parameters would be B-face centered. Therefore, if these reflections are neglected, the corresponding orthorhombic unit cell would be defined by a and c axes of half the length given in this table.

[b]Since the B-face of the monoclinic unit cell is a rhombus, an orthorhombic cell defined by the B-face diagonals and the b axis of the monoclinic cell can also be chosen. For purposes of discussion, it is frequently convenient to use the monoclinic rather than the orthorhombic cell, since its axes correspond with those of the undistorted perovskite cube. The true lattice symmetry would, of course, have to be determined from single-crystal data.

[c]The volume of a cell with doubled edges is given here for purposes of comparison only.

[d]St. v. Naray-Szabo, *Naturwiss.* **31**, 466 (1943).

[e]G. H. Jonker and J. H. Van Santen, *Physica* **16**, 337 (1950).

[f]F. Askham, I. Fankuchen, and R. Ward, *J. Am. Chem. Soc.* **72**, 3799 (1950).

[g]A. Wold and R. Ward, *J. Am. Chem. Soc.* **76**, 1029 (1954).

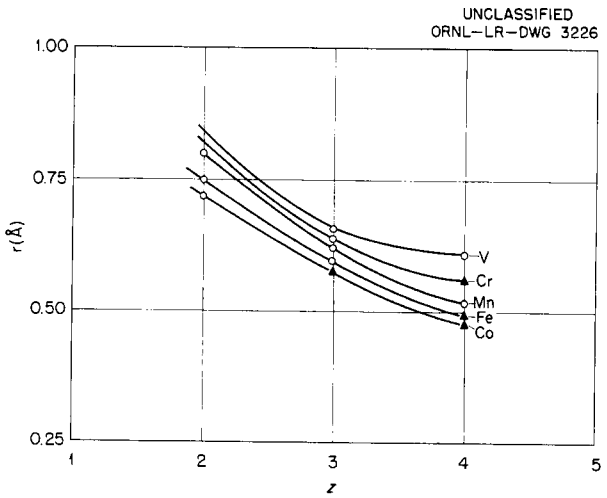

Fig. 3.10. Ionic Radii of Transition-Metal Ions of the Third Row as a Function of Their Nuclear Charge, z. O, Empirical radii; ▲, interpolated radii.

where V is the volume of the unit cell. Table 3.4 presents these distances, together with the radii sums calculated from Table 3.3, and the differences between theoretical and observed distances. Tolerance factors, t, defined by the equation

$$(R_O + R_A) = \sqrt{2}t(R_O + R_B) \ , \tag{3}$$

where R_O, R_A, and R_B are theoretical ionic radii, are also given.[15]

The δ values of Table 3.4 indicate close contacts between oxygen ions (O–O equals O–A in the ideal perovskite structure) and between oxygen and transition-metal ions. The negative values of δ probably reflect partial covalent-bond character, although any quantitative conclusions are precluded by the uncertainties in the ionic radii. The small positive values of δ_1 obtained for $SrFeO_3$ and $SrCoO_3$ may also be due to inaccurate radii or to nonstoichiometric composition of these substances caused by incomplete oxidation of iron or cobalt to the tetravalent state. For the latter possibility to be correct, however, the lattice defects accompanying nonstoichiometry would have to be interstitial cations, in contrast to the anion holes found in the similar case of $BaFeO_3$ by Erchak, Fankuchen, and Ward.[18]

[18]M. Erchak, I. Fankuchen, and R. Ward, *J. Am. Chem. Soc.* 68, 2085 (1946).

[19]H. D. Megaw, *Trans. Faraday Soc.* 42A, 224 (1946).

TABLE 3.3. IONIC RADII OF THE ELEMENTS CONTAINED IN THE PEROVSKITE STRUCTURES STUDIED

Ion	Radius (Å)
O^{2-}	1.40
Ca^{2+}	1.16*
Sr^{2+}	1.22*
La^{3+}	1.22*
V^{3+}	0.66
V^{4+}	0.61
Cr^{3+}	0.64
Cr^{4+}	0.56
Mn^{3+}	0.62
Mn^{4+}	0.52
Fe^{3+}	0.60
Fe^{4+}	0.50
Co^{3+}	0.58
Co^{4+}	0.48

*Corrected for change from sixfold to twelvefold coordination.

Megaw[19] has suggested that the different possible distortions of perovskite structures from cubic symmetry occur for separate ranges of values of the tolerance factor. Thus for $0.8 < t < 0.9$, orthorhombic (monoclinic) structures are predicted, whereas $0.9 < t < 0.97$ should lead to cubic symmetry and $0.97 < t < 1.02$ to tetragonal symmetry. It is seen that the tolerance factors for the compounds listed in Table 3.4 all lie between 0.91 and 0.98, where cubic or slightly distorted tetragonal structures are expected, but, as shown in Table 3.2, orthorhombic (monoclinic) and rhombohedral structures are also found experimentally. It would seem, therefore, that factors other than relative radii, possibly such as the tendency for the formation of covalent bonds between the transition-metal atom and some of the surrounding oxygen atoms,[20] may play an important role in determining the atomic displacements and, through them, the lattice symmetry.

This possibility of covalent bonding, indicated by close interatomic contacts and by the lattice

[20]H. D. Megaw, *Proc. Roy. Soc. (London)* 189A, 261 (1947).

TABLE 3.4. INTERATOMIC DISTANCES AND THEORETICAL IONIC-RADII SUMS

Compound	O–B Observed (Å)	$R_O + R_B$ (Å)	δ_1* (Å)	O–A (Å)	$R_O + R_A$ (Å)	δ_2** (Å)	t
$LaVO_3$	1.96	2.06	−0.10	2.77	2.62	+0.15	0.90
$SrVO_3$		2.01			2.62		0.92
$LaCrO_3$	1.94	2.04	−0.10	2.74	2.62	+0.12	0.91
$SrCrO_3$		1.96			2.62		0.95
$LaMnO_3$	1.98	2.02	−0.04	2.79	2.62	+0.17	0.92
$CaMnO_3$	1.87	1.92	−0.05	2.64	2.56	+0.08	0.94
$LaFeO_3$	1.96	2.00	−0.04	2.78	2.62	+0.16	0.93
$SrFeO_3$	1.94	1.90	+0.04	2.74	2.62	+0.12	0.98
$LaCoO_3$	1.91	1.98	−0.07	2.71	2.62	+0.09	0.94
$SrCoO_3$	1.93	1.88	+0.05	2.73	2.62	+0.11	0.98

*δ_1 = (O–B) observed minus ($R_O + R_B$). **δ_2 = (O–A) observed minus ($R_O + R_A$).

distortions, gives some explanation of the ferromagnetic and antiferromagnetic phases observed in the compounds at low temperatures. Indeed, magnetic coupling between the transition-metal atoms would be difficult to explain if the bonds between these atoms and the intervening oxygen atoms did not have considerable covalent character.

The doubled perovskite unit-cell edges so frequently recorded in Table 3.2 suggest puckered structures, with antiparallel atomic displacements, as found by Vousden[21] in $NaNbO_3$. These structures are therefore not likely to be ferroelectric, unless a metastable ferroelectric structure can be induced by an applied field.[22]

Of the two solid-solution systems studied, the ($LaCoO_3$–$SrCoO_3$) system appears to be anomalous. The increase in unit-cell volume with Co^{4+} concentration is opposite to the effect expected on the basis of relative ionic radii alone. The observations can be explained only if lanthanum cobaltate(III) is essentially a covalent compound and strontium cobaltate(IV) an ionic compound. No logical cause for this change in bond character can be advanced, however.

[21] P. Vousden, *Acta Cryst.* **4**, 373 (1951).

[22] H. D. Megaw, *Acta Cryst.* **5**, 739 (1952).

While the different lattice symmetries shown by the ($LaMnO_3$–$CaMnO_3$) solid solutions make a plot of lattice parameter vs Mn^{4+} concentration rather confusing, a plot of the unit-cell volume as a function of the same variable is, within experimental errors, a straight line of negative slope (see Fig. 3.11). This is in qualitative agreement with the expected decrease in transition-metal ion size between the tri- and tetravalent state.

As shown in Fig. 3.11 the unit-cell volumes of calcium manganate(IV) samples containing differing amounts of Mn^{4+} (71 to 98%, depending on the method of preparation) do not vary significantly. Substitution of trivalent ions for some tetravalent manganese ions should lead to an expansion of the ideal $CaMnO_3$ lattice, but charge equality demands that this substitution be accompanied by the introduction of either interstitial cations or anion vacancies. In order to explain the observed results, the vacancy model must be adopted, since this would lead to a lattice shrinkage which would compensate for the aforementioned expansion.

On the other hand, substitution of Mn^{4+} ions for some Mn^{3+} ions in the ideal $LaMnO_3$ structure should lead to lattice shrinkage due to the smaller size of the tetravalent ion and to either interstitial

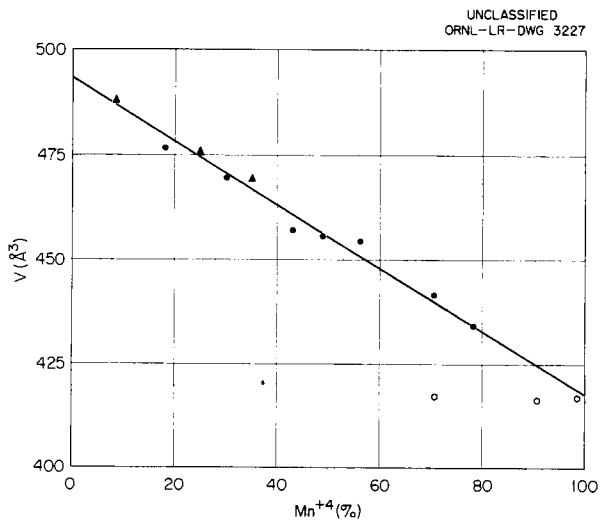

Fig. 3.11. Unit-Cell Volume as a Function of Mn^{4+} Concentration for the Solid-Solution System ($LaMnO_3$–$CaMnO_3$). Circled points represent calcium manganate(IV) samples, and crosses represent lanthanum manganate(III) samples prepared under different experimental conditions.

anions or cation vacancies. Again a vacancy model must be adopted to explain the observations. In this case, however, the lattice vacancies do not seem to contribute significantly to the shrinkage, as is shown by the fact that the cell volumes for $LaMnO_3$ defect structures follow the same straight line as the solid solutions of $CaMnO_3$ in $LaMnO_3$, where, of course, no defects should occur.

The above deductions are somewhat idealized in that the observed distortions from the ideal perovskite structure are ignored. Presumably the atomic displacements responsible for the distortions are not large enough to affect the situation significantly.

It is difficult to assess the importance of the differences between the results of the present investigation and those previous results included in Table 3.2. In most cases, these differences consist of weak reflections, indicative of multiple cells, which might be overlooked on weaker diffraction photographs. In one or two cases, however, split reflections due to previously unreported lattice distortions have been found. A possible explanation of this effect may lie in the wide variability of structure characteristic of these substances when prepared under different conditions.

The author wishes to thank E. O. Wollan and W. C. Koehler for their encouragement and many helpful discussions in connection with this work. Thanks are also due D. E. LaValle, who prepared many of the samples studied, A. D. Horton, who performed the chemical analyses of the samples, and R. M. Steele, whose assistance in recording the x-ray data was most helpful.

4. LOW-TEMPERATURE PHYSICS – NUCLEAR ALIGNMENT

BRUTE-FORCE POLARIZATION OF In^{115} NUCLEI

J. W. T. Dabbs, Jr. C. P. Stanford
L. D. Roberts S. Bernstein

Experiments are in progress on the polarization of In^{115} nuclei by application (at a very low temperature) of a magnetic field directly to the nucleus. Indium metal is thermally connected to a cooling salt by soldering to silver wires which are embedded in the cooling salt sample of $Fe(NH_4)(SO_4)_2 \cdot 12H_2O$ some 12 cm below. This salt is cooled by adiabatic demagnetization from 1.2°K and 15,000 gauss to a final temperature near 0.05°K. The sample unit is then lowered[1] to place the cooling salt inside a magnetic shield, where the field remains near zero, and to bring the indium sample into the gap of the Weiss magnet. The magnet is then turned on very slowly (to minimize eddy-current heating) to 10,000 gauss. Thus, a value of H/T of approximately 2×10^5 gauss/degree is applied to the indium sample, which serves to polarize the In^{115} nuclei to about 1.6%.

The nuclear sample is then bombarded with polarized thermal neutrons, and the intensity of the transmitted beam is measured with the neutron polarization parallel to and antiparallel to the nuclear polarization direction. A change in cross section is observed. The direction of the change gives the J value[2] ($J = I \pm \frac{1}{2}$) for the compound nucleus (In^{116}) formed by capture of the neutron, presumably for the 1.44-ev neutron resonance in In^{115}, other resonances contributing less strongly to the thermal-neutron cross section.

Experiments using neutrons polarized by transmission through magnetized iron have been carried out. These yielded a small effect when one compares polarized neutrons with unpolarized neutrons in the two possible relative spin directions. With the use of parallel magnetic fields (spins antiparallel) it was found that the cross section decreased (transmitted intensity increased) by 0.5 ± 0.12% when the neutrons were polarized, as compared with the unpolarized case. The "reversed" effect (with spins parallel) was also measured and was found to be −0.4% ± 0.2%. This effect was expected to be only 85% as large in this case because of inefficiencies in "flipping" or reversing the polarization of the neutrons. This result corresponds to $J = I + \frac{1}{2}$, which disagrees with the result of Brockhouse.[3]

A calculation of the size effect expected in this case has been carried out in which an averaging of cross section, neutron polarization and transmission effects, and counter sensitivity were taken into account. This yielded a calculated effect of 0.61% for an assumed temperature of 0.051°K in the spin-antiparallel case.

The above results are considered to be preliminary; the work in progress at present consists in changing the neutron-polarization method to that of diffraction from a single crystal of magnetized Fe_3O_4 as in previous work[1] on Sm^{149}. The new arrangement, however, places the Fe_3O_4 polarizer in the beam *ahead* of the nuclear sample, thus reducing by a large factor the intensity of neutrons actually striking the sample. Recent measurements have shown that substantial heating accompanies the transmission of the direct beam through indium, largely because of the 13-sec In^{116} isomeric beta decay. The new arrangement should obviate this difficulty, and the larger neutron polarization furnished by the Fe_3O_4, together with the use of a "flipper" to reverse the neutron spins, is expected to give a considerably larger effect.

MAGNETIC TRANSITION IN URANIUM TRI-IODIDE AT LIQUID-HELIUM TEMPERATURES

L. D. Roberts R. B. Murray

Previously reported measurements[4] of the magnetic susceptibility of UI_3 at liquid-helium temperatures indicate a transition from the paramagnetic to the antiferromagnetic state, in that the susceptibility passes through a maximum at 3.2°K, Fig. 4.1. These measurements also show a sharp peak in both the reactive and resistive components of the susceptibility near 1.5°K, which is strongly depressed by weak applied magnetic fields, Figs. 4.1 and 4.2. This latter behavior, as dis-

[1] S. Bernstein, L. D. Roberts, C. P. Stanford, J. W. T. Dabbs, and T. E. Stephenson, *Phys. Rev.* 94, 1243 (1954).

[2] M. E. Rose, *Phys. Rev.* 75, 213 (1949).

[3] B. N. Brockhouse, *Can. J. Phys.* 31, 431 (1953).

[4] L. D. Roberts, D. E. LaValle, and R. A. Erickson, *J. Chem. Phys.* 22, 1145 (1954).

cussed below, is interpreted as arising from a weak ferromagnetism involving the co-operation of very few electrons (~1 in 10^4).

In order to extend the study of these effects, the specific heat of UI_3 has been measured from 1.2 to 4.2°K. The specific-heat measurements were carried out by the techniques of low-temperature calorimetry, as discussed in previous progress reports. The sample of UI_3 (0.1041 mole) was contained in a gold-plated copper calorimeter cup and was handled at all times in an atmosphere of dry helium gas to prevent any chemical decomposition. The results of two specific-heat measurements, shown in Fig. 4.3, reveal a sharp, λ-type anomaly at 2.61°K. We associate this peak with the antiferromagnetic transition near 3°K. Above 3°K the magnetic specific heat behaves in a rather unusual manner, decreasing very slowly with increasing temperature, whereas the specific heat of many dilute paramagnetic salts decreases very nearly as $1/T^2$ above the transition, in agreement with theory.[5] An examination of the entropy curve, Fig. 4.4, obtained by integrating the specific-heat data, reveals that the electron-spin system is only partially disordered at temperatures just above the transition at 2.61°K. Thus this large specific heat above 3°K must represent the decay of an extensive short-range order. Sus-

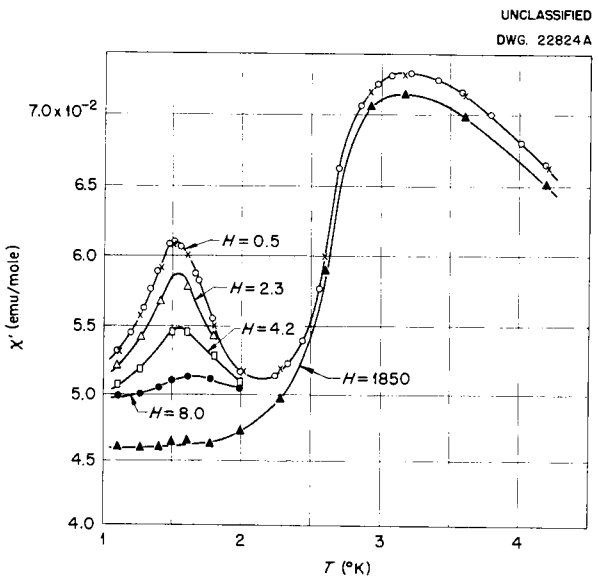

Fig. 4.1. Reactive Component of the Magnetic Susceptibility of UI_3 as a Function of Temperature and Magnetic Field. *H* is in gauss.

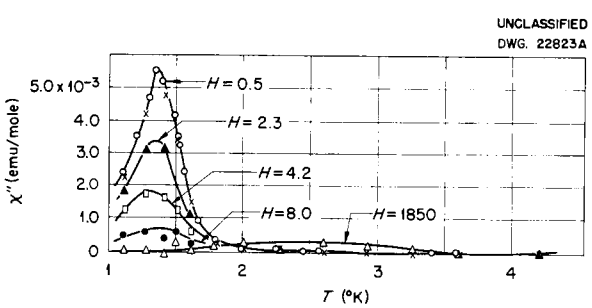

Fig. 4.2. Resistive Component of the Magnetic Susceptibility of UI_3 as a Function of Temperature and Magnetic Field. *H* is in gauss.

[5] J. H. Van Vleck, *J. Chem. Phys.* **5**, 320 (1937).

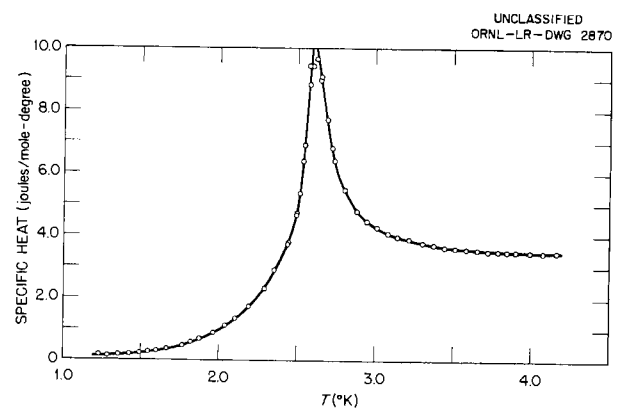

Fig. 4.3. Specific Heat of Uranium Tri-iodide.

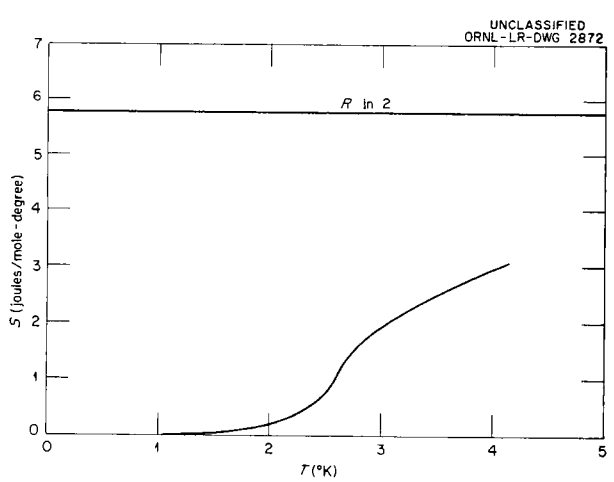

Fig. 4.4. Entropy of Uranium Tri-iodide.

ceptibility measurements[6] on dilute solid solutions of trivalent uranium suggest that the ground state is a Kramers doublet which would contribute a spin entropy of R ln 2 when both states are equally populated. Thus a large amount of spin entropy is yet to be gained, even above 4.2°K. In view of the large specific heat above 3°K, it is not surprising that the peak in the specific heat occurs at a somewhat lower temperature than does the susceptibility maximum, since the specific-heat anomaly presumably occurs with the onset of long-range magnetic ordering, whereas the susceptibility would be affected by the short-range order above the transition.

By way of comparison, the specific heat "tail" above the transition temperature of both[7,8] $MnCl_2 \cdot 4H_2O$ and $MnCl_2$ (which become antiferromagnetic near 2°K) falls off rather more slowly than $1/T^2$. This suggests that in all these cases short-range ordering effects play a larger role than has been predicted theoretically.[5] It is interesting to note that when the 1.5°K susceptibility peak is completely depressed by an applied field, the antiferromagnetic susceptibility extrapolated to 0°K is 0.63 times its maximum value at 3.2°K. This compares favorably with the Van Vleck theory of antiferromagnetism,[9] which predicts a ratio of 0.67, lending further support to the interpretation of the 3.2°K transition as antiferromagnetic.

It is interesting to note that the susceptibility maximum at 1.5°K, Fig. 4.1, is very nearly as large as that associated with the antiferromagnetic transition near 3°K, in spite of the fact that the specific heat shows no observable anomaly in the 1.5°K region. A specific-heat maximum at 1.5°K of the order of 10^{-3} times that at 2.61°K should have been detectable. It may be concluded from these facts that this large susceptibility arises from a type of ferromagnetic ordering of a very small fraction of the electrons. This interpretation is further supported by the extreme dependence of x' on H at 1.5°K, where it is seen that a field of only 5 oersteds depresses the susceptibility strongly, whereas the antiferromagnetic susceptibility near 3°K is relatively field insensitive.

[6] L. D. Roberts, C. C. Sartain, and B. Borie, *Revs. Mod. Phys.* 25, 170 (1953).

[7] S. A. Friedberg and J. D. Wasscher, *Physica* 19, 1072 (1953).

[8] R. B. Murray, *Phys. Rev.* 95, 307 (1954).

[9] J. H. Van Vleck, *J. Chem. Phys.* 9, 85 (1941).

As stated above, the 1850-oersted x' curve of Fig. 4.1 is interpreted as due to the antiferromagnetic transition near 3°K. We then ascribe differences between this curve and curves at lower fields as due to the "ferromagnetic" behavior, enabling one to determine x' ("ferromagnetic") as a function of field, Fig. 4.5. The corresponding magnetization as a function of field is obtained by integrating this "ferromagnetic" susceptibility and is shown in Fig. 4.6 for 1.5°K. This omits the small contribution of the resistive component

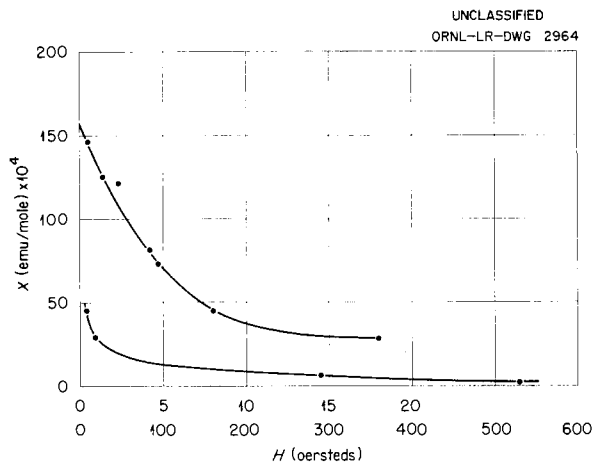

Fig. 4.5. "Ferromagnetic" Magnetic Susceptibility of UI_3 as a Function of Magnetic Field at 1.5°K.

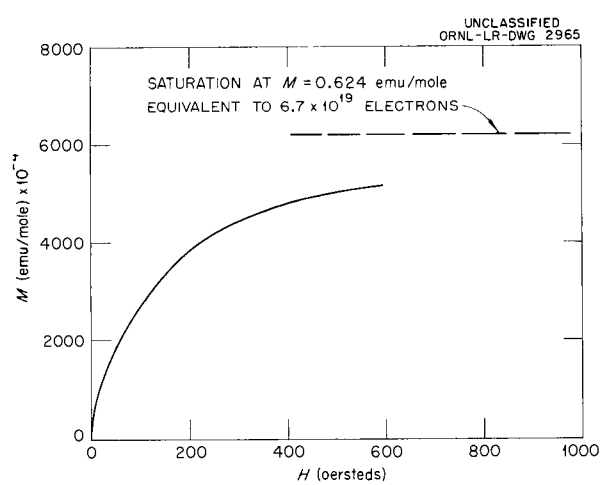

Fig. 4.6. "Ferromagnetic" Moment of UI_3 as a Function of Field at 1.5°K.

and also probably represents a technical, rather than complete, saturation. This magnetization curve cannot be fitted with a Brillouin function of spin ½, and, further, the extremely rapid rise of magnetization at low fields strongly suggests domain behavior. This concept is also supported by the presence of a very large out-of-phase component of the susceptibility x'', Fig. 4.2, as discussed below.

If we then assume this lower-temperature anomaly to be due to a type of domain ferromagnetism, we may calculate the number of electrons involved from two points of view. First, from the saturation curve of Fig. 4.6, we calculate this number to be 6.7×10^{19} electrons per mole, a mole fraction of 1.1×10^{-4}. Second, if we assume that these ferromagnetic domains rotate freely with an applied field, the observed zero-field susceptibility maximum at 1.5°K would require a mole fraction of "ferromagnetic" electrons of about 1×10^{-6}. This difference of a factor of 100 between the two calculations shows that the domain rotation is severely restricted, which is in accord with the appearance of the large out-of-phase component, x'', Fig. 4.2. The freedom of ferromagnetic-domain rotation may reasonably be associated with an activation energy, and correspondingly this restriction may be expected to become rapidly more severe with falling temperature. Thus the rise and fall of the susceptibility near 1.5°K may be due to a competition between a rising "ferromagnetic-domain" magnetization and an increasing restriction of rotation with decreasing temperature.

A weak magnetic remanence is found to accompany antiferromagnetic transitions in general. Neél[10] has suggested a possible explanation of this for crystals of a layer lattice, of which UI_3 is an example, by postulating the existence of antiferromagnetic domains. These antiferromagnetic domains are considered by Neel to consist of ferromagnetic sheets of alternating spin orientation with a corresponding zero net magnetization. The boundary between two antiferromagnetic domains is considered to be a region in which the spin phase shifts by 180 deg, giving rise to an uncompensated net spin, of a ferromagnetic nature, in the separating wall. On the basis of Neél's picture, the growth of magnetization in the separating walls would be expected to be simply correlated with the growth of long-range antiferromagnetic ordering throughout the crystal. In the case of UI_3 the observed parasitic ferromagnetism begins to grow in at temperatures just below the 2.61°K antiferromagnetic specific-heat anomaly. On the basis of our above observations it seems reasonable to attribute the magnetic behavior of UI_3 near 1.5°K to these domain-boundary effects as suggested by Neél. With this model, the lower susceptibility maximum is not an independent phenomenon but is an aspect of the antiferromagnetic transition at 3.2°K.

[10] L. Neél, Brussels Conference, Sept. 1954.

MAGNETIC TRANSITION IN ANHYDROUS MANGANOUS CHLORIDE AT LIQUID-HELIUM TEMPERATURES

R. B. Murray L. D. Roberts
R. A. Erickson[11]

Specific Heat

In a search for the thermal effects associated with a magnetic transition, measurements of the specific heat of $MnCl_2$ have been carried out from 1.2 to 4.2°K. Preliminary data on $MnCl_2$ sample I, in the form of a coarse powder, were reported in the preceding semiannual report.

In order to confirm the measurements on sample I, a second sample of $MnCl_2$ (sample II) was prepared by solidifying molten $MnCl_2$ in a cylindrical platinum cup which was then sealed with helium exchange gas in the copper calorimeter cup. A carbon resistance thermometer was embedded in the $MnCl_2$, and a heater coil was bonded to the platinum cup.

The results of a series of experiments on both samples I and II are given in Fig. 4.7. The most striking feature of the behavior of the specific heat is the appearance of two sharp, λ-type anomalies, located at 1.81 and 1.96°K, indicating a co-operative transition of a very unusual type. It was initially thought that such behavior might arise from the presence of two crystalline lattice phases; such a two-phase system could conceivably be brought about by mechanical deformations when sample I was broken into coarse chips before the calorimeter cup was loaded. The subsequent experiments on sample II, which was subject to no mechanical strains after solidification, agreed perfectly, however, with the eariler results on sample I. Furthermore, x-ray diffraction studies on ground $MnCl_2$ at room temperature, carried out

[11] Now at Ohio State University, Columbus, Ohio.

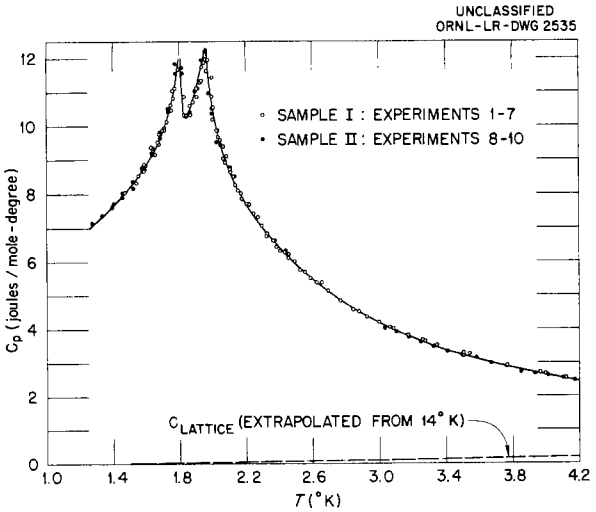

Fig. 4.7. Molar Specific Heat of $MnCl_2$.

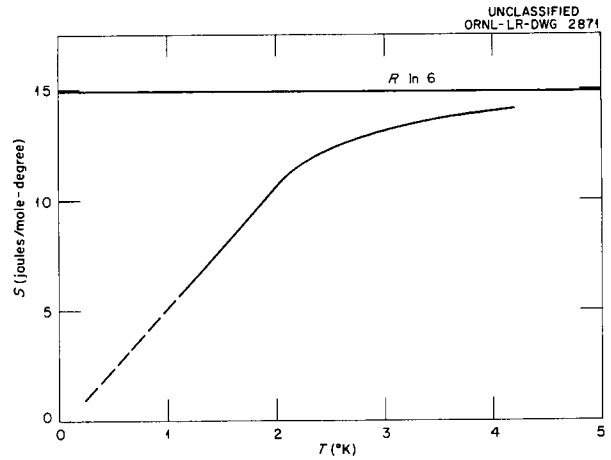

Fig. 4.8. Entropy of Manganese Chloride.

by R. D. Ellison, indicate that sample I was of a single crystalline phase. Chemical analysis of sample I showed it to be pure $MnCl_2$. In view of these facts, it is concluded that the two specific-heat maxima are an inherent property of $MnCl_2$. Further specific-heat measurements on sample I showed that the double peak was not due to thermal hysteresis effects.

In order to examine the behavior of the magnetic specific heat alone, it is desirable to subtract from the measured specific heat the small contribution arising from lattice vibrations. Earlier investigators[12] searching for cryomagnetic anomalies in $MnCl_2$ have measured the specific heat down to 14°K and found a lattice specific heat only. In the liquid-hydrogen range the lattice specific heat increases with increasing temperature as T^2, as predicted theoretically for a layer lattice such as $MnCl_2$, although these authors failed to note this point. The extrapolated lattice specific heat is shown in Fig. 4.7. The magnetic portion of the specific heat immediately above the transition decreases less rapidly than $1/T^2$ as predicted by theory, indicating the slow decay of short-range order.

Previous measurements of the magnetic susceptibility[13] of $MnCl_2$ down to liquid-hydrogen temperatures indicate that it is in a $^6S_{5/2}$ ground state, so that the electron-spin system when completely disordered can contribute a total of R ln 6 to the entropy. Extrapolating the magnetic specific heat to zero at 0 and 14°K, one can integrate the specific-heat data to obtain the entropy curve, Fig. 4.8. It is seen that about two-thirds of the available spin entropy has been achieved at 2°K, just above the transition, and that the disorder is sensibly complete at 5°K.

Magnetic Susceptibility

The magnetic susceptibility of $MnCl_2$ in the form of a spherical single crystal and as a powder has been measured at liquid-helium temperatures with the use of an a-c mutual inductance bridge.[14] The results are shown in Figs. 4.9 and 4.10. The positions of the two specific-heat maxima are shown by arrows. A positive Weiss constant of 3 to 4°K as found in these measurements and by other investigators[13] indicates an antiferromagnetic transition in the liquid-helium range. The measured susceptibility, however, does not demonstrate the characteristic maximum in the powder susceptibility which is usually found for such a transition. The single-crystal measurements at the lowest temperature, 1.2°K, show a susceptibility rising with decreasing temperature along both the a and c axes of the crystal, whereas the Van Vleck theory of antiferromagnetism[9] predicts, for temperatures below the antiferromagnetic

[12] O. Trapeznikowa and G. Miljutin, *Physik. Z. Sowjetunion* 11, No. 1, 55 (1937).

[13] C. Starr, F. Bitter, and A. R. Kauffman, *Phys. Rev.* 58, 977 (1940).

[14] R. A. Erickson, L. D. Roberts, and J. W. T. Dabbs, *Rev. Sci. Instr.* (in press).

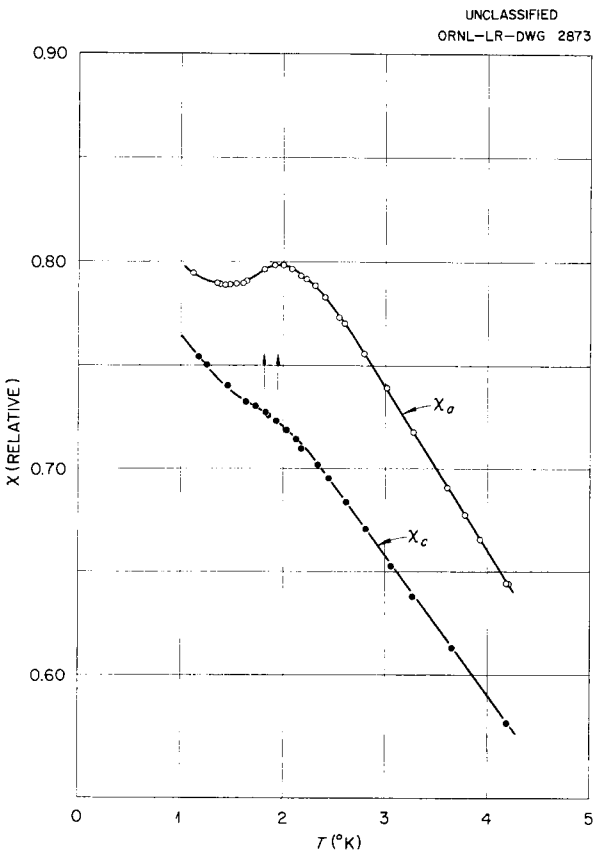

Fig. 4.9. Magnetic Susceptibility of Manganese Chloride – Single Crystal.

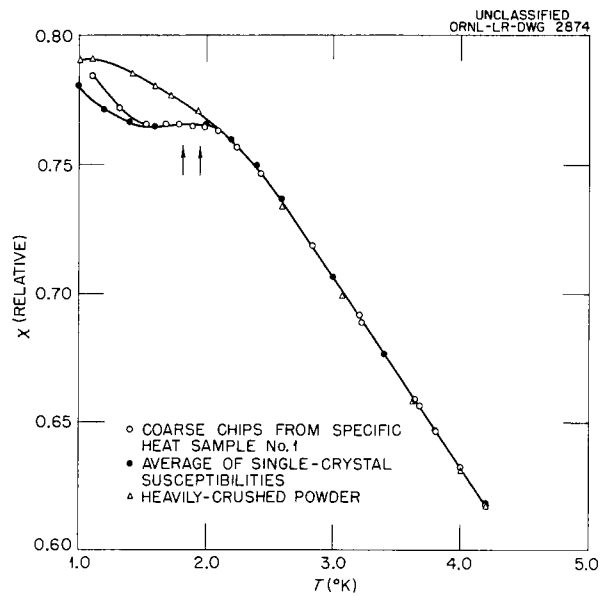

Fig. 4.10. Magnetic Susceptibility of Manganese Chloride – Powder.

transition, a falling susceptibility along the parallel axis (parallel to the direction of spontaneous antiferromagnetic alignment) and a temperature-independent susceptibility along the perpendicular direction.

The average of the single-crystal susceptibilities ($\frac{1}{3}\chi_c + \frac{2}{3}\chi_a$) is in good agreement with the measured powder susceptibility, Fig. 4.10, as expected. (For comparison these curves are normalized at 2.6 and 4.2°K.) In order to examine further the effect of mechanical working, a portion of $MnCl_2$ specific-heat sample I was heavily crushed to a fine powder, and its susceptibility is recorded in Fig. 4.10, again normalized for comparison with the other curves. The qualitative change in its behavior suggests the possible role of lattice defects brought about by mechanical working, but, in view of the agreement of the average of the single-crystal susceptibilities with the measured powder susceptibility of sample I, this effect presumably does not enter into the behavior of the other samples.

The susceptibilities were found to be independent of applied magnetic fields up to 500 oersteds throughout the liquid-helium region; thus the rising susceptibilities below 1.8°K cannot be due to a parasitic ferromagnetism as found in UI_3.

Discussion

From a consideration of the observed entropy curve, the anomalous behavior of the specific heat and susceptibility must be due to an ordering of the electron-spin system. In view of the sharpness of the specific-heat maxima, this transition is probably of a co-operative nature. The possibility of ferromagnetism below the transition can reasonably be ruled out by virtue of the small susceptibilities and their insensitivity to applied fields. The presence of two sharp λ-type specific-heat anomalies suggests a double transition in the spin system, the high-temperature transition being one from the paramagnetic state to a first type of antiferromagnetic ordering, the low-temperature transition resulting from a reorientation of the spin system to a second type of ordering. Such multiple transitions have been proposed

theoretically by several authors[15,16] on the basis of a molecular field theory and have been observed in manganese compounds of the type MnAs, which have a hexagonal crystal structure similar to that of $MnCl_2$. The magnitude of the specific-heat maxima calculated from the molecular field theory agrees approximately with that observed in $MnCl_2$.

In addition, there are two other effects which might contribute to the unusual aspects of this transition: first, the perturbing effect of crystalline electric fields[17] arising from the octahedron of Cl^- ions surrounding each Mn^{++} ion and, second, the influence of dipole-dipole coupling between the magnetic moments of Mn^{++} ions. To examine the first possibility, we have investigated the effect of including a term DS_z^2 in the magnetic Hamiltonian of an antiferromagnetic medium as given by Van Vleck,[9] where S_z is the z component of the spin angular momentum of a magnetic ion, and D is a constant determined by the magnitude of the crystalline electric field. The results of this calculation show that the antiferromagnetic transition temperature may be strongly depressed by the influence of a relatively small electric-field term. A significant contribution from electric-field effects to the behavior of $MnCl_2$ near 2°K, however, requires a much larger electric-field splitting than one would reasonably expect for Mn^{++}. On the other hand, because of the low transition temperature and the high magnetic density of spin $\frac{5}{2}$ ions, dipole forces must play an important role and may give rise to the observed anisotropy in the single-crystal susceptibilities. Studies of all these effects are being continued.

[15] Y. Yafet and C. Kittel, *Phys. Rev.* 87, 290 (1952).

[16] J. S. Smart, *Phys. Rev.* 90, 55 (1953).

[17] M. H. L. Pryce, *Phys. Rev.* 80, 1107 (1950).

5. HEAVY-ION PHYSICS

INVESTIGATION OF ELECTRON CAPTURE AND LOSS FOR HEAVY IONS PASSING THROUGH GASES

P. M. Stier R. A. Howard[1]
C. F. Barnett W. Bugg[2]

In the previous semiannual report,[3] the ratios of the electron-loss to the electron-capture cross section were given for each of the ions H^+, He^+, N^+, Ne^+, and A^+, passing through the stopping gases hydrogen, helium, nitrogen, oxygen, neon, and argon. These ratios were determined by observing the charge distribution in the particle beam after it passed through a gas target which was thick enough for equilibrium to be established between competing capture and loss processes. In continuation of these charge-exchange studies, the cross sections for electron loss by fast hydrogen atoms passing through the various gases have been measured in the energy range from 20 to 200 kev.

The apparatus used for these measurements consists of two charge-exchange chambers, shown schematically in Fig. 5.1. The first, designated as the neutralizer, converts part of the incident ion beam to atoms by charge exchange. The electrostatic deflection plates (electrostatic analyzer No. 1) remove all ions from the emergent beam so that the particle beam incident on the second gas cell is entirely neutral atoms. Ions formed by electron loss in this second gas cell are removed from the beam by an applied electric field. Since an ion formed by charge exchange must travel a finite distance in the electric field before it is deflected enough to be rejected by the collimating aperture, the effective length of the analyzers is somewhat less than the geometrical length. By segmenting the electric-field plates, it was possible to determine experimentally the effective length of each segment. The detector used is similar to the combination foil-thermocouple secondary-electron detector described previously.[4] Most of the data were taken with the use of the secondary-electron emission from a target as a measure of the beam intensity and were corrected for the relative secondary-electron emission for hydrogen ions and atoms. This correction was determined with the foil thermocouple used as a charge-insensitive detector.

To obtain the cross section, one measures the attenuation of the particle beam emerging from the gas cell. This attenuation is due to the removal of ions as they are formed and is related to the cross section by the formula

$$\frac{N}{N_0} = e^{-\pi\sigma_{01}} ,$$

where

N = flux of neutral hydrogen atoms emerging from the gas with the field on,

[1] Summer participant.

[2] Summer employee.

[3] P. M. Stier, C. F. Barnett, and G. E. Evans, *Phys. Semiann. Prog. Rep. March 10, 1954*, ORNL-1705, p 43.

[4] P. M. Stier, G. E. Evans, C. F. Barnett, and V. L. DiRito, *Phys. Semiann. Prog. Rep. Sept. 10, 1953*, ORNL-1620, p 37.

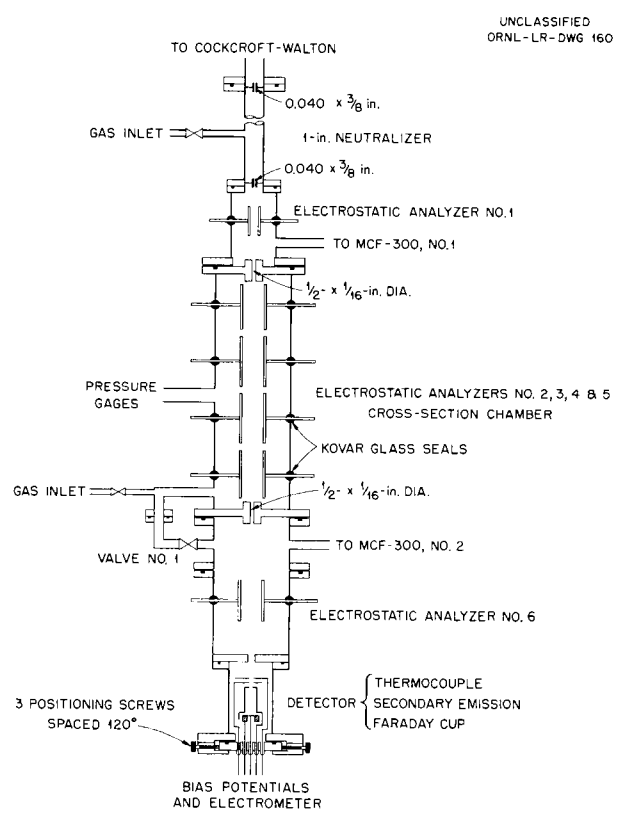

Fig. 5.1. Schematic Drawing of Electron-Loss Apparatus.

N_0 = flux of particles without field,

σ_{01} = cross section for electron loss by the fast hydrogen atom,

π = atoms presented by the target gas per square centimeter and determined from

$$\pi = \frac{Llmp}{RT},$$

in which

L = Avogadro's number,

l = thickness of the gas target,

m = number of atoms per molecule in the gas which is at pressure p and at absolute temperature T,

R = the gas constant.

The measured electron-loss cross sections are plotted as a function of velocity in Fig. 5.2. The cross sections for electron loss measured in hydrogen by Montague[5] and in air by Kanner[6] are included. The agreement between the present results and those of Montague and Kanner may be considered satisfactory in view of the experimental difficulties in this field.

The electron-capture cross sections may be computed from the previously reported ratios of loss-to-capture cross sections and the loss cross sections. The computed capture cross sections for protons in various gases are shown as a function of velocity in Fig. 5.3. Currently these capture cross sections are being directly measured, and preliminary results indicate that the measured and computed results agree within 10 or 15%.

[5] J. H. Montague, *Phys. Rev.* 81, 1026 (1951).
[6] H. Kanner, *Phys. Rev.* 84, 1211 (1951).

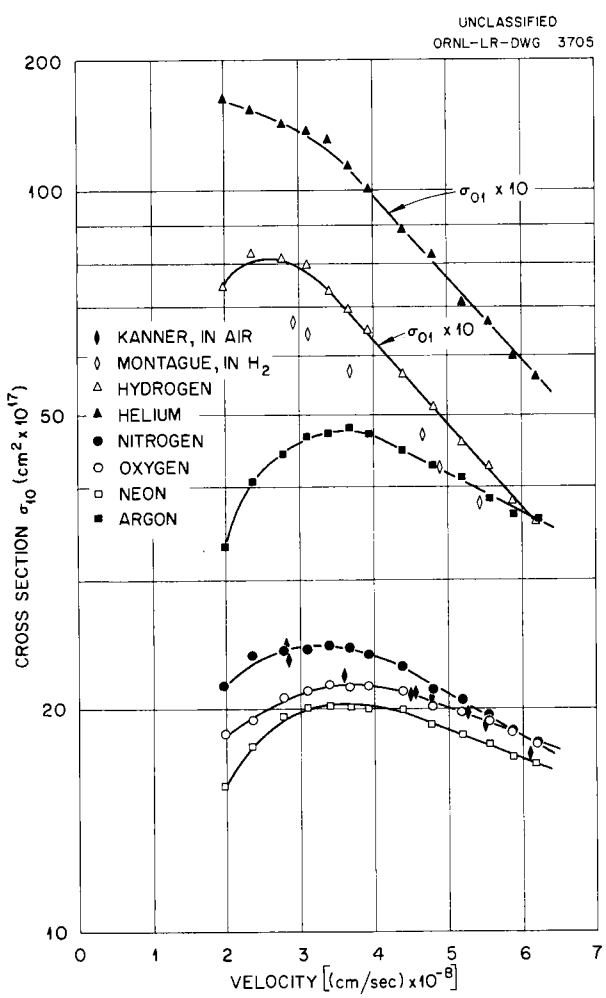

Fig. 5.2. Electron-Loss Cross Section per Atom, σ_{01}, for Hydrogen Atoms in Various Gases.

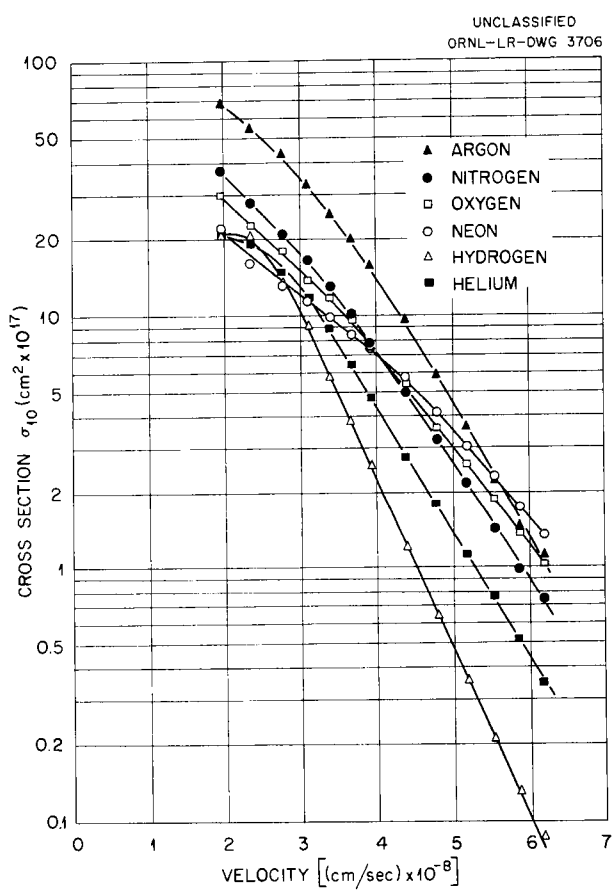

Fig. 5.3. Electron-Capture Cross Section per Atom, σ_{01}, for Protons in Various Gases; Calculated from σ_{01} and σ_{01}/σ_{10}.

6. NEUTRINO RECOIL

RECOIL SPECTROMETRY

Spectrometry of Recoils from Neutrino Emission in A^{37}

A. H. Snell F. Pleasonton

In our work on recoil spectrometry, radioactive gas is admitted to a conical, field-free volume (Fig. 6.1) at a total pressure of about 10^{-5} mm Hg, including impurities or carrier gas such as may be present. Some of the atoms recoiling as the result of radioactive decay emerge through the opening at the narrow end of the cone and form a beam which can be subjected to magnetic or electric deflection for momentum or energy analysis. The source volume is insulated from the deflection chamber so that a small predeflection acceleration can be applied if it is desired. After deflection, the ions are accelerated by 5000 v for counting on an electron multiplier. Both the magnet and the electric deflector focus in two directions; that is, they are stigmatic devices. The magnet deflects through 96.5 deg, and the electric deflector through 90 deg. Strong differential pumping is required to prevent the radioactive gas from diffusing into the multiplier chamber, where otherwise it would give an overwhelming background.

Argon-37 has been chosen as the first radionuclide to be studied in this device. Argon-37 is an electron-capturing isotope with a half life

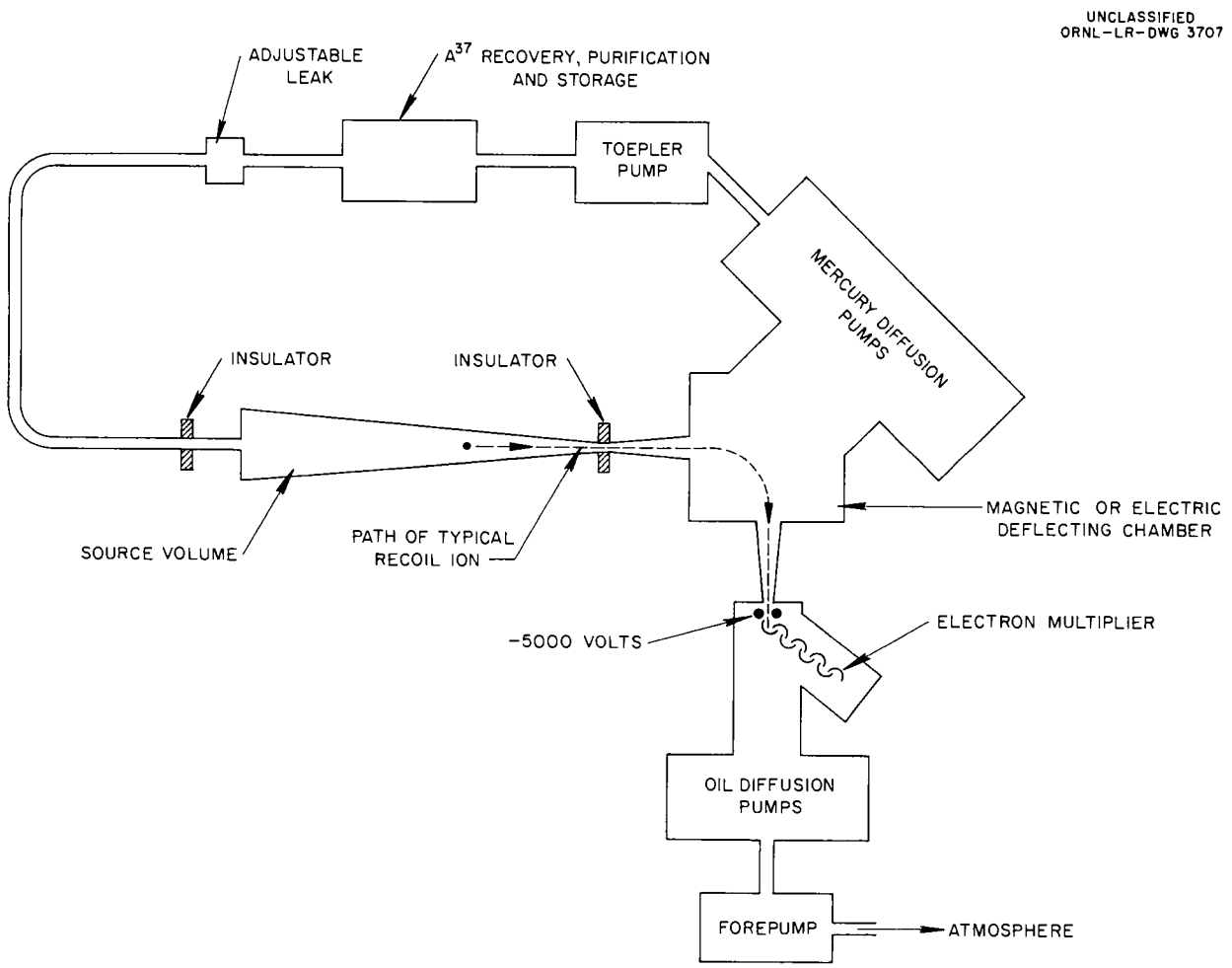

Fig. 6.1. Block Diagram of Recoil Spectrometer as Used in A^{37} Investigation.

of 35 days. It is prepared[1] in the LITR by the fast-neutron reaction $Ca^{40}(n,a)A^{37}$. The only mechanism that can give appreciable recoil momentum is neutrino emission. The disintegration energy available (814 kev), if carried off by a single, weightless neutrino, would impart a recoil energy of 9.6 ev to the resulting Cl^{37} atom. The x rays following electron capture are known to cause emission of Auger electrons, so that the chlorine can be expected to be ionized; in fact, the mean charge is known to be about +3.5.

Magnetic deflection was used in our first observations of these recoils. With the use of predeflection accelerations of 100 or 500 v, peaks were found corresponding to e/m values of 2/37, 3/37, and 4/37, respectively. Singly charged ions (1/37) were looked for but not found; quintuply charged ions (5/37) have not yet been sought. The triply charged ions were found to be about twice as abundant as the doubly and quadruply charged ions. On reducing the predeflection acceleration to about 20 v in order to obtain greater sensitivity to the energy of recoil, peaks like the one shown in Fig. 6.2 have been observed for the charge-3 ions. Note that the peak rises only about 50% above background. The position of the peak clearly demonstrates the momentum given by the neutrino emission, even though the exact location (over 11 ev on the recoil-energy scale) does not agree well with the predicted 9.6 ev. This discrepancy is not found in the electric deflection, and its origin is as yet not understood. The operating equation for the magnetic deflection is

$$(1) \qquad F = \frac{5900e}{[36.9762(E_r + eV_T)]^{1/2}} ,$$

where e is the ionic charge, 36.9762 is the atomic weight of Cl^{37+++}, E_r is the energy of recoil in electron volts, and V_T is the voltage applied to the source volume. F is the fluxmeter reading (ma), which is related to H through the expression H (gauss-cm) = $8.492 \times 10^5/F$. The constant 5900 has been determined by using an ion source to provide ions of known energy. Trouble is encountered in obtaining a sufficiently homogeneous beam from the source at low voltages (for example, 10 v), but this difficulty has been circumvented by using only higher voltages and varying the ion *mass* so that the magnet calibration can be checked down through the weak-field (150-gauss) region to be used in the recoil experiments. By this means it has been found that the figure 5900 holds constant through the operating region, and the magnet and fluxmeter are thought to be behaving properly. The calibration, however, depends directly on the energy measurement of the ions from the source rather than on the absolute properties of the magnetic field.

Electric deflection of the recoils was attempted in an effort to improve the signal relative to the background, because the electric-deflection apparatus permitted more effective differential pumping and also provided a larger solid angle for acceptance. There is an inherent disadvantage, however, in that the peaks arising from charge-3, -4, and -5 ions will be difficult to resolve because their natural width is too great. Figure 6.3 shows the result of a survey of the recoil spectrum of

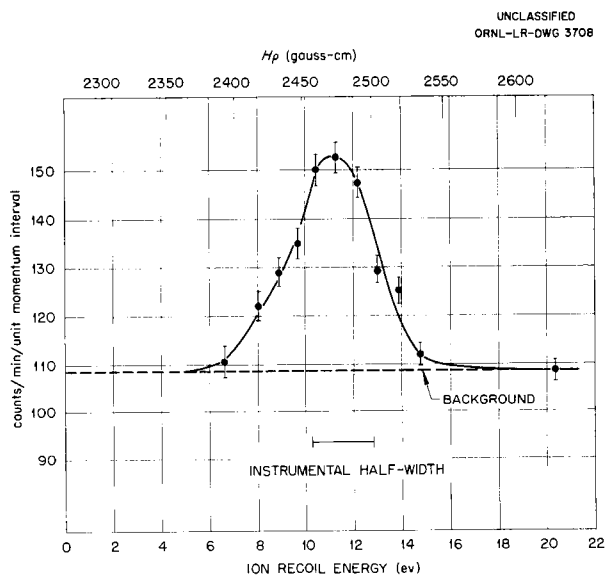

Fig. 6.2. Magnetic Analysis of the Charge-3 A^{37} Recoil Peak, with the Use of 20.21-v Predeflection Acceleration. Background has not been subtracted; calibration constant is 5900. The statistical limits shown pertain to the 50% probability interval. The "instrumental half-width" refers to the full width at half maximum of the transmission peak of the spectrometer for a monoenergetic line.

[1] We are indebted to R. E. McHenry of the Operations Division for the chemical separation and purification of argon.

A^{37} in which the voltage on the deflecting plates (7.450 v) was fixed and the predeflection acceleration was varied through a small range in the neighborhood of 20 v. The peak at the left of the figure is due to doubly charged Cl^{37} recoils, the recoil-energy scale being indicated above. The larger peak is a composite of the intense charge-3 peak (for which the recoil-energy scale is given at the top of the figure) and unresolved peaks arising from charge-4 and charge-5 ions. Because of the composite nature of the data, the plot is given in counts per minute rather than in counts per minute per unit energy interval.

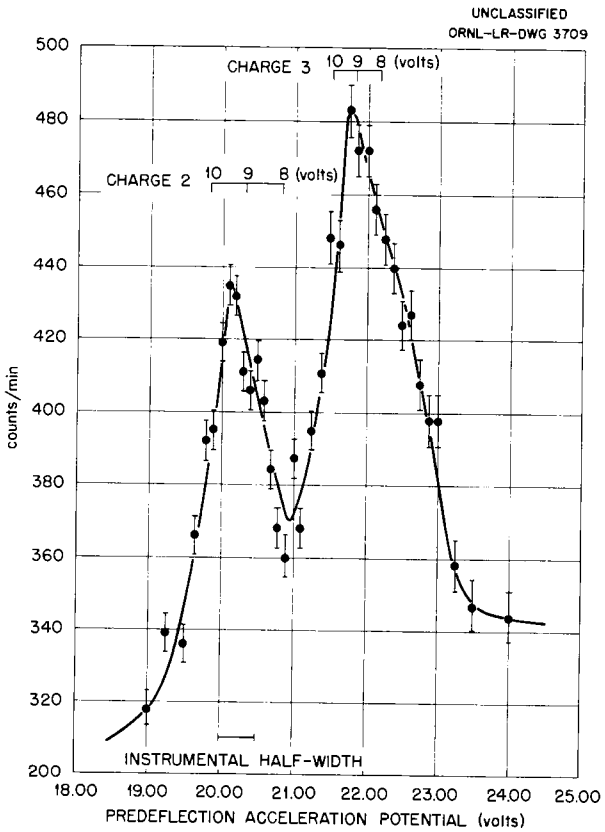

Fig. 6.3. Electric Analysis of the Ions Recoiling from Neutrino Emission in A^{37}. Background has not been subtracted. For these readings the deflecting plate voltage V_p was kept fixed at 7.450 v, and the voltage on the source volume was varied to give the abscissa scale. The statistical limits refer to the 50% probability interval. The "instrumental half-width" refers to the full width at half maximum of the transmission peak of the spectrometer for a monoenergetic line.

The operating equation for the electric deflector is

$$eV_p = 0.300(E_r + eV_T) ,$$

where V_p is the voltage on either deflecting plate (equal, but one positive and the other negative) relative to ground. The calibration constant 0.300 has again been determined, by using the ion source, at voltages high enough to make energy uncertainties unimportant. (This value of the constant agrees well with the design value associated with the radii of the deflecting surfaces.) This value of the constant is at present uncertain within 1%, and this uncertainty can explain the discrepancy between the position of the charge-2 peak in Fig. 6.3, at 9.2 ev on the recoil-energy scale as compared with the expected 9.6 ev. The singly charged peak would be most favorable to use for the recoil-energy measurement, but unfortunately it is so weak that a search failed to reveal its presence.

The recoil peaks have a very considerable energy spread, arising partly from the thermal motion of the A^{37} atoms but approximately doubled by the effect of recoil from Auger emission. J. M. Jauch[2] has calculated this line shape as a random-walk problem, and the widths of the observed peaks are in approximate agreement with the prediction, although a detailed comparison has not yet been made.

In conclusion, it may be stated that after this preliminary survey our objectives remain threefold: to obtain as accurate a measurement of the recoil energy as we can, to obtain the relative intensities of the various multiply charged peaks, and to obtain a detailed line profile for comparison with Jauch's calculation.

[2]Summer visitor from State University of Iowa.

7. THEORETICAL PHYSICS

NUCLEAR STRUCTURE FROM HIGH-ENERGY ELECTRON SCATTERING

G. T. Trammell

The measurements being conducted at Stanford[1] of the differential elastic-scattering cross sections of various nuclei for electrons of several energies in the 100- to 200-Mev range promise to give interesting new information concerning nuclear structure. In this energy range the de Broglie wave length is comparable to the radius of heavy nuclei, for example, the wave length of 100-Mev electrons is $\lambda = 12 \times 10^{-13}$ cm, whereas the approximate radius of the gold nucleus is $R_{Au} = 7 \times 10^{-13}$ cm. Thus the angular and energy dependence of the scattering cross section should be a sensitive indication of the spatial distribution of the nuclear charge.

The most extensive experimental investigations of heavy nuclei have been of Au^{197} and Pb^{208}; their cross sections are the same within experimental error.

With the analysis of the heavy-nuclei experiments as an objective, computations of the theoretical cross section have been made for several uniform-static-charge models of the gold nucleus and for electron energies in the neighborhoods of the experimentally realized energies 85, 126, and 154 Mev.

To compute the cross section, the Dirac equation was separated in spherical co-ordinates in the well-known manner, and the radial equations were integrated numerically out to a point external to the nucleus, where they are fitted to the previously computed coulomb functions and the phase shifts are obtained from the known asymptotic expressions for the coulomb functions. The details of this calculation will be given elsewhere; the resulting cross sections are given in Fig. 7.1, including the point-charge result[2] (labeled $kR = 0$). In Fig. 7.1, $k = E/\hbar c$, and R is the radius of the uniform charge model. For the high energies considered here, neglecting the electron mass in comparison with its energy can be shown to lead to negligible errors in the scattering cross section;[3] this then gives a Dirac equation with $1/k$ as the only length scale other than the lengths $l_1, l_2 \ldots l_n$, which specify the charge distribution, but this may be shown to necessitate a cross section of the form

$$\sigma(\theta) = \frac{1}{k^2}\, \phi(\theta, kl_1, kl_2, \ldots kl_n) \; .$$

If $R_{Au} \equiv r_0 \times (197)^{1/3} \times 10^{-13}$ cm, then the curves $kR = 2.8$, 4.2, and 5.58 correspond to energies 85, 126, and 154 Mev if $r_0 = 1.1$. The comparison of these theoretical curves with experiment is exemplified in Fig. 7.2, where the 126-Mev experimental data are plotted with several of the theoretical curves all renormalized so as to fit the experimental points at small angles. It is seen that a uniform model with $r_0 \approx 1.1$ will give a good fit to the experimental points so far as the positions of the peaks and valleys of the scattering curves are concerned, but some change away from the uniform model that will tend to smooth out the peaks and valleys at large angles is necessary. There is some evidence[2] that a "rounding of the edge" of the nuclear-charge distribution entails just such an effect and that a slightly rounded uniform model gives an appreciably better fit than is obtained in Fig. 7.2.

For charge distributions which do not differ very much from one of those represented in Fig. 7.1, it is unnecessary to integrate the radial differential equations; rather it is possible to treat the deviation as a small perturbation and calculate the difference in the phase shifts by first-order perturbation. This method makes possible a considerably quicker survey of various models and will be used in making a closer analysis of the experimental cross sections. To illustrate the validity of this procedure, the $kR = 3.84$ case has been calculated by the perturbation method from the $kR = 4.2$ case, and the result is shown as the dashed curve in Fig. 7.1.

The author would like to take this opportunity to acknowledge his debt to Thelma Arnette, who

[1] R. Hofstadter, H. R. Fechter, and J. A. McIntyre, *Phys. Rev.* 92, 978 (1953) and another paper to be published in *The Physical Review*. The author wishes to thank Professor Hofstadter for prepublication copies of their results.

[2] Similar results have been obtained: D. R. Yennie, R. N. Wilson, and D. S. Ravenhall, *Phys. Rev.* 92, 1325 (1953) and another paper to be published in *The Physical Review*. The author wishes to thank Professor Yennie for prepublication copies of their results.

[3] H. Feshback, *Phys. Rev.* 84, 1206 (1951).

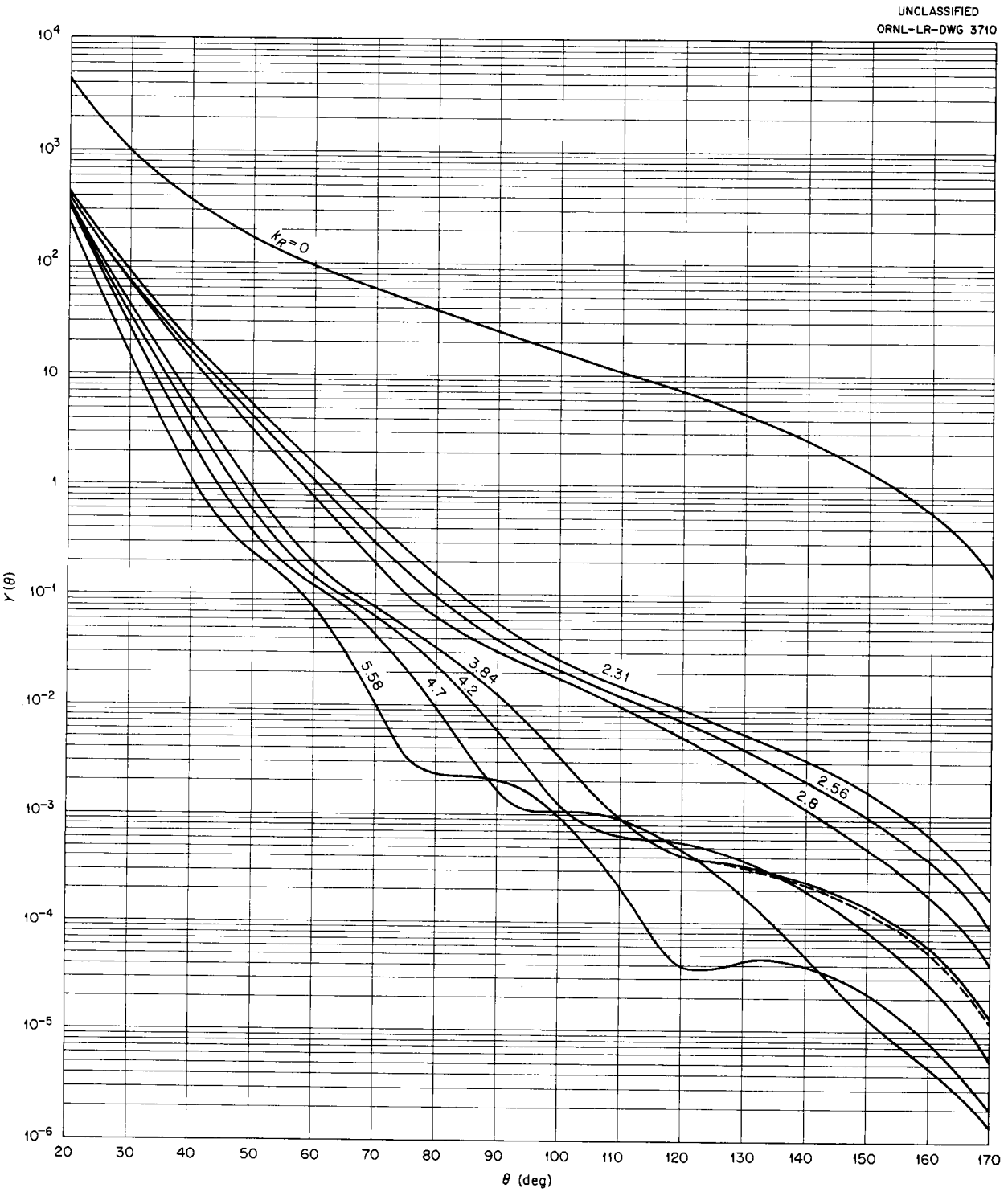

Fig. 7.1. Theoretical Scattering Cross Sections for Uniform-Charge-Distribution Models of the Gold Nucleus. The ordinate is $Y(\theta) = (2k)^2\ (d\sigma/d\Omega)$, where $k = E/\hbar c$. The abscissa is the scattering angle, and the numbers on the individual curves are assumed values of kR, where R is the radius of the model. The curve with $kR = 0$ is the pure coulomb cross section.

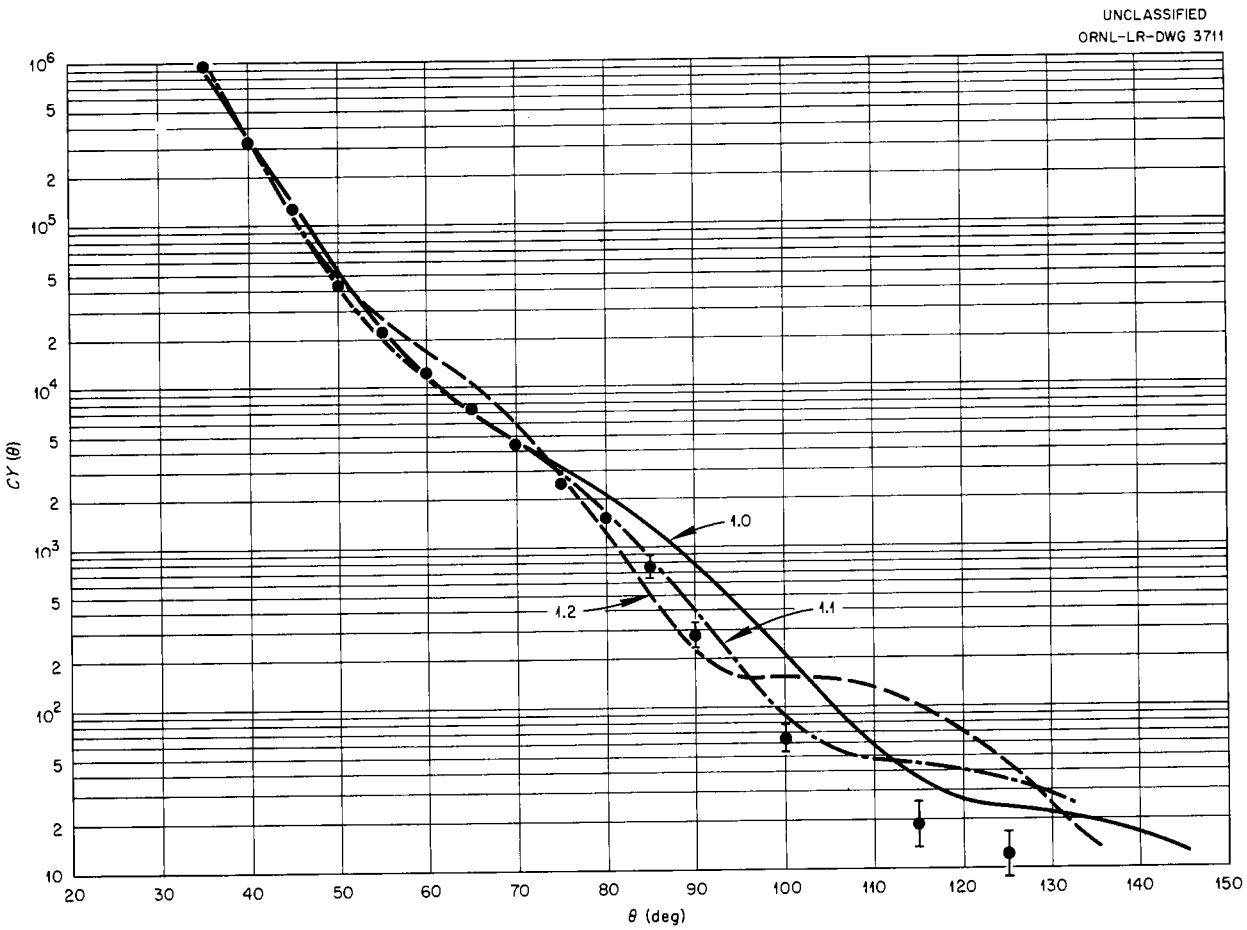

Fig. 7.2. Experimental Cross Section at 126 Mev Compared with Several Uniform-Charge-Distribution Models (Fig. 7.1) Renormalized to Give Good Fits to the Experimental Data at Small Angles. The experimental data taken by Hofstadter *et al.*[1] represent only relative cross sections. The numbers labeling the theoretical curves are $r_0 = R \times 10^{13}/(197)^{1/3}$ cm, where R is the radius of the nuclear model.

has done all the ORACLE coding that this problem entailed.

QUANTUM ELECTRODYNAMICS

T. A. Welton

Some further work with the formalism previously described has been undertaken with the aim of clarifying the origin and resolution of the difficulty presented by the infinite mass correction of conventional quantum electrodynamics. This correction causes no actual difficulty in computation when the technique of mass renormalization is used, but a more fundamental approach is clearly desirable.

The formalism previously described, which gives correctly the known results of quantum electrodynamics, rigorously pictures the radiation field as a classical vector potential acting *on* the electron. This potential is given by

$$A_\mu(x) = \frac{\sqrt{4\pi}}{L^2} \sum_k \frac{1}{(k^2)^{1/2}} e^{i\phi_{\mu k}} e^{ikx} ,$$

$$\phi_{\mu k} = -\phi_{\mu -k} , \tag{1}$$

where periodicity in a four-dimensional cube of side L has been assumed. The phase angles $\phi_{\mu k}$ are randomly distributed, and all physically meaningful results of calculation finally involve an average over all the $\phi_{\mu k}$.

The mass correction thus calculated agrees exactly with the familiar logarithmically divergent

quantity. However, it is easily shown that the necessary perturbation calculation becomes invalid just as the fractional mass correction becomes greater than unity. This leads to the suspicion that no *true* divergence exists and that a calculation without the use of perturbation theory would lead to a *finite* mass correction, roughly equal to the unperturbed mass. To give some additional support to this hypothesis, the mass correction was calculated on the assumption that the sum (in Eq. 1) contains only a single term, with k taken very large and an amplitude which is also very large, in order to take into account the fact that one plane wave is being used as a rough representation for a divergent spectrum of plane waves. On this assumption the mass correction can be calculated exactly by the use of the familiar theory of Hill's equation (second-order differential equation with periodic coefficients).

Some slight additional simplicity can be obtained by study of a scalar rather than a vector field, the same essential features being present. The wave equation becomes

$$m\psi = \gamma_\mu p_\mu \psi + \epsilon(e^{ikx} + e^{-ikx}) \ . \tag{2}$$

Because of the presence of a single plane wave only, the phase factor in Eq. 1 can be arbitrarily chosen. A natural system of co-ordinates will have one axis (the x-axis) in the direction of k. No other co-ordinate appears except as a derivative, so that it is convenient to introduce another co-ordinate axis (the y-axis) perpendicular to the x-axis and chosen in the direction of the constant part of the momentum vector. Since now only two components of p appear explicitly, a simple representation for the γ_μ can be chosen, so that

$$m\psi = i\sigma_1 \frac{\partial\psi}{\partial x} + Q\sigma_2\psi + \epsilon(e^{i|k|x} + e^{-i|k|x})\psi \ , \tag{3}$$

where σ_1 and σ_2 are Pauli spin matrices, Q is the component of momentum perpendicular to k, $|k|$ is the magnitude of the wave vector k, and ϵ is the coupling constant.

For $|k| >> m$, the fractional mass correction is

$$\frac{\delta m}{m} = -\frac{4\epsilon^2}{k^2}\frac{Q^2}{P^2 + Q^2} \ , \tag{4}$$

where P and Q are the unperturbed momentum components, and perturbation theory has been used. Similarly, the norm of the first-order correction to the wave function (which should be small compared with unity if Eq. 4 is to be valid) is given by

$$N = \frac{\epsilon^2}{k^2} \ . \tag{5}$$

Note that if $N << 1$, then $\delta m/m << 1$. If, on the other hand, ϵ^2/k^2 is chosen so large as to make $\delta m/m$ larger than unity, then the calculation becomes invalid.

An exact determination of m is possible from Eq. 3, which is equivalent to the simple second-order total differential equation

$$\left\{\frac{d^2}{d\theta^2} + \frac{4\epsilon^2}{k^2}\cos^2\theta + \frac{2i\epsilon}{k}\sin\theta + \frac{4m\epsilon}{k^2}\cos\theta + \frac{m^2 - Q^2}{k^2}\right\}\psi = 0 \ , \tag{6}$$

where $\theta = |k|x$.

The last term in the bracket is negligible for $k/m >> 1$, and the term with coefficient $m\epsilon/k^2$ can be treated by a perturbation argument. Dropping the last two terms, Eq. 6 has the solution

$$\psi = Ae^{i(2\epsilon/k)\sin\theta} \ , \tag{7}$$

where A is constant. If the term in $m\epsilon/k^2$ is included, a sufficiently accurate solution is obtained by taking A as a slowly varying function of θ:

$$A = e^{(2im/k)\theta} = e^{2imx} \ . \tag{8}$$

The approximate solution (Eq. 7) corresponds to no momentum, since the phase does not steadily increase in any direction. The factor (8), however, gives a momentum of $2m$ in the x-direction, so that the result can be written

$$m = \frac{1}{2}P \ , \tag{9}$$

with P the component of momentum in the direction of k.

It is important to note that the mass correction for large k and ϵ/k (when Eq. 9 is valid but Eq. 4 is not) is finite and independent of the coupling constant, so that in this case the divergence of the mass correction is only apparent.